DEVELOPMENT AND VALIDATION OF A NEW METHOD TO MODEL SLIP AND WORK INPUT FOR CENTRIFUGAL COMPRESSORS
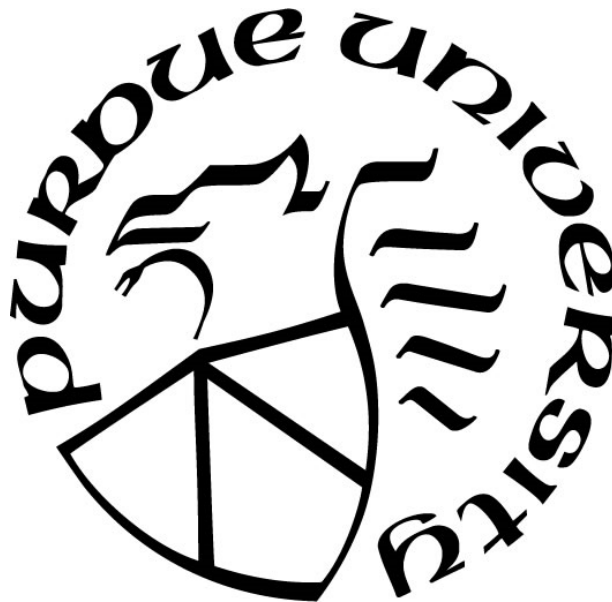
by

Herbert M. Harrison III

A Dissertation

Submitted to the Faculty of Purdue University

In Partial Fulfillment of the Requirements for the degree of

Doctor of Philosophy

School of Mechanical Engineering

West Lafayette, Indiana

May 2020

THE PURDUE UNIVERSITY GRADUATE SCHOOL
STATEMENT OF COMMITTEE APPROVAL

Dr. Nicole L. Key, Chair

School of Mechanical Engineering

Dr. Robert P. Lucht

School of Mechanical Engineering

Dr. Guillermo Paniagua

School of Mechanical Engineering

Dr. Rakesh Srivastava

Senior Manager, Advanced Technical Performance,
Operability and Methods Group, Honeywell Aerospace

Approved by:

Dr. Nicole L. Key

To the friends we make along the way.

ACKNOWLEDGMENTS

TABLE OF CONTENTS

LIST OF FIGURES

9

LIST OF TABLES

NOMENCLATURE

Acronyms

1D	one-dimensional
2D	two-dimensional
3D	three-dimensional
CFD	computational fluid dynamics
IGV	inlet guide vane
NACA	National Advisory Committee for Aeronautics
NASA	National Aeronautics and Space Administration
NPSS	Numerical Propulsion System Simulation
OTAC	Object Oriented Turbomachinery Analysis Code
PFG	perfect flow guidance
RMS	root mean square
SDS	stationary diffusion system
SRE	single relative eddy
SSCC	Single Stage Centrifugal Compressor
TPR	total pressure ratio
TTR	total temperature rise ratio

Symbols

A	area, new slip model coefficient
a	speed of sound
B	new slip model coefficient
b	blade span including clearance
b^*	ratio of diffuser inlet span to impeller exit span
C_f	coefficient of friction
c_p	specific heat at constant pressure
D	diameter

D_f	diffusion factor
D_h	hydraulic diameter
F	slip model constant
h	enthalpy
K	empirical loss coefficient
k_s	equivalent sand grain roughness
L_c	mean camberline blade length
L	meridional blade length
M_{U2}	machine Mach number
m	meridional length
$\dot{m}$	mass flow rate
N_s	specific speed
p	pressure
Re	Reynolds number
R	ideal gas constant
r	radius
r_e	radius of relative eddy
s	impeller backface gap width, impeller blade pitch, entropy
T	temperature
t	blade thickness
U	impeller velocity
V	velocity
V_{slip}	slip velocity
W	relative velocity
W_{max}	maximum relative velocity
w	work input
Z	blade number

Greek Symbols

α	absolute flow angle
β	relative flow angle
$\beta_{1,opt}$	optimum inlet relative flow angle
γ	ratio of specific heats
γ_b	meridional inclination angle
δ	deviation angle
ϵ	limiting radius ratio for Wiesner's slip model
ϵ_{TC}	tip clearance gap
ϵ_{wake}	wake fraction of blade pitch
ζ	flow path meridional inclination angle
λ	impeller inlet hub to tip radius ratio
ν	kinematic viscosity
ρ	density
ϕ	flow coefficient
σ	slip factor
χ	ratio of actual loading coefficient to perfect flow guidance loading coefficient
ψ	loading coefficient
ω	angular velocity
$\bar{\omega}$	total pressure loss coefficient

Subscripts

0	stagnation condition
1	impeller inlet
$1-$	just upstream of impeller leading edge
$1+$	just downstream of impeller leading edge
2	impeller exit
3	diffuser exit
b	blade parameter

BL	blade loading
BLK	blockage
CL	clearance
$design$	fixed design specification
DF	disc friction
eff	effective value
ERR	error
EXP	experimental measurement
EXT	external loss
FAM	family implementation
GEN	general implementation
h	hub
I	ideal condition
imp	impeller
inc	incidence
INT	internal loss
m	meridional direction, root mean square or mean span
MB	main blade
MIX	mixing
PFG	perfect flow guidance condition
PS	pressure surface
Q	parameter associated with Qiu's slip model
RC	recirculation
s	isentropic process
SB	splitter blade
sds	stationary diffusion system
sep	wake separation velocity
SF	skin friction
SS	suction surface
$STAGE$	stage parameter

t	tip
θ	tangential direction
VB	parameter associated with von Backström's slip model
W	parameter associated with Wiesner's slip model

ABSTRACT

Slip in centrifugal compressors arises from imperfect guidance of the flow by the impeller blades and reduces the work input delivered by the impeller, and slip models are typically used to predict slip in preliminary design. However, slip models are typically calibrated with data that are not representative of modern aerospace compressors (i.e. pumps, turbochargers, or industrial compressors) and do not account for the variation of slip factor with operating condition. A generalized meanline model for centrifugal compressors is developed to interrogate slip in centrifugal compressors from a one-dimensional design perspective. The meanline model is used to investigate the efficacy of slip models for predicting the slip factor and work input of modern, high-speed impellers at design and off-design conditions. Three slip models are used to predict the performance of five impellers, four of which are documented in the open literature. All three slip models generally overpredict the slip factor, and the largest error in the prediction of slip factor typically occurred near design speed. In addition, the analysis shows a close correlation between slip factor and two key design parameters of machine Mach number and loading coefficient over the entire compressor operating range. Finally, error propagation analysis shows that the error in impeller work input is proportional to the error in slip factor scaled by the square of machine Mach number and reveals the inherent challenge of accurate prediction of work input for high-speed machines.

Finally, a new method of modeling slip factor and work input for centrifugal compressor impellers is presented. Rather than using geometry to predict the behavior of the flow at the impeller exit, the new method leverages governing relationships to predict the work input delivered by the impeller with dimensionless design parameters. The approach incorporates both impeller geometry and flow conditions and, therefore, is inherently able to predict the slip factor at design and off-design conditions. Five impeller cases are used to demonstrate the efficacy of the method, four of which are well documented in the open literature. Multiple implementations of the model are introduced to enable users to customize the model to specific applications. Significant improvement in the accuracy of the prediction of slip factor and work input is obtained at both design and off-design conditions relative to Wiesner's slip model. While Wiesner's model predicts

the slip factor of 52% of the data within ±0.05 absolute error, the most accurate implementation of the new model predicts 99% of the data within the same error band. The effects of external losses and flow blockage on the model are considered, and the new model is fairly insensitive to the effects of both phenomena. Finally, detailed procedures to incorporate the new model into a meanline analysis tool are provided in the appendices.

1. INTRODUCTION

1.1 Motivation

Gas turbines have developed into a mature technology with a large body of research available for the foundations of modern applications. Designers draw on a wealth of historical data, available in the form of experimental correlations and analytical models, combined with advanced computational methods to achieve extremely efficient power generation. As the accessibility of high-performance computing has rapidly increased over recent decades, the use of complex three-dimensional (3D) simulations to augment the design process has become more common. Despite the continued improvement of computational capabilities and turbulence models for three-dimensional models, the one-dimensional (1D) design approach remains a critical component of turbomachinery design. Key features of the compressor and turbine are established in the preliminary design phase using one-dimensional relationships that govern the fundamental flow processes of the machine (Japikse, 1996; Jones, 2014), and poor design choices in preliminary design cannot be remedied by any amount of optimization during detailed design with 3D simulations. Furthermore, three-dimensional simulations are unnecessarily complex for relatively straightforward procedures like inlet sizing and have turnaround times that are too large for the iterative nature of the preliminary design phase. One-dimensional design tools, on the other hand, provide near instantaneous results for review. Thus, the one-dimensional approach has been the foundation of the centrifugal compressor design process for decades and will continue to be for the foreseeable future.

However, the inherently one-dimensional, inviscid equations utilized in the preliminary design phase do not account for non-ideal flow processes during the compression process. Models must be employed and incorporated into the one-dimensional equations to capture the nonideal flow processes that occur as a result of the unsteady, three-dimensional, rotational flow generated by impellers and diffusers in centrifugal compressors. The entropy generation due to various processes such as skin friction and incidence are estimated with loss models. Slip models are used to predict the deviation of the impeller exit flow from the impeller exit blade angle, known as slip in centrifugal compressors. Because slip and loss strongly influence the work input and efficiency

of the stage, accurate estimation of the parameters is vital to success in preliminary design. Unfortunately, reliable prediction of slip for the centrifugal compressor design space remains difficult despite almost an entire century of research. There are many models available in the open literature, but they often require significant tuning to obtain estimations of slip representative of actual operation. Since prediction of slip, and by extension work input, remains an inexact science, some organizations have developed correlations for specific impeller families instead of relying on general slip models (Medic et al., 2014).

High impeller tip speeds enabled by modern materials have only exacerbated the difficulty in accurate prediction of work input. To illustrate this problem, the experimentally measured work for Krain's transonic impeller (Eisenlohr et al., 2002) is shown in terms of total temperature rise ratio (TTR) as a function of corrected mass flow rate in Figure 1.1. Alongside the experimental observations, which are shown in black, the work input calculated with the meanline analysis tool presented in Chapter 2 with Wiesner's classic slip model (Wiesner, 1967), is shown in red. Where there is a difference between the measured and modeled values, a black-to-red gradated line connects the measured and modeled pairs. The experimental and one-dimensional calculations agree quite well at low speed, but as wheel speed increases, the predicted total temperature rise ratio diverges from the experimental measurements. At design speed, the meanline model overpredicts the total temperature rise ratio by more than the measured difference in work input between the 95% and 100% speedlines.

To determine the root cause of the large difference in total temperature rise ratio between the model and experiment, the Euler turbomachinery equation is examined:

$$-w = U_2 V_{\theta 2} - U_1 V_{\theta 1}. \tag{1.1}$$

In equation (1.1), w is the compressor work input, U is the velocity of the reference frame, V_θ is the absolute tangential velocity, and the subscripts 1 and 2 are the impeller inlet and impeller exit stations, respectively. The Euler turbomachinery equation links the change in angular momentum brought about by the rotating blade rows to the enthalpy change of the stage. For axial inlet flow (no pre-whirl), the impeller inlet angular velocity term is equal to zero, and the work input is only
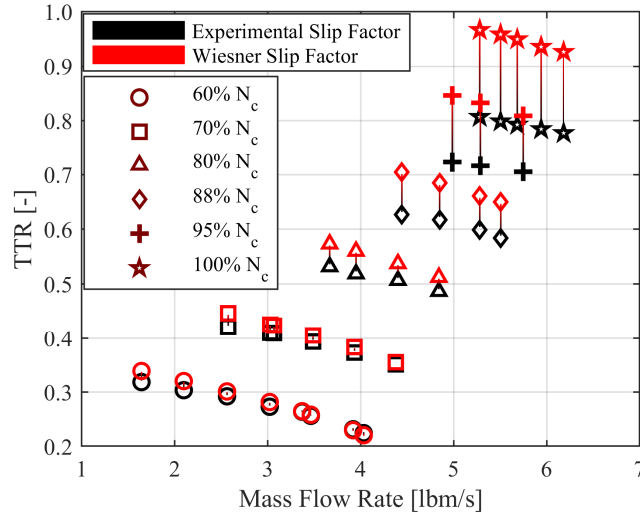
Figure 1.1: Map of the experimentally measured TTR and calculated TTR for Wiesner's slip model applied to Krain's transonic impeller, with each pair of points connected for reference.

dependent on the impeller exit tip speed and tangential flow velocity. Since the inlet flow in Krain's experiment was axial, and with the assumption of adiabatic operation, the impeller exit velocity triangle determines the temperature rise of the stage. The differences between the model and experiment must, therefore, be due to differences in the modeled and actual components of the impeller exit velocity triangle. Since the data pairs shown in Figure 1.1 are from the same impeller operating at the same conditions (U_2 is the same for each pair of points), the difference between the model and experiment is the result of inaccurate estimation of the impeller exit tangential velocity through Wiesner's slip model. Since the impeller exit tangential velocity is multiplied by the impeller exit tip speed, the error in the estimation of slip is scaled by the impeller tip speed through the Euler turbomachinery equation and causes large errors in the predicted total temperature rise ratio at high impeller tip speeds.

As shown with the Krain case study, accurate prediction of slip is vital to success in the preliminary design phase. This is especially true for high-speed compressors because work input, which is a core parameter of stage performance, is more sensitive to errors in the prediction of slip at high impeller tip speeds. Much of the discussion in the open literature has emphasized the prediction of slip at the design point of lower-speed compressors, pumps, or radially bladed impellers, which are not representative of the modern, high-speed centrifugal compressor design space

(Lakshminarayana, 1995). Since any error in the prediction of the slip velocity results in a corresponding error in work input scaled by the impeller tip speed, models validated for pumps and low-speed designs may be inadequate for the high-speed design space. Thus, the challenges and considerations when utilizing slip models to predict work input for high-speed compressors at both design and off-design conditions must be addressed to improve the reliability of compressor preliminary design.

1.2   Review of Impeller Flow

One-dimensional models and design tools are not intended to provide detailed insight into the complex flow field that develops through a centrifugal compressor. Rather, they are intended to give a baseline representation that serves as the foundation for development of a compressor design from concept to application. While the one-dimensional tools intentionally simplify extremely complex flow fields, an understanding of the basic characteristics of the centrifugal compressor flow field is necessary. Therefore, a review of the the centrifugal compressor flow field is prudent to establish the fundamental principles of centrifugal compressor work input and pressure rise, as well as the flow features that contribute to entropy generation and slip.

Centrifugal compressors were originally designed assuming no separations through the impeller and axisymmetric impeller discharge flow. However, Dean and Senoo's (1960) landmark paper describing the "jet-wake flow" proved that this was not the case through experimental investigations. The model accompanying the experimental work proposed that the jet-wake flow was composed of two discrete regions: the high relative velocity jet on the pressure side of the impeller blade and the low relative velocity wake on the suction side of the impeller blade. The authors acknowledged that a realistic flow would likely feature smooth velocity gradients between the jet and wake regions, but they proposed this simplified approach to improve prediction of losses from the existing design approach for which a uniform exit flow field was assumed.

Since Dean and Senoo's early work, the understanding of the impeller flow field has been drastically improved in conjunction with advancements in instrumentation and data acquisition technologies. The impeller velocity field has been characterized with numerous variations of

nonintrusive laser measurement systems. A detailed picture of the jet-wake structure was first illustrated by Eckardt (1975, 1976). The core flow was observed to tend towards the pressure side of the passage which, when interacting with the secondary flows induced by the turn to radial and tip leakage flow, creates a pooling of low-energy fluid in the shroud-suction surface corner. The wake region occupied 35% of the impeller passage at the trailing edge with steep gradients between the jet and wake regions. The flow remained non-axisymmetric through the largest radius ratio (1.05) measured in the vaneless diffuser.

Similar development of the jet-wake flow structure in a radially bladed impeller and vaneless diffuser was replicated by Krain (1981) with only small differences attributable to slight alterations in geometry. When a vaned diffuser was coupled with the same radial impeller, the diffuser potential field had minor effects on the impeller exit flow. The weak influence of the diffuser vanes on the impeller flow was likely due to the high vane-leading-edge-to-impeller-exit ratio ($r_3/r_2 = 1.1$) and low Mach number at the diffuser leading edge. Unsteadiness from the impeller discharge flow generated flow angle fluctuations greater than 15°, and a high level of unsteadiness persisted up to the farthest downstream measurement location, the diffuser throat.

Researchers investigating the impeller discharge flow have consistently observed the jet-wake structure, though its size, shape, and location within the passage appear to be dependent on shroud curvature and blade exit angle, among other factors (Cumpsty, 1989; Johnson & Moore, 1980). In some cases, the wake has manifested as a large low-velocity region that dominates the impeller discharge flow, while in others the wake moved away from the shroud-suction surface corner to occupy the mid-passage hub region (Inoue & Cumpsty, 1984; Krain, 1988). While the exact form of the wake at the impeller exit is not consistent across impeller geometries, large velocity gradients in both the pitchwise and spanwise directions almost universally arise as a result of the jet-wake structure, and the downstream diffuser must efficiently recover static pressure from the complex impeller exit flow (Gooding et al., 2019).

In addition to the jet-wake pattern, several additional flow phenomena develop within impeller passages, as illustrated in Figure 1.2, that compound the flow complexity inherent to centrifugal compressors (Cumpsty, 1989; Ibaraki et al., 2009; Kaneko & Tsujita, 2015; Wood et al., 1983).

Vortices develop at the impeller leading edge near both the hub and shroud, and shocks may occur near the blade tip in high-speed machines. The tip leakage flow conveys flow from the pressure side of the blade to the suction side of the blade through the tip gap between the blade and shroud, and the jet and wake may also develop distinct secondary flow patterns. Together these interacting flow features further complicate the impeller flow field and impede accurate prediction of centrifugal compressor performance.
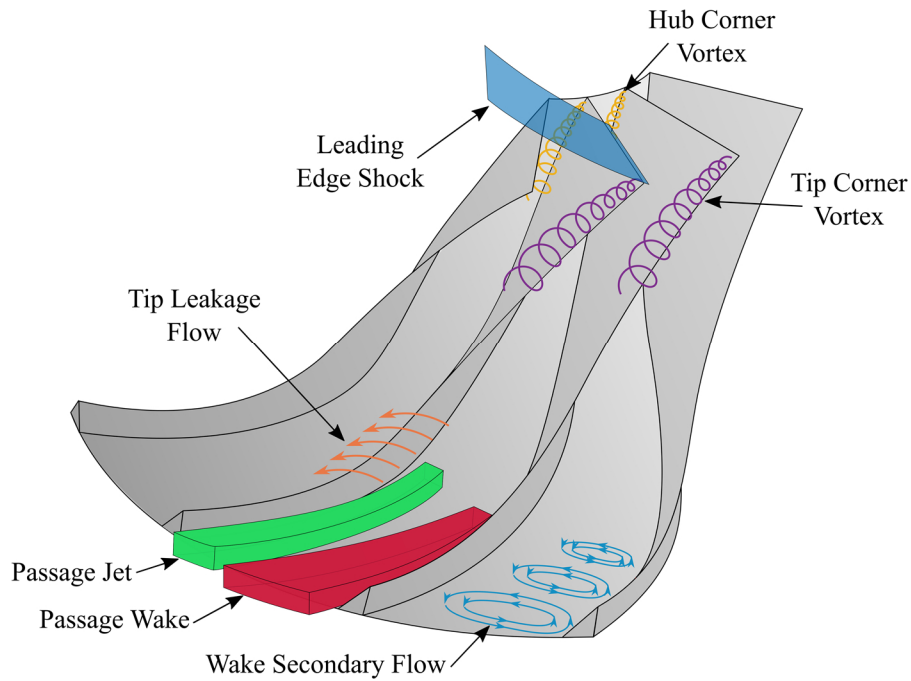
Figure 1.2: Various flow processes commonly developed within centrifugal compressor impellers.

1.3 Meanline Modeling

Detailed investigations of the complex flow fields in centrifugal compressors are conducted to dissect the component performance of a compressor or delve into the flow features for the development of one-dimensional models. In contrast to that, meanline modeling is used to distill the spatial and time variant flow field into the mixed-out average parameters at the inlet and exit of each blade row in the rotating machinery. The compressor flow field is represented through one-dimensional relationships, known as the meanline equations, that govern the flow processes of the machine and establish the fundamental characteristics of the stage (Japikse, 1996; Jones, 2014).

23
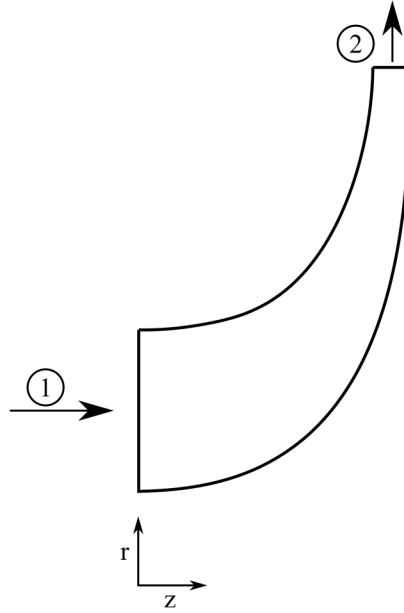
Figure 1.3: Meanline representation of flow through a centrifugal compressor impeller with the axial and radial directions indicated by r and z, respectively.

The meanline representation of flow through an arbitrary impeller is shown in Figure 1.3. Rather than developing detailed three-dimensional fields that show development of the flow within the impeller in the meridional direction, as well as the spanwise and pitchwise variation of the flow, the impeller flow is fully characterized by the average flow field at the inlet (station 1) and exit (station 2). The 1D modeling approach is, thus, termed meanline analysis: a single point, generally located at mid-span of the inlet and exit of each blade row represents the complex, time-variant, multidimensional flows inherent to turbomachinery. While the meanline approach is simplistic, it provides the fundamental characteristics of the flow that are necessary to achieve the desired performance for a new design. In fact, since the meanline equations determine the basic physics of any compressor, poor design choices or inaccurate performance predictions in the preliminary design phase cannot be remedied by optimization during detailed design with 3D simulations.

The meanline equations are given in various forms depending on the author and context of the application. In all cases, however, the meanline equations ultimately link the desired aerodynamic performance of a blade row to the basic geometry required to achieve that performance. Seven parameters are necessary to solve the system of equations at each station: (1) mass flux, (2-3) two thermodynamic state properties, (4-6) three-dimensional velocity vector, and (7) radial position of

the fluid element relative to the axis of rotation (Jones, 2014). The meanline equations are defined in equations (1.2) through (1.8) as given by Jones (2014):

$$\dot{m}_1 = \dot{m}_2, \tag{1.2}$$

$$h_{02} - h_{01} = U_2 V_{\theta 2} - U_1 V_{\theta 1}, \tag{1.3}$$

$$p_{02} = p_{02,I} - \overline{\omega}, \tag{1.4}$$

$$\beta_2 = \beta_{2b} + \delta, \tag{1.5}$$

$$r_2 = r_{design}, \tag{1.6}$$

$$A_2 = A_{design}, and \tag{1.7}$$

$$\gamma_b = \gamma_{b,design}, \tag{1.8}$$

where $\dot{m}$ is mass flow rate, h is enthalpy, p is pressure, $\overline{\omega}$ is the loss coefficient, β is the relative flow angle, δ is deviation, A is area, and γ_b is the meridional inclination angle with respect to the axial direction. The inlet and exit states for the blade rows are denoted by the subscripts 1 and 2, respectively, and correspond to the impeller inlet and exit stations given in Figure 1.3. The subscript 0 indicates the stagnation condition, I is the ideal condition (no work input is dissipated by entropy generation), θ indicates the tangential direction, and b is a parameter associated with the blade geometry. Finally, the $design$ subscript indicates a parameter that is fixed as part of the direct-design approach. In direct design, the stage geometry is set, and the performance is calculated. The meanline equations can also be used from the inverse-design approach, in which case the aerodynamic performance is specified, and the geometry required to achieve the desired performance is the result. Alternate formulations and extensive discussion of the meanline equations are given by Japikse (1996) and Whitfield & Baines (1990).

The meanline equations, which are the foundation of the 1D design approach, do not inherently account for non-ideal flow processes. Without the incorporation of models to simulate loss, $\bar{\omega}$ in equation (1.4), and flow deviation, δ in equation (1.5), the meanline equations give the solution for an idealized compression process, denoted by state $02_{I,PFG}$ in the Mollier diagram of Figure 1.4. This exit state is the result of an isentropic compression process in which the flow exactly follows the compressor blades: the perfect flow guidance (PFG) condition. The idealized compression process is not representative of the actual compression process from 01 to 02, and thus, models must be introduced to account for the deleterious flow phenomena that result in exit state 02. Loss models account for the entropy difference between the ideal exit state, 02_I, and the actual exit state, as well as the corresponding difference in total pressure between isobars $p_{02,I}$ and p_{02}.
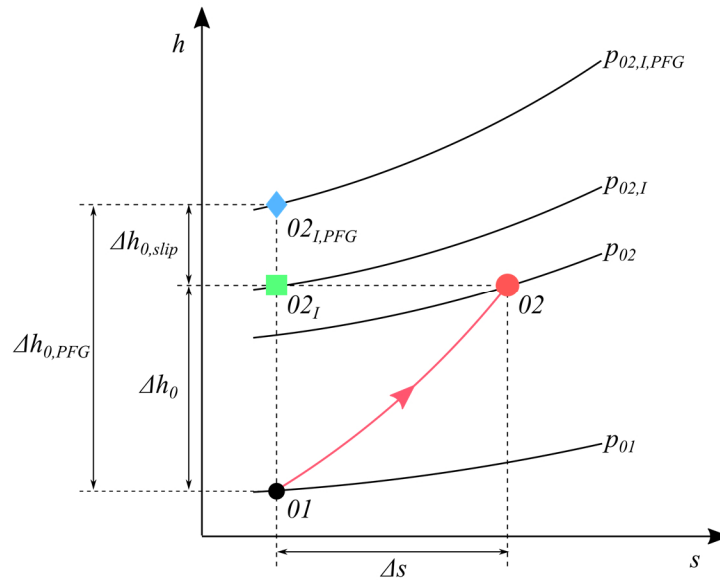
Figure 1.4: Mollier diagram showing the actual compression process as well as the ideal and ideal, PFG conditions.

The losses incurred by the centrifugal compressor impeller are generally split into two groups, internal and external losses. A conceptual breakdown of internal losses (orange) and external losses (violet) compared to the actual compression process (red, state 01 to state 02) is presented in Figure 1.5. Internal losses arise from entropy generation as a result of phenomena inherent to the compression process, such as skin friction, mixing, or incidence, and reduce the total pressure

available for a given enthalpy rise. External losses, often referred to as parasitic losses, are mechanisms that consume shaft work but do not contribute to the total pressure rise across the impeller. As such, external losses often arise from auxiliary mechanisms like recirculation of the flow or disk friction at the backface of the impeller.
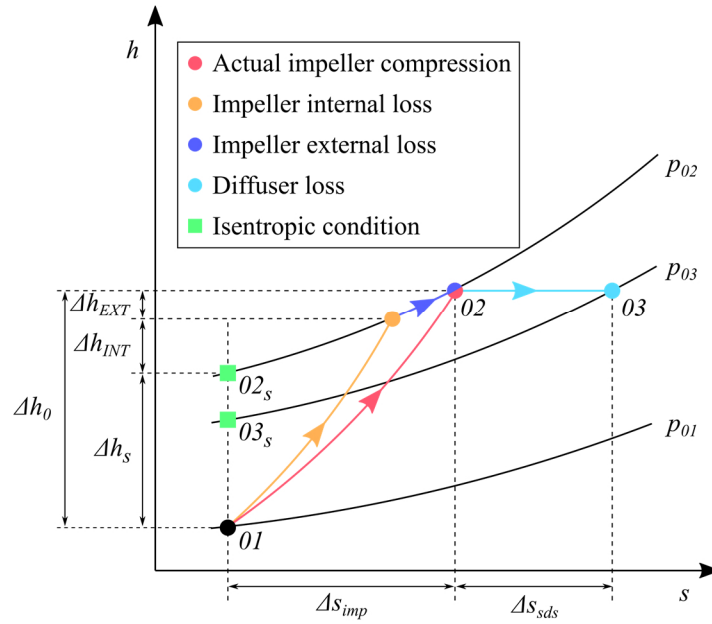
Figure 1.5: Breakdown of impeller internal losses, impeller external losses, and stationary diffusion system losses.

The losses associated with the stationary diffusion system (SDS), which may consist of various combinations of a vaneless space, vaned diffuser, vaneless diffuser, volute, and/or deswirl, are represented in light blue in Figure 1.5. Instead generating an enthalpy rise, the stationary diffusion system recovers static pressure from the high stagnation pressure flow at the impeller exit. The static pressure recovery process is accompanied by entropy generation from state 02 to state 03. The sum of the losses across the impeller and diffuser together determine the isentropic efficiency of the compression process.

Loss models are implemented in various ways as a function of the design approach. At the most basic implementation, loss is correlated with non-dimensional parameters such as specific speed and mass flow coefficient for preliminary estimates of efficiency at the design point (Casey &

Marty, 1986; Rodgers, 1979). Casey and Robinson (2012) recently expanded this method from exclusively design point prediction to estimation of the entire compressor map with the use of a few key nondimensional parameters. A second method utilizes performance correlations constructed from empirical data sets to evaluate component efficiencies for a previously tested design family. These correlations usually provide better accuracy than other loss models, but they require detailed knowledge of the component design family before beginning the design process. Lastly, numerous loss models are implemented to independently evaluate the loss associated with various deleterious flow phenomena, such as skin friction or incidence. The set of models required to completely evaluate the impeller loss through this approach is extensive and varies widely depending on the researcher or institution (Aungier, 1995; Coppage et al., 1956; Galvas, 1973; Herbert, 1980; Oh et al., 1997). Additionally, the models must be tuned to accurately reflect the performance of a particular design (Herbert, 1980).

An overview of flow phenomena often modeled for loss is provided here, and additional detailed reviews of loss models in meanline design are given by Oh, Yoon, & Chung (1997), Whitfield (1990), Aungier (1995), Aungier and Cassin (2003), and Chapter 2 of the present work. First considering the collection of commonly used internal loss models, incidence loss develops as a result of the adjustment of the flow upstream of the blades to the impeller leading edge, and, generally, increases as the magnitude of the difference between the relative flow angle and the impeller leading edge metal angle increase. The adjustment of the flow to the blockage caused by the blades themselves is often considered as a part of incidence loss, as well (Aungier & Cassin, 2003; Conrad et al., 1979; Petermann & Pfleiderer, 2013). Blade loading loss characterizes the pressure difference from the pressure side to the suction side of the impeller blades to estimate the loss associated with diffusion and boundary layer growth. Blade loading is a function of the impeller solidity and diffusion factor, and excessive loading is associated with large losses and boundary layer separation (Aungier & Cassin, 2003; Coppage et al., 1956; Jansen, 1967). Skin friction loss develops due to the interaction of the working fluid with solid boundaries throughout the impeller flow path and generally increases with increase mass flow rate (Coppage et al., 1956; Harley et al., 2013; Jansen, 1967). Impeller tip clearance losses are a function of the number of blades and the ratio of the clearance height to the blade height. Clearance losses have been related to passage velocities (Jansen, 1967) and blade loading (Aungier & Cassin, 2003). Mixing losses

are associated with the viscous diffusion that occurs as a result of the three-dimensional, unsteady, and rotational impeller flow (Dean & Senoo, 1960), and have often been modeled using sudden expansion analysis (Aungier & Cassin, 2003; Johnston & Dean, 1966).

Impeller external losses are included somewhat at the discretion of the user (Whitfield & Baines, 1990). In some cases, like in turbochargers, inclusion of loss through bearings and heat transfer may be appropriate. Disc friction loss models, which estimate the loss of shaft work due to fluid friction between the backface of the impeller and the stationary housing, should be included for comparison with most experiments (Aungier & Cassin, 2003; Daily & Nece, 1960). However, 3D computational fluid dynamics (CFD) models of centrifugal compressors rarely include the flow field at the backface of the impeller, so the disc friction losses should generally be neglected when comparing the meanline model to 3D simulations. Recirculation losses are intrinsic to the flow field, however, and must be included. The phenomenon of recirculation occurs at the impeller trailing edge as low momentum fluid is ejected from the impeller at near tangential flow angles, and due to the adverse pressure gradient, flows upstream back into the impeller reference frame. As the recirculation fluid moves upstream, entropy generation occurs and the fluid is re-worked by the compressor, resulting in absorption of shaft work without an accompanying increase in total pressure. Recirculation may also occur at the impeller leading edge near the blade tip. Losses associated with recirculation often become large and are the primary driver of efficiency reduction near stall (Aungier & Cassin, 2003; Coppage et al., 1956; Jansen, 1967; Oh et al., 1997; Stuart et al., 2017).

Unfortunately, explicit validation of each individual loss model is not possible. Various sources of loss may be conceptually considered as discreet flow processes, but rigorous separation of each loss phenomenon is not possible in experiments or three-dimensional simulations. While CFD models offer the opportunity to investigate local entropy generation, attributing the entropy generation to a specific phenomenon is difficult. For example, exact partitioning and quantification of the loss at the impeller leading edge to skin friction, tip clearance, and recirculation is not possible. At best, the losses in experiments and CFD can be allocated to entire stage components, like the impeller, diffuser, or vaneless space. Therefore, the loss collections must be considered in their entirety, tuned to match a specific impeller family, and extended to similar designs for best

predictive results. Context on the contribution of each loss model to the total loss can be considered, however (Thanapandi & Prasad, 1990). According to Harley et al. (2013), the relative magnitude of the loss arising from each of the incorporated impeller loss models considered was fairly similar, with the exception of recirculation which was quite large at low mass flow rates for all the loss collections investigated.

Blockage refers to a reduction in the effective flow area available in compressor passages and the last component of flow modeling in the impeller. The geometric area within blade passages is rarely representative of the effective area available to the flow: boundary layers and recirculation often produce regions of low momentum fluid where the mass flux through a meridional cross section is effectively zero. Thus, the effective area available to pass flow through the machine is often less than that of the geometric area, and velocity triangles are changed relative to a completely unblocked passage due to the effect of flow area on conservation of mass (Dixon & Hall, 2013). There are two fundamentally different approaches to the incorporation of blockage in meanline analysis. The first is that blockage must be modeled since there is effectively zero mass flux through the blocked region and the average fluid state is not valid for the zero-mass flux region. The opposite approach is that modeling blockage is fundamentally inconsistent with meanline analysis because the average fluid state at the inlet and exit of each blade row must be representative of the entire fluid region (Japikse, 1996). While some loss models incorporate a blockage factor for estimation of specific losses (Aungier & Cassin, 2003), very few blockage correlations to calculate the effect of blockage on velocity triangles are available in the open literature. Pampreen's (1981) and Aungier and Cassin's (2003) blockage models are the only approaches known to the author, and both have received minimal attention and validation since publication.

Only limited discussion of diffuser loss models is available in the open literature, and most of the published work is concerned with vaneless diffusers. Vaned diffuser loss models are unique to the blade shapes of each diffuser, and the vanes themselves often do not conform to NACA specifications. As such, loss models for vaned diffusers are generally proprietary and unavailable in the literature. Vaned diffuser models often correlate impeller exit flow conditions and the area

ratio of the diffuser passage. Both Japikse & Baines (1998) and Aungier & Cassin (2003) present design and analysis approaches for vaned, as well as vaneless, diffusers.

In contrast with vaned diffusers, vaneless diffusers are usually modeled through the fundamental mass, momentum, and energy equations. With a known inlet and exit radius, as well as known inlet conditions from the impeller exit, the diffuser is portioned into small steps, and the conservation equations are calculated at each step of increasing radius up to the diffuser exit. The primary modeling in vaneless diffuser performance is for estimation of the loss due to skin friction between the flow and diffuser. The vaneless diffuser model published by Stanitz (1952) may overpredict the loss of vaneless diffuser at small radius ratios but is quite accurate for large radius ratio designs (Stuart et al., 2015). Herbert (1980) presented a method similar to that of Stanitz, and more recently, a two-zone approach for vaneless diffuser flow was developed (Dubitsky & Japikse, 2008).

1.4   Slip in Centrifugal Compressors

While loss models account for the entropy difference between thermodynamic states 02 and $02_{I,PFG}$ in Figure 1.4, the difference in predicted exit stagnation enthalpy between the two states is due to the phenomenon of slip in centrifugal compressors. The maximum available work input for any centrifugal compressor occurs at the perfect flow guidance condition for which the impeller exit flow tangential velocity, $V_{\theta 2,PFG}$, is maximized, as shown in Figure 1.6. In this case, the exit relative flow angle, β_2, is identical to the impeller exit blade angle, β_{2b}, and the resulting tangential velocity is the difference between the impeller tip velocity, U_2, and the intended tangential velocity reduction due to backsweep, $V_{m2} \tan \beta_{2b}$ (for radially bladed impellers, the perfect flow guidance circumferential velocity is identical to the impeller tip velocity). While the reduction in tangential velocity achieved with backsweep is a design choice usually incorporated for improved stability and efficiency, the slip velocity, V_{slip}, is an unknown and, as shown by the Euler equation, has a direct impact on the total enthalpy rise delivered by the impeller:

$$q - w = \Delta h_0 = c_p \Delta T_0 = \Delta U V_\theta = U_2\big(V_{\theta 2,PFG} - V_{slip}\big) - U_1 V_{\theta 1}, \qquad (1.9)$$

31

where q is heat transfer, c_p is the specific heat of air at constant pressure, and T_0 is stagnation temperature. Since slip is an unknown required to solve the meanline equations, slip models are introduced to account for the reduction in impeller work input due to deviation of the flow from the blade exit angle.
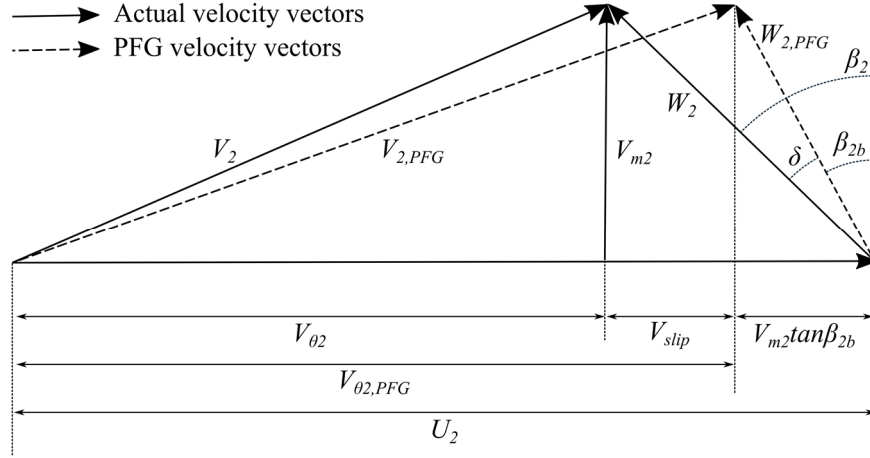
Figure 1.6: Impeller exit velocity triangle at actual and PFG conditions.

The flow phenomena that cause slip in centrifugal compressors are qualitatively well understood due to extensive research and analysis over the past century. The fundamental cause of slip is often explained from an inviscid perspective, though viscosity likely also contributes to slip in actual compressor operation. The theory of the relative eddy, which is the foundation of the vast majority of slip models available in the open literature, was originally presented by Stodola (1927) in the 1920's and is outlined in Figure 1.7. For the case of two-dimensional, steady, potential flow, there is no mechanism to generate or destroy vorticity, and irrotational flow entering the impeller must remain irrotational throughout the flow field (Greitzer et al., 2007). The bulk flow field in Figure 1.7a conveys the fluid through the impeller, but, while the fluid is within the impeller passages, the fluid is in a rotating reference frame. The condition of irrotationality must be maintained since vorticity can neither be created nor destroyed in potential flow fields. Therefore, a secondary flow develops in the impeller passages with an angular velocity equal and opposite to the angular velocity of the impeller reference frame, Figure 1.7b. The secondary flow, termed the relative eddy, satisfies the condition of irrotationality relative to the inertial reference frame. When

superimposed on the meridional bulk flow at the impeller exit, the relative eddy causes a reduction in the exit tangential flow velocity, i.e., slip, as shown in Figure 1.7. Stodola's original discussion was intentionally simplified and qualitative in nature, but numerous researchers later published exact solutions for the potential flow field in impeller passages in which slip was confirmed to be an inviscid phenomenon (Busemann, 1928; Greitzer et al., 2007; Hassenpflug, 2010; Reddy, 1954; Stanitz, 1949; Stanitz & Ellis, 1950).
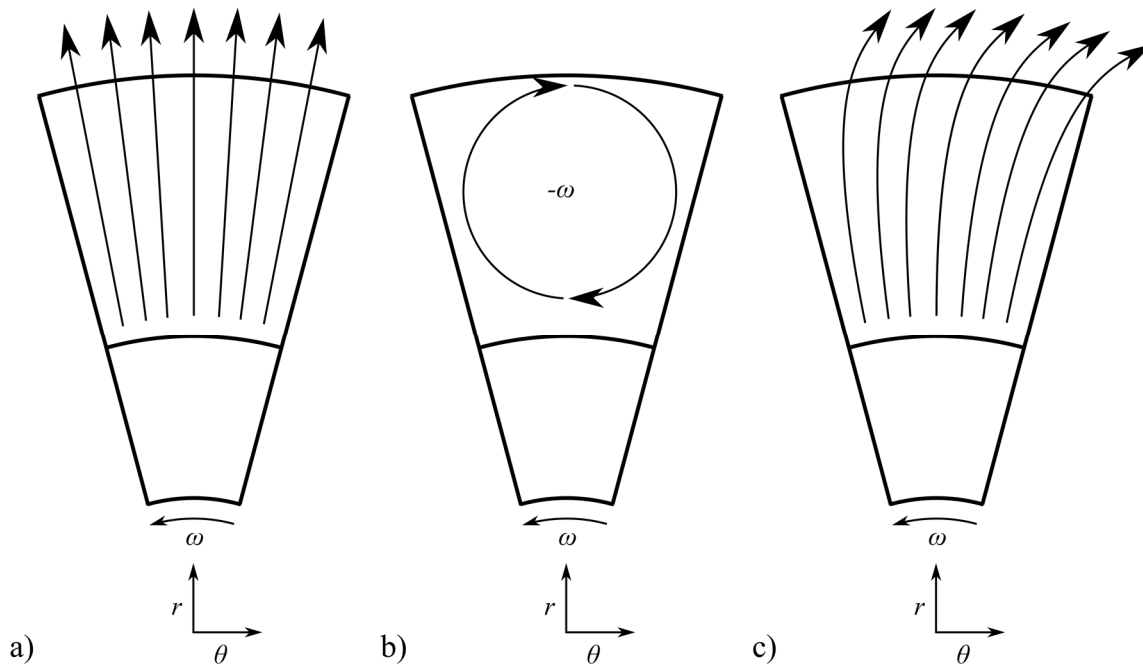
Figure 1.7: The potential flow approach to development of the relative eddy through superposition of a) the meridional flow field with b) the relative eddy which results in c) the inviscid solution of flow through an impeller showing slip at the impeller exit.

The reduction in blade loading at the trailing edge is an alternate and equivalent approach often used to explain the phenomenon of slip. Like in axial blades, the blade loading must decrease to zero at the impeller trailing edge to satisfy the Kutta-Joukowski condition. The gradual decrease in blade loading corresponds to a reduction in the pitchwise pressure gradient within the passage, from which a cross-passage velocity opposed to the direction of impeller rotation arises (Cumpsty, 1989; Qiu et al., 2011). Whether attributed to the relative eddy or relaxation of the cross-passage pressure gradient, the secondary flow within the passage is the root cause of the difference between

the actual velocity triangle and the ideal velocity triangle associated with the perfect flow guidance condition in Figure 1.6.

Many models have been developed to predict slip with almost all of them having some basis in Stodola's original approach which used the impeller geometry to predict the impeller exit tangential velocity reduction due to slip. Stodola's (1927) original work used the geometry of the impeller passage to estimate the size of the relative eddy, Figure 1.8. The radius of the relative eddy, r_e, is assumed occupy the entire width of the impeller passage and can, thus, be calculated according to equation (1.10),

$$r_e = \frac{r_2}{2} \sin \frac{2\pi}{Z} \tag{1.10}$$

from which the slip velocity, illustrated in Figure 1.6, can be calculated. In equation (1.10), r_2 is the impeller exit radius and Z is the impeller blade number. Since the angular velocity of the relative eddy and the impeller itself are equal in magnitude, both sides of equation (1.10) are multiplied by the angular velocity, ω, to obtain the slip velocity in terms of the impeller exit tip speed, equation (1.11):

$$V_{slip} = \omega r_e = \frac{\omega r_2}{2} \sin \frac{2\pi}{Z} = \frac{U_2}{2} \sin \frac{2\pi}{Z}. \tag{1.11}$$

For large impeller blade numbers the sine term in equation (1.10) can be approximated as

$$\sin \frac{2\pi}{Z} \approx \frac{2\pi}{Z}. \tag{1.12}$$

With the approximation in equation (1.12), the dimensionless representation of Stodola's slip model is obtained by nondimensionalizing the slip velocity with the impeller exit tip speed to develop the historical definition of the slip factor, σ:
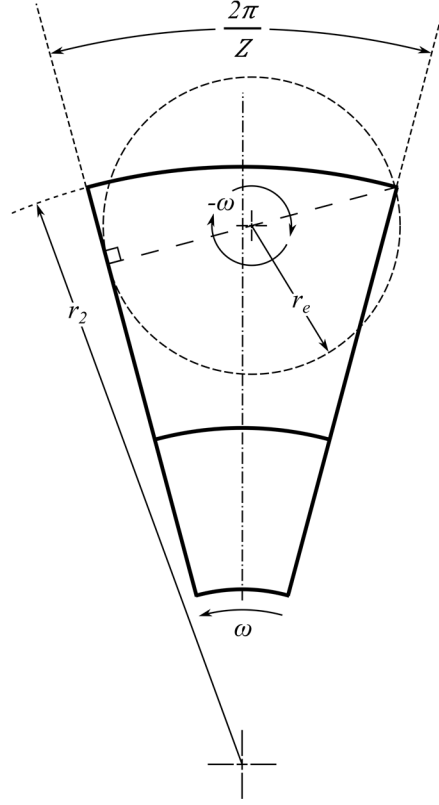
Figure 1.8: Reproduction of the sketch used by Stodola (1927) to evaluate the slip factor from the impeller geometry.

$$\sigma = 1 - \frac{V_{slip}}{U_2}. \tag{1.13}$$

The slip factor is substituted into equation (1.11) for the ratio of the slip velocity to the impeller exit tip speed to obtain the Stodola's slip model for radially bladed impellers:

$$\sigma = 1 - \frac{\pi}{Z}. \tag{1.14}$$

Equation (1.14) must be modified slightly for backswept impeller blades to account for the reduction in passage width at the impeller trailing due to backsweep, equation (1.15):

$$\sigma = 1 - \frac{\pi \cos \beta_{2b}}{Z}. \tag{1.15}$$

Shortly after Stodola's original publication, Busemann (1928) presented an analytical solution for two-dimensional potential flow in an impeller with logarithmic spiral blades. The Busemann solution is inherently more rigorous than Stodola's approach since it is based on a theoretical flow field rather than geometric relations. Additionally, the Busemann solution generally provided more accurate estimations of slip than Stodola's model. Busemann's approach was rarely used, however, due to the complexity of implementation in the design phase. Stodola's model requires only backsweep and blade number to solve a simple equation, while Busemann's logarithmic spiral blade potential flow solution must be adapted to actual impeller geometries to achieve a meaningful value for slip. As such, Stodola's model became the standard procedure for impeller design during the first half of the twentieth century.

The vast majority of slip models published since Stodola's and Busemann's proposals are based in the theory of the relative eddy and rely heavily on the impeller geometry to predict the slip factor. Reddy (1954) published a solution for radially bladed impellers using a similar approach to Busemann with potential flow theory. Stanitz (Stanitz, 1949; Stanitz & Ellis, 1950) published a correlation for slip factor based on a solution of two-dimensional, inviscid flow through a radially bladed impeller:

$$\sigma = 1 - \frac{0.63\pi}{Z}.$$
(1.16)

Stanitz's model yielded similar results to that of Stodola with a slightly lower magnitude, and, despite being derived specifically for radial blades, it has often been used for backswept impellers, as well (Stahler, 1965).

The landmark study in the investigation of slip is Wiesner's review in which a slip factor calculated from experimental flow measurements was compared to the predicted slip factor for more than 70 compressors and pumps (Wiesner, 1967). Wiesner developed a simple experimental correlation that emulated Busemann's (1928) mathematical results using only the blade exit angle, blade number, and impeller radii:

$$\sigma_W = 1 - \frac{\sqrt{\cos \beta_{2b}}}{Z^{0.70}}, \qquad \left(\frac{r_1}{r_2}\right)_{limit} < \epsilon = \exp\left(\frac{-8.16 \cos \beta_{2b}}{Z}\right). \qquad (1.17)$$

The correlation in equation (1.17) was satisfactory up to a limiting radius ratio, ϵ, of the impeller inlet tip radius, r_1, to impeller exit tip radius, r_2. In the cases that the radius ratio is exceeded, the correction in equation (1.18) is applied:

$$\sigma_{W,corr} = \sigma_W \left[1 - \left(\frac{\left(\frac{r_1}{r_2}\right) - \epsilon}{1 - \epsilon} \right)^3 \right]. \qquad (1.18)$$

Wiesner evaluated the accuracy of equation (1.17) and equation (1.18) relative to Busemann's solution, which the correlation was intended to match, as well as Stodola's and Stanitz's model. The predicted slip factor for each model was compared to an experimentally calculated slip factor, and the percentage of points within a relative error of ±5% of slip factor was quantified. Of the four approaches, Wiesner's correlation calculated the largest percentage of values for slip factor within the error band (88%), outperforming Busemann's original potential flow solution. Less than 60% of the data were predicted within the ±5% relative error band for Stodola's and Stanitz's models.

Since Wiesner's review, slip has remained a widely discussed topic in the field of centrifugal compressors. Hassenpflug (2010) presented a solution to the potential flow field of an impeller in the incompressible regime, as well as an extensive review of analytical solutions published to that point. The so-called "single relative eddy" (SRE) method was proposed by von Backström (2005) in which the relative eddy approach is implemented on the impeller as a whole rather than per blade passage. The SRE model proposes that blade solidity is the dominant parameter in the relative eddy and, by extension, the determination of slip. As such, the model is a function of the impeller exit solidity (the ratio of the blade length, L_c, to the blade spacing at the impeller trailing edge, s_2) and blade exit angle, β_{2b}:

$$\sigma_{VB} = 1 - \left(1 + F_{VB}\left(\frac{L_c}{s_2}\right)\cos^{0.5}\beta_{2b}\right)^{-1}. \tag{1.19}$$

The constant, F_{VB}, can be tuned to fit different impeller families. To improve the utility of the model in the meanline design process when the blade length may not yet be known, the author provides equation (1.20) as equivalent to solidity at the impeller trailing edge:

$$\frac{L_c}{s_2} = \frac{(1 - RR)Z}{2\pi\cos\beta_{2b}}, \qquad RR = \begin{cases} \frac{r_1}{r_2}, & \frac{r_1}{r_2} \geq 0.5 \\ 0.5, & \frac{r_1}{r_2} < 0.5 \end{cases}. \tag{1.20}$$

The tuning constant is beneficial in that the utility of the model is broadened, but it is also a detriment in comparing the efficacy of the model to predict slip factor across the design space. The SRE model performed similarly to Wiesner's model in the validations published by the author.

All the slip models discussed to this point rely only on the impeller geometry, and therefore, the flow conditions are neglected in these approaches. Yet, the preponderance of evidence shows that slip factor changes throughout a compressor's operating range (Cumpsty, 1989; Dean, 1971; Eckardt, 1980; Sakai et al., 1967; Stahler, 1965). Whitfield first addressed this inconsistency using the two-zone modeling approach to investigate the variation of slip factor with flow rate (Whitfield, 1974). However, Whitfield's method relies upon accurate representation of the actual diffusion factor achieved by the impeller which is not known in the preliminary design phase. Del Greco et al. proposed a model to calculate slip factor throughout the operating range based on the familiar parameters of blade exit angle, blade number, and solidity (Del Greco et al., 2009). The model was validated with numerous designs and operating points, but it relies on the calibration of 10 constants, which creates a significant barrier to its use.

Qiu et al. utilized the traditional geometric parameters to estimate the effect of the relative eddy, but they also incorporated the impeller exit flow coefficient and trailing edge curvature to account for the variation of slip at different operating conditions (Qiu et al., 2011). Qiu proposed that slip

is due to two primary factors: radial rotation and blade turning rate, which are defined respectively in terms of slip as

$$\Delta\sigma_{radial} = \frac{F_Q \pi \cos\beta_{2b} \sin\zeta_{2b}}{Z} \qquad (1.21)$$

and

$$\Delta\sigma_{turn} = \frac{F_Q s_2 \phi_2}{4\cos\beta_{2b}} \left(\frac{d\beta_b}{dm}\right)_2, \qquad (1.22)$$

where ζ_2 is the meridional inclinational angle at the impeller exit measured from the axial direction, and ϕ_2 is the impeller exit flow coefficient. The derivative in equation (1.22) is the blade turning rate (the rate of change of the blade angle per unit meridional distance) at the impeller trailing edge. A third component affecting slip, the passage width variation, is considered negligible in the original reference and, as such, is not included in the present work. Each of the components is dependent on a shape factor unique to every impeller, F_Q, defined as

$$F_Q = 1 - \sin\frac{\pi}{Z}\sin\left(\frac{\pi}{Z} + \beta_{2b}\right)\cos\beta_{2b}\sin\zeta_{2b} - \frac{t_2}{s_2\cos\beta_{2b}}, \qquad (1.23)$$

where t_2 is the thickness of the blade at the impeller trailing edge. Qiu indicates that the model is applicable only to impellers with inlet-to-exit radius ratios that are less than the shape factor. Finally, the slip factor according to Qiu's method is

$$\sigma_Q = 1 - \Delta\sigma_{radial} - \Delta\sigma_{turn}. \qquad (1.24)$$

Stuart et al. (Stuart et al., 2019) extended Qiu's model to a multi-zone technique. The authors used a recirculation model (Harley et al., 2014) to designate the impeller exit flow as the jet, wake, and recirculation zones to calculate the area of the "active flow region" which the relative eddy occupies.

Equation (1.13) is one of two commonly used definitions of the slip factor. An alternate definition of slip factor uses a ratio of the slip velocity to the perfect flow guidance impeller exit tangential velocity, but equation (1.13) will be used for the remainder of the present work for its utility in comparing slip at different impeller tip speeds. As the slip factor decreases, the amount of slip (the magnitude of the slip velocity) increases, and vice versa. Thus, an overprediction of slip factor, synonymous with an underprediction of slip or slip velocity, results in an overprediction of work input and impeller exit tangential flow velocity.

1.5   Research Objectives

Despite the continued advancement of high-fidelity computational simulations, one-dimensional modeling is a critical step of the centrifugal compressor design process. At the same time, reliable prediction of centrifugal compressor performance through one-dimensional modeling is elusive, especially when utilizing tools available in the open literature or in the absence of empirical datasets. As such, a generalized meanline model is developed for analysis of centrifugal compressors at design and off-design conditions. The meanline model is used to evaluate the efficacy of numerous slip models available in the open literature with respect to five centrifugal compressor cases with emphasis on the high-speed design space. A new method to model slip and work input for centrifugal compressors is developed through consideration of the thermodynamic perspective of the compression process rather than modeling behavior of the flow at the impeller exit, as is typical of most models currently available in the open literature.

The Object-oriented Turbomachinery Analysis Code (OTAC) environment within the Numerical Propulsion System Simulation (NPSS) computational framework is utilized to develop and validate a generalized meanline model for centrifugal compressors. Of the five centrifugal compressors cases simulated in the general meanline model, four are documented in detail in the open literature. The five cases represent a broad survey of the centrifugal compressor design space with emphasis on high-speed impellers. Many loss models and slip models available in the open literature are incorporated into the meanline model, and an existing centrifugal compressor case in the open literature is used to validate the model. Validation of the meanline model also serves as

validation for OTAC to conduct off-design calculations for centrifugal compressors which has not been previously documented.

The efficacy of slip models derived from the theory of the relative eddy is investigated in terms of accuracy in prediction of centrifugal compressor work input at both design and off-design conditions. One-dimensional data for the open literature compressors is generated by quantifying the slip and loss necessary to match the experimentally measured performance. The experimental values of slip factor are compared to that predicted by various models available in the open literature. The error propagation from misprediction of slip factor to error in the prediction of work input is investigated, and the unique challenges associated with predicting the work input for high-speed impellers are discussed. In the process, the trend of slip factor with various dimensionless design parameters is developed.

Finally, a new method to predict the slip factor and work input for high-speed impellers is developed. Stodola's (1927) original method used geometry to predict the size of the relative eddy, and by extension, the slip factor associated with a given impeller design. Most models available in the literature have followed Stodola's approach and primarily rely on the impeller geometry to predict the behavior of a highly unsteady, three-dimensional flow field at the impeller exit (Qiu et al., 2011; Stahler, 1965; Stanitz, 1949; Stuart et al., 2017; von Backström, 2005; Wiesner, 1967). Due to errors and inconsistencies in predicting the behavior of a complex flow field chiefly from geometry, as well as limited success in predicting slip at off-design conditions, there is significant room for improvement in the prediction of slip factor. Therefore, a model is proposed that utilizes thermodynamic principles in conjunction with the meanline equations, rather than flow modeling, to predict work input and slip factor at design and off-design conditions.

2. A GENERALIZED MEANLINE MODEL FOR CENTRIFUGAL COMPRESSORS

A generalized meanline model for centrifugal compressors was developed in the OTAC environment within the NPSS computational framework (Jones, 2014, 2015; *Numerical Propulsion System Simulation (NPSS)*, 2016) with the goal of investigating centrifugal compressor performance from a one-dimensional design perspective. NPSS is an object-oriented code built around a linear solver and is intended for use in thermodynamic cycle design and analysis. Various elements, such as the inlet, compressor, combustor, turbine, etc., are typically built up to model a gas turbine engine. The elements are linked together at flow stations that represent the fluid state at the inlet and exit of each component in the system. Since NPSS is object oriented, each element may contain various subelements that each contain additional subelements or functions that provide data to the top-level component. A turbine element may contain performance maps that support interpolation of efficiency and pressure ratio based on mass flow rate and the inlet and exit total temperatures, or inlet components might contain models to estimate pressure recovery based on the free stream Mach number.

The NPSS framework features a built-in linear solver that varies user-defined independent quantities to satisfy the constraints of additional user-defined dependent quantities. Since the user defines the solver setup, dependent quantities can be defined as aerodynamic performance parameters or geometry, and the independent quantities are manipulated to satisfy governing relationships, such as conservation of mass and momentum. A Jacobian matrix is constructed by the solver, and each independent quantity is perturbed with the goal of reducing the error of each dependent condition to within a user-specified tolerance. Additional details on the linear solver and structure of NPSS are available in the NPSS User's Guide (*Numerical Propulsion System Simulation (NPSS)*, 2016).

OTAC provides a direct link within NPSS between thermodynamic cycle design and turbomachinery component analysis. The object-oriented approach of NPSS, which uses elements with flow stations at the inlet and exit of each element, is naturally extended to meanline design

and analysis in OTAC. The functionality of OTAC is fundamentally similar to that of NPSS, but elements are composed of blade rows rather than engine level components. The blade row elements contain the information necessary for meanline analysis, such as blade geometry, rotational speed, flow models, etc. The independent quantities and dependent quantities of each blade row are structured to allow the solver to satisfy the meanline equations given in equations (1.2) to (1.8). The linear solver can iterate on the meanline equations from a direct-design or inverse-design approach at design or off-design conditions based on the solver setup. Further documentation on OTAC and baseline validation of the code is available in references published by the author (Jones, 2014, 2015).

Four well documented centrifugal compressor cases available in the open literature were modeled in OTAC: Krain's transonic impeller stage (SRV2-O), NASA's low specific speed impeller (CC3), Came's transonic backswept impeller (Came stage B), and Eckardt's backswept impeller (Eckardt impeller A). Additionally, the data set available from the Honeywell Test Single Stage Centrifugal Compressor (SSCC) facility was utilized as a validation case. The Honeywell SSCC is a test vehicle operated at Purdue University and is outfitted with a wide array of instrumentation for various research purposes. The primary design point performance and geometric parameters of each stage are given in Section 2.1, as well as the geometric parameters necessary to incorporate each compressor into a meanline model. Further documentation for each of the stages can be found in the references (Came, 1978; Came & Herbert, 1980; Eckardt, 1978, 1980; Eisenlohr et al., 2002; Krain et al., 1995; Kulkarni et al., 2013; Lou, 2016; Lou et al., 2016; Mangani et al., 2012; McKain, 1997; Skoch et al., 1997). The five stages represent a broad survey of the centrifugal compressor design space with emphasis on high-speed speed designs. Many of the loss models available in the open literature for centrifugal compressor impellers are incorporated into the model, as well as numerous slip models, to support modeling of each stage. A model for loss through vaneless diffusers is also included. The resultant meanline model is then validated through comparison of Eckardt's impeller A with the loss collection published by Oh et al. (1997). The model validation case also serves as validation for the off-design utility of OTAC for centrifugal compressors, a capability which has not been previously documented.

2.1 Centrifugal Compressor Cases

The five centrifugal compressor cases modeled in OTAC represent a broad survey of the centrifugal compressor operating space, as shown by the maps of each open literature compressor in Figure 2.1. The design point aerodynamic specifications of each impeller are given in Table 2.1 to accompany the comparison of the compressor operating ranges in Figure 2.1. The definition of specific speed utilized in Table 2.1 and through the remainder of the manuscript is

$$N_s = \frac{\phi_1^{0.5}}{\psi^{0.75}}. \tag{2.1}$$

The inlet flow coefficient, ϕ_1, and loading coefficient, ψ, are defined as

$$\phi_1 = \frac{\dot{m}}{\rho_{01} D_2^2 U_2} \tag{2.2}$$

and

$$\psi = \frac{\Delta h_0}{U_2^2}, \tag{2.3}$$

respectively.

The Krain and Came impellers are both transonic, high-speed impeller designs. They provide the largest pressure ratios of the four open literature stages, but they occupy different design spaces: Krain's impeller has a high specific speed while Came's impeller has a low specific speed. The NASA impeller is a lower pressure ratio machine, with a specific speed between that of Krain's and Came's impellers. Eckardt's impeller has both the lowest speed and pressure ratio and, thus, is not as representative of aerospace applications. However, Eckardt's studies are widely documented, referenced, and used as validation cases throughout the centrifugal compressor literature. Eckardt's impeller is, therefore, included in the present analysis for comparison of the present work with that of past studies, as well as to extend the present analysis across high- and
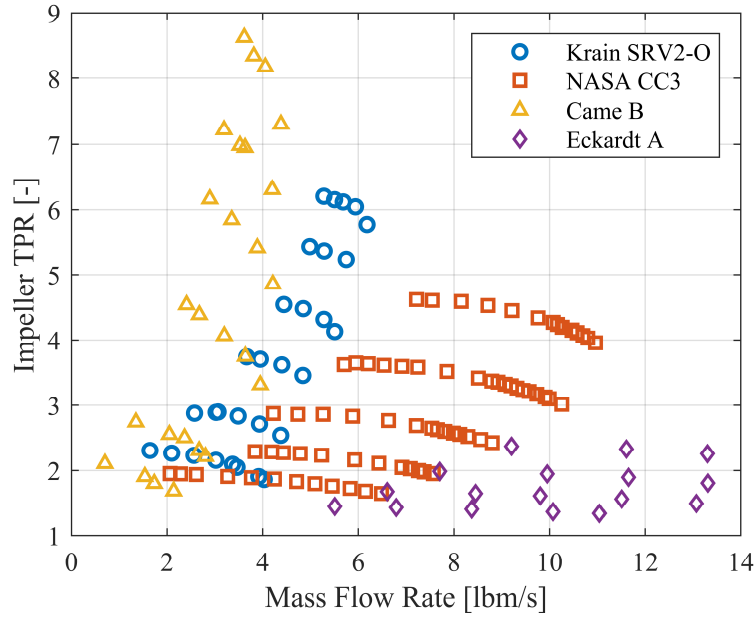
Figure 2.1: Impeller total pressure ratio of open literature centrifugal compressors as calculated from OTAC.

low-speed designs. The final compressor included in the analysis, the Honeywell SSCC, is also a high-speed stage. The vaneless diffuser configurations of each of the open literature compressors are the primary focus of the current work, and as such, much of the proceeding discussion is concentrated on the impeller.

The meridional profiles of each impeller are also indicative of the differences in each impeller design, Figure 2.2. With increasing impeller rotational speed, the inducer tip radius generally decreases to minimize the effect of shock losses at the inducer tip (Japikse, 1996). In contrast, the impeller exit radius increases with decreasing rotational speed to take advantage of reduced mechanical stresses and the centrifugal effect on pressure rise through the impeller. The differences in exit radii and mechanical speed between each of the impellers result in significant variation of the machine Mach number amongst the four stages. The machine Mach Number, or tip-speed Mach number, signifies the general operating regime of each stage and is defined according to equation (2.4):

Table 2.1: Aerodynamic design point parameters of the open literature impellers.

Parameter	Units	Krain SRV2-O	NASA CC3	Came B	Eckardt A	Honeywell SSCC
Mass Flow Rate	lbm/s	5.6	10.0	4.0	13.2	-
Pressure Ratio	-	6.1	4.2	8.1	2.3	~7.5
Efficiency	%	84.0	86.7	87.0	85.0	-
Rotational Speed	rpm	50,000	21,789	40,000	16,000	~45,000
Specific Speed	-	0.38	0.27	0.23	0.38	0.27
Machine Mach Number	-	1.72	1.44	1.69	0.98	~1.7
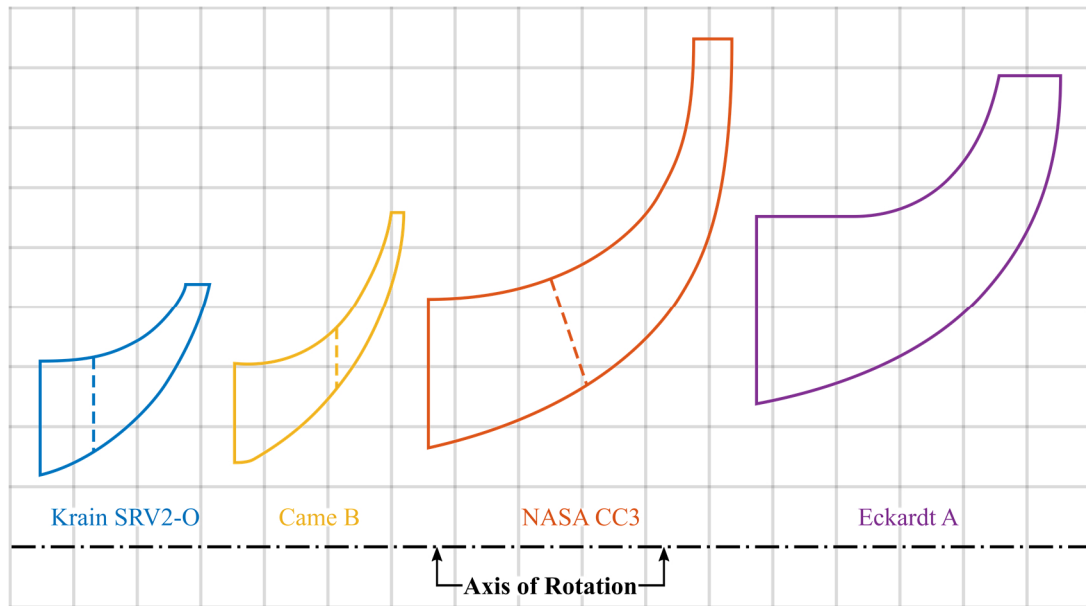
Figure 2.2: Meridional profile of each open literature impeller, drawn to scale, with grid spacing of 1 inch by 1 inch, axis of rotation indicated by the black dash-dot line, and splitter vane leading edges indicated by dashed lines.

$$M_{U2} = \frac{U_2}{\sqrt{\gamma R T_{01}}}, \qquad\qquad (2.4)$$

where M_{U2} is the machine Mach number, γ is the ratio of specific heats, R is the ideal gas constant, and T_{01} is the stagnation temperature at the impeller inlet. According to Casey and Robinson (2012), industrial compressors operate in the lowest ranges of machine Mach number, between 0.5 and 1.0. Turbochargers have a broader possible range, from 0.5 to 1.5, and they can reach machine Mach numbers as large as 1.7 for large diesel engines. Aerospace and refrigeration applications typically operate with machine Mach numbers from 1.0 to 2.0. Thus, the five selected impellers are representative of a broad survey of designs, particularly for high-speed aerospace applications.

Geometric parameters of the leading edge, blades, and trailing edge of each impeller are given in Table 2.2, Table 2.3, and Table 2.4, respectively. All parameters required to calculate the stage performance and/or apply the included slip and loss models are defined. The inlet and exit blade angles are measured from the axial and radial directions, respectively. Each of the tables includes

Table 2.2: Leading edge geometric parameters of the open literature impellers.

Parameter	Units	Krain SRV2-O	NASA CC3	Came B	Eckardt A
Hub Radius	inch	1.18	1.63	1.20	2.36
Shroud Radius	inch	3.07	4.13	2.65	5.51
Inducer Hub-to-Tip Radius Ratio	-	0.385	0.395	0.453	0.429
Radial Clearance	inch	0.020	0.012	-	0.020
Shroud Blade Angle	degree	63.5	53.7	53.8	60.0
Hub Blade Angle	degree	37.1	27.2	31.4	38.9
Shroud Blade Thickness	inch	0.049	0.076	0.070	0.031
Hub Blade Thickness	inch	0.070	0.133	0.098	0.247

Table 2.3: Blade parameters of the open literature impellers.

Parameter	Units	Krain SRV2-O	NASA CC3	Came B	Eckardt A
Shroud Axial Length to Shroud Radius Change Ratio	-	1.90	1.04	1.11	1.72
Blade Count (Main/Splitter)	-	13/13	15/15	17/17	20
Meridional Length	inch	3.85	8.26	5.42	7.09
Change in Blade Angle per Unit Meridional Length at Meanline	rad/inch	-0.001	-0.131	-0.022	-0.229

Table 2.4 Trailing edge geometric parameters of the open literature impellers.

Parameter	Units	Krain SRV2-O	NASA CC3	Came B	Eckardt A
Exit Radius	inch	4.41	8.48	5.41	7.87
Backsweep	degree	38	50	30	30
Average Blade Thickness	inch	0.070	0.104	0.081	0.235
Exit b-Width (Blade Height + Clearance)	inch	0.390	0.683	0.241	1.051
Exit Axial Clearance	inch	0.012	0.012	0.090	0.028

parameters that are not explicitly given in the original publication but can be derived from provided coordinates or profiles. Of the tabulated quantities, the inducer radius ratio, exit radius, exit blade height, and backsweep are critical for calculation of the stage performance. The inducer radius ratio governs the inlet flow coefficient of each stage, and the exit radius and backsweep, along with slip, determine the work input provided by the impeller. Each of the impellers in the present work incorporate backsweep, including the SSCC impeller which has a backsweep angle of 45

degrees. Diffusion through the impeller, often measured with the impeller relative velocity ratio, is governed by the impeller exit blade height.

The geometry of each vaneless diffuser is given in Table 2.5. The radius ratio is the ratio of the vaneless diffuser exit measuring station, as defined in each of the references, to the impeller exit radius. The b-width ratio is also defined from the vaneless diffuser measuring station to the impeller exit and is the ratio of the passage height at each location. The vaneless diffuser configurations in Krain's and Eckardt's and experiments utilized constant-area vaneless diffusers to minimize the effect of the diffuser on the impeller performance. The short configurations used in the NASA and Came experiments isolated the impeller performance by placing the measuring station just downstream of the impeller to minimize the losses. The performance of the CC3 impeller was directly measured with total pressure and total temperature rakes at a radius ratio of 1.18, but structural integrity of probes and the effect of highly unsteady flow on measurements for the high pressure ratio Came impeller was a concern. Instead of directly measuring the total conditions just downstream of the impeller, total conditions at the vaneless diffuser exit farther downstream were measured, and static pressure taps at the 1.065 radius ratio were utilized to calculate the impeller total pressure ratio. Vaneless diffuser models are not applicable for the Honeywell SSCC, but the impeller total pressure ratio and efficiency were calculated from the impeller exit static pressure measurements and diffuser exit conditions. Since the impeller is the primary focus of the present investigation, the one-dimensional model included only up to the impeller exit measurement station rather than incorporating a model for the vaned diffuser.

Table 2.5 Vaneless diffuser geometric parameters of the open literature centrifugal compressors.

Parameter	Units	Krain SRV2-O	NASA CC3	Came B	Eckardt A
Radius Ratio	-	1.98	1.18	1.065	1.687
b-Width Ratio	-	0.50	0.92	0.90	0.59

2.2 Model Structure

The one-dimensional model of each compressor was constructed by specifying the stage geometries in Table 2.2, Table 2.3, Table 2.4, and Table 2.5 within the appropriate OTAC elements. Standard day conditions are provided as total conditions at the inlet in the "OTACStart" element, which serves as a source term, with an area equivalent to that of the impeller inducer. A loss-free inlet guide vane (IGV) is included upstream of the impeller in a "BladeRow" element to impart pre-whirl to the flow if desired. BladeRow elements require metal angles to support solving the Euler turbomachinery equation, but vaneless diffusers do not contain blades. Therefore, the "DuctGap" element is more amenable to vaneless diffuser geometry since it only requires the area change between the inlet and exit flow stations to satisfy conservation of momentum.

The NPSS top level solver proceeds from the most upstream component downstream through each element of the model. The individual elements host local solvers that iterate on the equations necessary to fully define the fluid state at the inlet and exit flow stations of the elements. The BladeRow and DuctGap elements of OTAC were significantly modified to accommodate the unique geometric characteristics of centrifugal compressor impellers and diffusers. The inlet flow station of each element inherits the properties of the upstream elements, but the area at the exit flow stations of the BladeRow and DuctGap elements must either be defined as a design parameter or calculated from the inverse design approach. In the version of OTAC used in the present work, the exit flow stations operate with the assumption of an annular flow path and calculate the exit area of the flow stations based on the difference between the hub radius and shroud radius. Both the BladeRow and DuctGap components were modified to calculate the exit area for a span perpendicular to the radial, rather than axial, direction, as well as to track the radial and axial coordinates of the radial flow path. The DuctGap segment was also altered to accept loss models because its default properties assume a lossless, annular flow path. Minor changes were also made to the "StreamSegment" element to accept the reworked exit flow station area calculations.

Typically, loss is specified in terms of static enthalpy, total enthalpy, or total pressure and is often given as a nondimensional loss coefficient. OTAC was written to accept various definitions of loss coefficients, but many of the classic impeller loss models are specified in terms of total enthalpy

50

loss which is not available in the default OTAC calculations. Therefore, prior to incorporating loss models, the OTAC source code was modified to accept dimensional enthalpy loss. An additional external loss element was also developed to separately quantify impeller internal and external losses.

2.3   Impeller Loss Models

The basis of each impeller internal loss model incorporated into the general meanline model is given in the proceeding tables, and nomenclature is provided in the Nomenclature section at the beginning of this document. When possible, multiple loss models for each loss mechanism were incorporated to allow users to choose the loss models best suited for their application. Some loss models use the same terms but define the terms differently. For example, several models use a typical definition of blade length: the meridional distance from the impeller leading edge mid-span to the impeller exit mid-span. Other models give a particular definition of blade length specifically for use with that model. For clarity, all terms required for the loss models are explicitly defined within the relevant rows of each table. Empirical loss coefficients, indicated by K with various subscripts, are included in the original formulation of some models. Suggested values from the literature are provided where available, but the exact values of each coefficient are a function of the impeller design. Additional information on each loss model is available in each of the provided references.

Both impeller incidence loss models in Table 2.6 estimate the total enthalpy loss based on the adjustment the incoming flow must make to align with the impeller blade angle. The adjustment is a function of the inlet mass flow rate, rotational speed, and radial location along the span. Aungier's (1995) model uses a weighted average based on spanwise location to estimate the incidence loss with the mean radius having the largest influence. The incidence model originally published by Petermann & Pfleiderer (2013) and popularized by Conrad et al. (1979) uses only the root mean square radius. The optimum relative flow angle, $\beta_{1,opt}$, is determined from the inducer blade angle but accounts for the adjustment the flow must make to align with the blades from the area just upstream of the inducer leading edge, A_{1-}, to the area just downstream of the inducer leading edge, A_{1+}, where blades occupy part of the annular area. Additional details on the

calculation of the optimum inlet flow angle are given by Conrad et al. (1979), Galvas (1973), and Whitfield & Baines (1990). Similar models that calculate incidence loss based on the adjustment of the flow to the blades were also independently developed by NASA (Futral & Wasserbauer, 1965; Galvas, 1973; Todd & Futral, 1969).

Table 2.6: Impeller incidence loss models included in the meanline model.

Reference	Equation
Conrad et al. (1979) Petermann & Pfleiderer (2013)	$\Delta h_{0,inc} = \dfrac{K_{inc}}{2} \left(W_1 \sin \lvert \beta_1 - \beta_{1,opt} \rvert \right)^2$ $\beta_{1,opt} = \text{atan} \left(\dfrac{A_{1-}}{A_{1+}} \right) \tan \beta_{1b}$ $0.5 \le K_{inc} \le 0.7$
Aungier (1995)	$\Delta h_{0,inc,r} = 0.4 \left(W_1 - \dfrac{V_{m1}}{\sin \beta_1} \right)^2 \Big\vert_{r=r_{1h},r_{1m},r_{1t}}$ $\Delta h_{0,tot} = \dfrac{\Delta h_{0,inc,h} + \Delta h_{0,inc,t} + 10 \Delta h_{0,inc,m}}{12}$

The relative velocity is commonly used to estimate the blade loading losses of an impeller, as shown in the models in Table 2.7. Coppage et al. (1956) used the ratio of the impeller exit relative velocity to the inducer tip relative velocity to develop an impeller diffusion factor analogous to the axial compressor diffusion factor (Lieblein et al., 1953). In contrast to the diffusion factor approach, Aungier (1995) calculates loss from blade loading based on the difference between the suction side and pressure relative velocities of the impeller blades and the blade loading coefficient.

The methods to calculate the skin friction loss provided by Coppage et al. (1956) and Jansen (1967) rely on calculation of a skin friction coefficient, Table 2.8. While the models themselves are straightforward, many diverse methods can be used to compute the skin friction coefficient from sand grain roughness. Each method is likely to result in a unique value which is typical of

Table 2.7: Impeller blade loading loss models included in the meanline model.

Reference	Equation
Coppage et al. (1956)	$$\Delta h_{0,BL} = 0.05 D_f^2 U_2^2$$ $$D_f = 1 - \frac{W_2}{W_{1t}} + \frac{K_{D_f}\psi_b}{\frac{W_{1t}}{W_2}\left(\frac{Z}{\pi}\left(1 - \frac{r_{1t}}{r_2}\right) + \frac{2r_{1t}}{r_2}\right)}$$ $$K_{D_f} = \begin{cases} 0.6, with\ splitters \\ 0.75, no\ splitters \end{cases}, \text{ according to Galvas (1973)}$$
Aungier (1995)	$$\Delta h_{0,BL} = \frac{(\Delta W)^2}{48}$$ $$\Delta W = W_{SS} - W_{PS} = \frac{2\pi D_2 U_2 \psi_b}{Z_{eff}L_c}$$ $$Z_{eff} = Z_{MB} + \frac{L_{SB}}{L}Z_{SB}$$

roughness calculations. Furthermore, sand grain roughness is rarely specified in mechanical drawings. Instead, roughness usually is specified by another measure, such as average roughness, and there are a myriad of correlations available to convert from the specified mechanical tolerances to sand grain roughness (Forster, 1966; Grein, 1975; Musgrave, 1979; Simon & Bülskämper, 1984). Generally, the average roughness of a machined surface varies from a factor of one to three times that of the sand grain roughness (Grein, 1975).

While the ambiguity in calculation of the skin friction coefficient for centrifugal compressors is not ideal from a scientific perspective, loss models must always be tuned for accuracy, so exact replication of the methods is not critical. In the present work, the skin friction coefficient was calculated from the Colebrook-White equation adapted for use in centrifugal compressors,

Table 2.8: Impeller skin friction loss models included in the meanline model.

Reference	Equation

Coppage et al. (1956)

$$\Delta h_{0,SF} = \frac{K_{SF} C_f \left(\frac{L_{SF}}{D_2}\right)}{\frac{D_h}{D_2}} \left(\frac{W}{U_2}\right)^2_{AV} U_2^2$$

$$\frac{L_{SF}}{D_2} = \frac{1 - D_1}{2 \cos \beta_{2b}}$$

$$\frac{D_h}{D_2} = \frac{1}{\frac{Z_2}{\pi \cos \beta_{2b}} + \frac{D_2}{b_2}} + \frac{\frac{D_{1t}}{D_2}}{\frac{2}{1 - \lambda} + \frac{2Z_2}{\pi(1 + \lambda)} \sqrt{1 + \tan^2 \left(\frac{\beta_{1t,b}}{2} (1 + \lambda^2)\right)}}$$

$$\left(\frac{W}{U_2}\right)^2_{AV} = \frac{1}{2} \left[\phi_1^2 + \left(\frac{D_1}{D_2}\right)^2 + \left(\frac{W_2}{W_{1t}}\right)^2 \left(\phi_1^2 + \left(\frac{D_{1t}}{D_2}\right)^2\right)\right]$$

$$\lambda = \frac{r_{1h}}{r_{1t}}$$

$$K_{SF} = \begin{cases} 7.0, & with\ splitters \\ 5.6, & no\ splitters \end{cases}, \text{ according to Galvas (1973)}$$

Jansen (1967)

$$\Delta h_{0,SF} = 2 C_f \frac{L}{D_h} \overline{W}^2$$

$$\overline{W} = \frac{1}{4} (2W_2 + W_{1t} + W_{1h})$$

$$L_{SF} = \frac{\pi}{8} \left(D_2 - \frac{D_{1t} + D_1}{2} - b_2 + 2L_z\right) \left(\frac{2}{\frac{\cos \beta_{1t,b} + \cos \beta_{1h,b}}{2} + \cos \beta_{2b}}\right)$$

$$\frac{D_h}{D_2} = \frac{\cos \beta_2}{\frac{Z}{\pi} + \frac{d_2 \cos \beta_{2b}}{b_2}} + \frac{\frac{1}{2}\left(\frac{D_{1t}}{D_2} + \frac{D_{h1}}{D_2}\right)(\cos \beta_{1t,b} + \cos \beta_{1h,b})}{\frac{Z}{\pi} + \frac{D_{1t} + D_1}{D_{1t} - D_1}\left(\frac{\cos \beta_{1t,b} + \cos \beta_{1h,b}}{2}\right)}$$

$$\frac{1}{\sqrt{4C_f}} = 1.74 - 2\log_{10}\left(\frac{2k_s}{D_h} + \frac{18.7}{Re\sqrt{4C_f}}\right), \tag{2.5}$$

as given by Casey (1985) and Moody (1944). In equation (2.5), C_f is the friction coefficient, k_s is the sand grain roughness, D_h is the hydraulic diameter, and Re is the Reynolds number. The Reynolds number for centrifugal compressor flow used in equation (2.5) is based on the impeller exit tip speed and blade height:

$$Re = \frac{U_2 b_2}{\nu_1}, \tag{2.6}$$

where b_2 is the impeller exit span and ν_1 is kinematic viscosity at the impeller inlet. A similar procedure is incrementally outlined by Suhrmann, Peitsch, Gugau, Heuer, & Tomm (2010): the Colebrook-While equation is first modified for use in curved pipes and then for use in turbomachinery (Musgrave, 1979; Schlichting & Gersten, 2016). The hydraulic diameter is calculated according to the procedure published by each author. As a much simpler alternative, the hydraulic diameter of the impeller can be approximated as

$$D_h \approx 2b_2 \tag{2.7}$$

according to Casey (1985).

The impeller tip clearance loss models given in Table 2.9 utilize sudden expansion analysis as well as blade loading to estimate the entropy generation of the fluid that passes between the impeller blades and the shroud. The leakage flow undergoes a rapid contraction as it approaches the pressure side of the blade followed by a rapid expansion at the suction side exit of the tip clearance gap.

Mixing loss models predict the viscous mixing losses that occur in the diffuser as a result of the nonuniformity of the impeller discharge flow. Both the jet-wake structure of impeller passage flow and the wakes of the blades themselves mix out and generate entropy downstream of the impeller

Table 2.9: Impeller tip clearance loss models included in the meanline model.

Reference	Equation
Jansen (1967)	$$\Delta h_{0,CL} = 0.6 \frac{V_{\theta 2}\epsilon_{TC}}{b_2} \sqrt{\frac{4\pi V_{\theta 2}V_{m1}}{b_2 Z}\left(\frac{r_{1t}^2 - r_{1h}^2}{(r_2 - r_{1t})\left(1 + \frac{\rho_2}{\rho_1}\right)}\right)}$$
Aungier (1995)	$$\Delta h_{0,CL} = \frac{\dot{m}_{CL}\Delta P_{CL}}{\dot{m}\rho_1}$$ $$\Delta P_{CL} = \frac{\dot{m}(r_2 V_{\theta 2} - r_1 V_{\theta 1})}{Z_{eff}\bar{r}\bar{b}L_c}$$ $$Z_{eff} = Z_{MB} + \frac{L_{SB}}{L}Z_{SB}$$ $$\bar{r} = \frac{r_1 + r_2}{2}$$ $$\bar{b} = \frac{b_1 + b_2}{2}$$ $$\dot{m}_{CL} = \rho_2 Z_{eff}\epsilon_{TC}LU_{CL}$$ $$U_{CL} = 0.816\sqrt{\frac{2\Delta P_{CL}}{\rho_2}}$$

exit (Dean & Senoo, 1960; Johnston & Dean, 1966; Thanapandi & Prasad, 1994). The losses actually occur in the diffuser, but the nonuniform flow field arises from Coriolis forces, curvature, and unsteadiness dependent upon the impeller, and thus, are considered impeller losses. Like in tip clearance loss models, abrupt expansion analysis is used to develop the mixing loss models included in Table 2.10. Calculation of the wake width, ϵ_{wake}, in Johnston and Dean's (1966) model is not specifically defined, and unfortunately, determination of the wake width at the impeller exit is a somewhat byzantine process. The most robust methods to determine the wake width are cumbersome for 1D design: the shroud profiles, as well as the impeller diffusion ratio, must be

Table 2.10: Impeller mixing loss models included in the meanline model.

Reference	Equation
Johnston & Dean (1966)	$$\Delta h_{0,MIX} = \frac{1}{1+\tan^2\alpha_2}\left(\frac{1-\epsilon_{wake}-b^*}{1-\epsilon_{wake}}\right)^2 \frac{V_2^2}{2}$$ $$b^* = \frac{b_3}{b_2}$$
Aungier (1995)	$$\Delta h_{0,MIX} = \frac{1}{2}\left(W_{sep}-W_{out}\right)^2$$ $$W_{sep} = \begin{cases} W_2 & for\ D_{eq} \le 2 \\ \dfrac{W_2 D_{eq}}{2} & for\ D_{eq} > 2 \end{cases}$$ $$W_{out} = \sqrt{\left(\frac{V_{m2}A_2}{\pi d_2 b_2}\right)^2 + W_{\theta 2}^2}$$ $$D_{eq} = \frac{W_1 + W_2 + \Delta W}{2W_2}$$ $$\Delta W = W_{SS} - W_{PS} = \frac{2\pi d_2 U_2 \psi_b}{Z_{eff} L_c}$$ $$Z_{eff} = Z_{MB} + \frac{L_{SB}}{L} Z_{SB}$$

specified (Frigne & Van den Braembussche, 1979; Herbert, 1980). These parameters are usually not known during preliminary design and extend the loss model into the realm of a two-dimensional approach. To maintain a strictly one-dimensional procedure, a more simplistic method based on the relative velocity ratio is used. Equation (2.8),

$$\epsilon_{wake} = 1 - \frac{1}{0.45}\frac{W_2}{W_{max}}, \qquad\qquad (2.8)$$

was published by Takagi, Kobayashi, Miyashiro, and Morimoto (1980) and is based on Schorr, Welliver, and Winslow's (1971) commentary on centrifugal compressor design. While not as robust as the pusedo-2D approach, other researchers have shown that correlating the wake width with the relative velocity ratio is adequate for preliminary design (Bing et al., 2012; Thanapandi & Prasad, 1994).

Of the external losses considered in the present work, recirculation losses have the largest effect on the trend of the impeller efficiency from choke to stall. Recirculation losses increase dramatically with increasing loading and drive the efficiency penalty of operating a centrifugal compressor near stall. Recirculation develops from near-tangential impeller exit flow angles that occur at low mass flow rates, and researchers have often incorporated the impeller exit flow angle as a function of trigonometric or hyperbolic operators to capture the sharp increase in loss as centrifugal compressors approach stall (Aungier, 1995; Coppage et al., 1956; Oh et al., 1997). The impeller diffusion factor is usually included in the correlation for recirculation loss, as shown in the models included in Table 2.11.

Disc friction and seal leakage loss models are the final components of the loss collection available in the general meanline model and are given in Table 2.12 and Table 2.13, respectively. Like recirculation losses, disc friction and seal leakage absorb shaft work without contributing to the impeller pressure rise and are considered external losses. Relative to recirculation, however, the disc friction and seal leakage contribute little to the total loss of the impeller. The disc friction loss is modeled through direct application of the approach given by Daily and Nece (1960) for the induced flow between rotating discs. The seal leakage loss model given by Aungier (1995) uses similar principles to that of the same author's tip clearance loss model.

2.4 Vaneless Diffuser Loss Model

The vaneless diffuser loss model developed by Stanitz (1952) is incorporated into the general meanline model. While recently published two-zone methods provide improved accuracy relative

Table 2.11: Impeller recirculation loss models included in the meanline model.

Reference	Equation
Oh et al. (1997)	$$\Delta h_{0,RC} = D_f^2 U_2^2 \sinh(3.5\alpha_2^3)$$ $$D_f = 1 - \frac{W_2}{W_{1t}} + \frac{K_{D_f}\psi_b}{\frac{W_{1t}}{W_2}\left(\frac{Z}{\pi}\left(1 - \frac{r_{1t}}{r_2}\right) + \frac{2r_{1t}}{r_2}\right)}$$ $$K_{RC} = 8 * 10^{-5}$$ $$K_{D_f} = \begin{cases} 0.6, with\ splitters \\ 0.75, no\ splitters \end{cases}, according\ to\ Galvas\ (1973)$$
Aungier (1995)	$$\Delta h_{0,RC} = \left(\frac{D_{eq}}{2} - 1\right)\left(\frac{W_{\theta 2}}{V_{m2}} - 2\cot\beta_2\right) \geq 0$$ $$D_{eq} = \frac{W_1 + W_2 + \Delta W}{2W_2}$$ $$\Delta W = W_{SS} - W_{PS} = \frac{2\pi d_2 U_2 \psi_b}{Z_{eff}L_c}$$ $$Z_{eff} = Z_{MB} + \frac{L_{SB}}{L}Z_{SB}$$

to Stantiz's model, the current work is intentionally limited to exclusively 1D approaches, so the two-zone, pseudo-2D approaches are not included. Stanitz's method is both extensive and widely available, so only a brief overview is provided in the present work.

Stanitz's (1952) model was developed to be applicable to a wide variety of applications and, therefore, can be used for one-dimensional modeling of radial or mixed flow vaneless diffusers with friction and heat transfer. The method does not consider mixing losses that arise from the impeller exit flow nonuniformities and, therefore, is conducive for use in tandem with an impeller

Table 2.12: Impeller disc friction loss model included in the meanline model.

Reference	Equation
Daily & Nece (1960)	$$\Delta h_{0,DF} = K_{DF} \frac{\bar{\rho} r_2^2 U_2^3}{4 \dot{m}}$$ $$\bar{\rho} = \frac{\rho_1 + \rho_2}{2}$$ $$K_{DF} = \begin{cases} \dfrac{3.7 \left(\frac{s}{r_2}\right)^{0.1}}{Re_{DF}^{0.5}}, & Re_{DF} < 3 * 10^5 \\[2em] \dfrac{0.102 \left(\frac{s}{r_2}\right)^{0.1}}{Re_{DF}^{0.2}}, & Re_{DF} \geq 3 * 10^5 \end{cases}$$ $$Re_{DF} = \frac{U_2 r_2}{\nu_2}$$

mixing loss model. The primary assumptions of Stanitz's model stem from neglecting mixing. The inlet flow is assumed to be uniform in the spanwise and tangential directions such that the flow is a one-dimensional function of radius. Therefore, the average, mixed-out properties of the impeller exit must be provided as inputs to the model.

Once the diffuser inlet flow field is defined from the impeller exit state, the procedure calculates the fluid state as a function of radius, as well as three thermodynamic properties, the fluid velocity, and flow direction. These parameters are calculated from the continuity equation, conservation of momentum in the meridional and tangential directions, equation of state, and the heat transfer equation. The procedure then uses a "marching technique" to step outward in radius through small changes in the radius ratio and calculation of the relevant properties at each step. The original procedure specifies stepping out in radius by up to 10% of the radius ratio at a time until the diffuser exit radius is reached. However, computational resources at the time of publication would have limited the number of iterations realistically possible for the procedure. The computations require little time on a current desktop computer, so in the present work, the procedure was conducted with steps equal to 1% of the vaneless diffuser radius ratio. The procedure given by

Table 2.13: Impeller seal leakage loss model included in the meanline model.

Reference	Equation
Aungier (1995)	$$\Delta h_{0,LK} = \frac{\dot{m}_{CL} U_{CL}}{2\dot{m}} U_2$$ $$U_{CL} = 0.816 \sqrt{\frac{2\Delta P_{CL}}{\rho_2}}$$ $$\Delta P_{CL} = \frac{\dot{m}(r_2 V_{\theta 2} - r_1 V_{\theta 1})}{Z_{eff} \bar{r} \bar{b} L_c}$$ $$Z_{eff} = Z_{MB} + \frac{L_{SB}}{L} Z_{SB}$$ $$\bar{r} = \frac{r_1 + r_2}{2}$$ $$\bar{b} = \frac{b_1 + b_2}{2}$$ $$\dot{m}_{CL} = \rho_2 Z_{eff} \epsilon L U_{CL}$$

Casey (1985) in Section 2.2 was used to determine the skin friction coefficient of the vaneless diffuser.

2.5 Slip Models

The slip models developed by Wiesner (1967), von Backström (2005), and Qiu et al. (2011) are included in the general centrifugal compressor model. The details of each model are given in Section 1.4. Each model is based primarily on the impeller geometry and intended for one-dimensional analysis. While slip is traditionally used to quantify the difference between the exit blade angle and exit flow angle for impellers, OTAC was written to accept an angle for deviation rather than a slip factor. Therefore, to accommodate the existing structure of OTAC, the slip velocity was related to the exit flow angle via equation (2.9),

$$\beta_2 = \text{atan}\left(\frac{V_{m2}}{V_{slip} + \dfrac{V_{m2}}{\tan\beta_{2b}}}\right), \tag{2.9}$$

where β_2 is the impeller exit flow angle, V_{m2} is the impeller exit meridional velocity, V_{slip} is the slip velocity, and β_{2b} is the impeller exit blade angle. The exit flow angle was then used to provide OTAC with a value for deviation.

All of the impeller loss models given by Oh et al. (Oh et al., 1997), as well as Stanitz's vaneless diffuser model (Stanitz, 1952), were incorporated into the meanline model.

2.6   One-Dimensional Model Validation and Results

The efficacy of the general model for centrifugal compressors was validated through comparison of the present model to well-documented historical data. The validation of the present work also serves as verification for the off-design capability of OTAC. Eckardt's impeller A was modeled according to the procedures given by Oh et al. (1997). The loss models recommended by Oh et al. (1997) are given in Table 2.14, and the geometric specifications of Eckardt's impeller A available in the open literature are provided in Section 2.1. Deviation of the flow from the impeller blade exit angle was modeled according to Wiesner's (1967) correlation for slip. Adiabatic operation was assumed throughout the analysis.

Most of the information necessary to replicate Oh et al.'s (1997) procedure is explicitly available in the open literature. However, some parameters necessary to determine the loss through Eckardt's impeller according to each of the models in Table 2.14 is not published. Specifically, values for surface roughness, which are critical to the calculation skin friction loss, as well as the impeller seal and backface geometry are not available. Additionally, Oh et al. do not give a procedure for calculation of the wake width in the Johnston and Dean's (1966) mixing loss model, nor do they provide any information on the tuning of the loss models or coefficients used in their procedure. In the present work, both the impeller and diffuser surfaces were assigned an average surface roughness of 128 microinches. The gap between the impeller backface and the stationary

Table 2.14: Oh et al. (1997) loss collection.

Loss Mechanism	Model
Incidence	Conrad et al. (1979)
Blade Loading	Coppage et al. (1956)
Skin Friction	Jansen (1967)
Clearance	Jansen (1967)
Mixing	Johnston & Dean (1966)
Disc Friction	Daily & Nece (1960)
Recirculation	Oh et al. (1997)
Leakage	Aungier (1995)
Vaneless Diffuser	Stanitz (1952)

casing was set as 0.25 inches, and the seal gap required for calculation of the leakage loss was assigned a value of 0.05 inches. The wake width was calculated according to equation (2.8). After initial evaluation of the resulting performance predictions, the loss models were tuned to match the results published by Oh et al. (1997).

The total temperature rise ratio predicted via the Oh et al. modeling procedure generally underpredicts the work input provided by the impeller to the flow, Figure 2.3. The total temperature rise predicted by Oh et al. is not included in the figure because it was explicitly given in the original work. The effect of the recirculation loss model on work input can be observed in the sharp upturn in work input at the lowest mass flow rates of each speedline. The under prediction in work input is primarily driven by the use of Wiesner's slip model, as illustrated in Figure 2.4. The experimental slip factor, as calculated from optical measurement techniques, is much larger than the slip factor predicted by Wiesner's slip model throughout the operating range, which corresponds to an underprediction of the work input provided by the impeller.

The fairly large difference in slip factor results in a relatively small difference in total temperature rise because the external losses have been tuned to match the experimental data. Generally, the
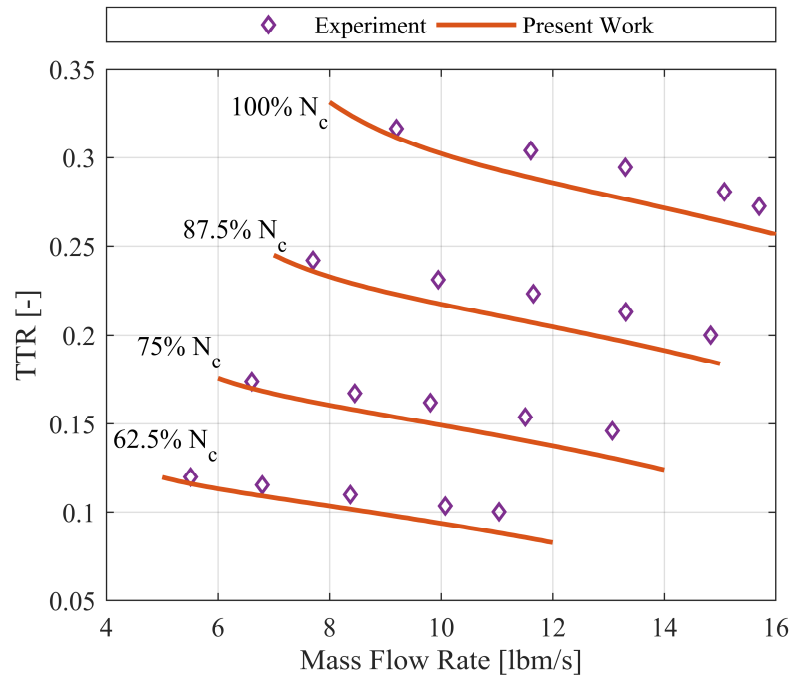
Figure 2.3: Comparison of experimentally measured and predicted total temperature rise ratio for Eckardt's impeller A.
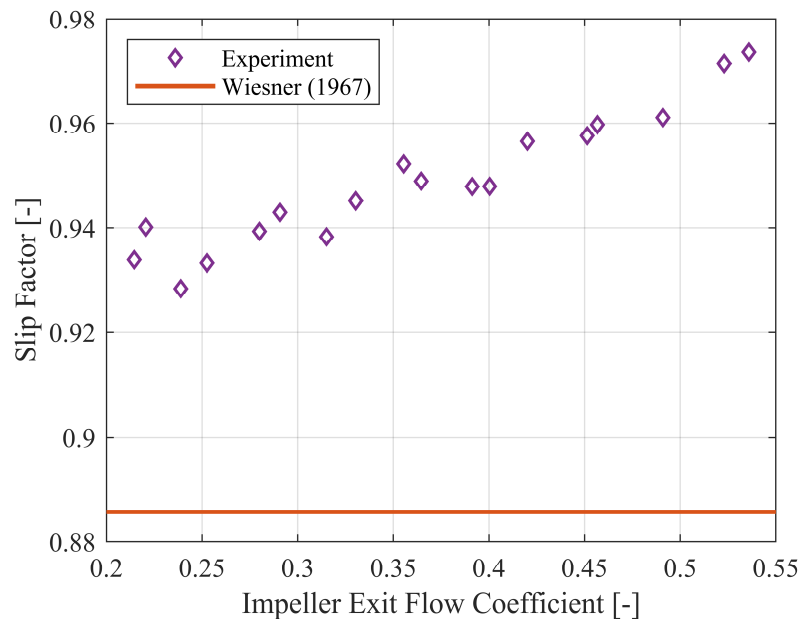
Figure 2.4: Comparison of measured and predicted slip factor for Eckardt's impeller A.

work done on the flow and the efficiency of the compression process determine the total pressure ratio of the stage. However, external losses partially decouple the stage work input from the total pressure ratio because external losses contribute to the enthalpy rise of the flow without a corresponding pressure increase. In other words, external losses are work done on the flow by some mechanism not associated with flow turning from the impeller blades. The relationships between slip factor, external losses, and work input will be explored further in the proceeding chapters.

Figures 2.5-2.8 show the comparison of the efficiencies predicted by the experiments, Oh et al.'s model, and the model of the present work for four speedlines. The contribution of each loss model in the present work to the overall loss for each speedline is also provided by showing the portion of the loading coefficient required to overcome the loss in the impeller. A dash-dot black line indicates the isentropic work input required to reach the pressure rise for a given corrected speed and mass flow rate. The Euler work, the work done by the blades from flow turning, is indicated by a solid black line. Finally, the dashed black line is the total work done on the flow by the stage, including the blades and external losses together. The internal losses are shown with solid colors, and external losses have a wavy hatch pattern overlaid on the color.

Skin friction loss comprises the majority of the loss at all four speedlines and increases with increasing mass flow rate. Blade loading and incidence losses increase with decreasing mass flow rate, while tip clearance losses remain fairly constant across the operating range. The mixing loss increases with decreasing mass flow rate at each speedline, but the contribution to the overall loss is negligible because the wake width calculated from equation (2.8) is very small for Eckardt's impeller at all operating conditions. Internal losses contribute most of the overall loss at high mass flow rates, but as recirculation increases at low mass flow rates the external losses become more significant.

The efficiency of the models matches the efficiency measured in the experiments fairly well at the 100%, 87.5%, and 75% speedlines, but the models do not capture the rapid decrease in efficiency at high mass flow rates for 100% and 87.5% speed. The inducer is likely approaching the choking mass flow rate, and the loss models are unable to capture the rapid increase in loss associated with
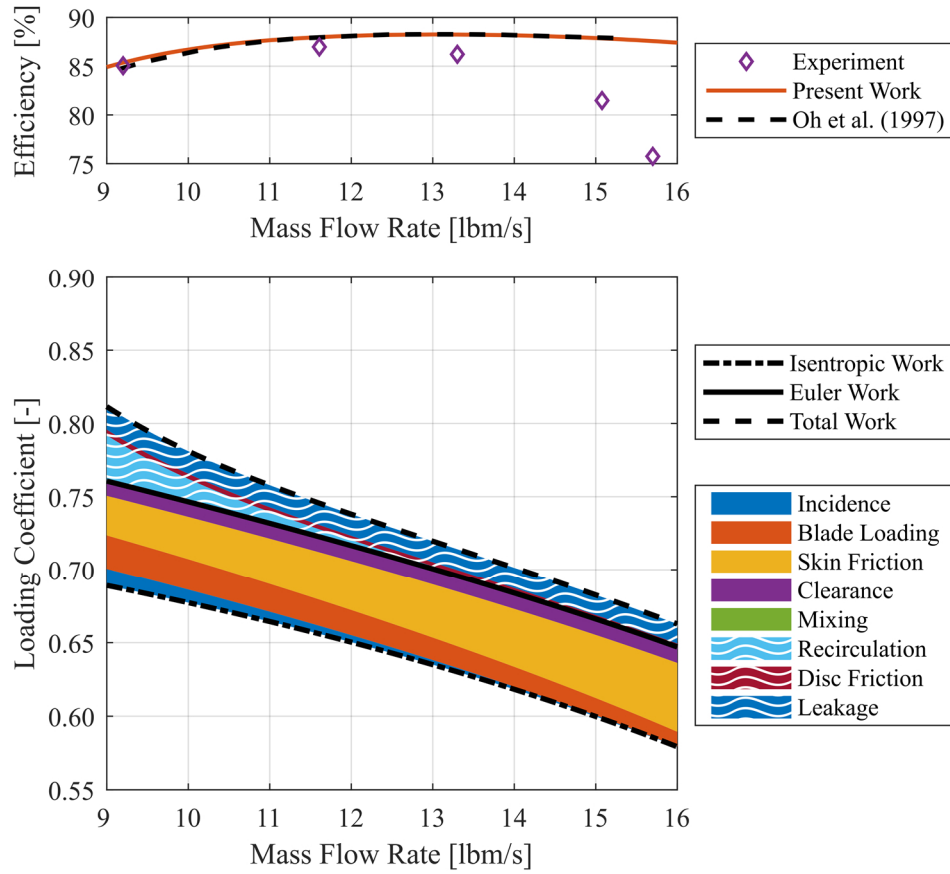
Figure 2.5: Comparison of efficiency between the experiment, Oh et al.'s model, and the present work, as well as the loss breakdown of the present work, for Eckardt's impeller A at 100% corrected speed.

inducer choke. At 62.5% speed the trend in the efficiency is captured by the models, but the magnitude of the efficiency is underestimated. The rapid increase in recirculation loss at low mass flow rates drives the steep reduction in efficiency observed at low mass flow rates for all of the speed lines. The one-dimensional modeling published by Oh et al. and that of the present work are quite similar at all speeds, which provides validation for the present centrifugal compressor model.

The experimentally measured compressor performance map in Figure 2.9 is accompanied by the maps predicted with each of the one-dimensional models. The measured and modeled compressor maps agree fairly well, though the models generally underpredict the total pressure ratio relative to the experiment. For a reduced work input with the same efficiency, less total pressure rise is provided. Therefore, the underprediction in total pressure ratio relative to the experiment originates
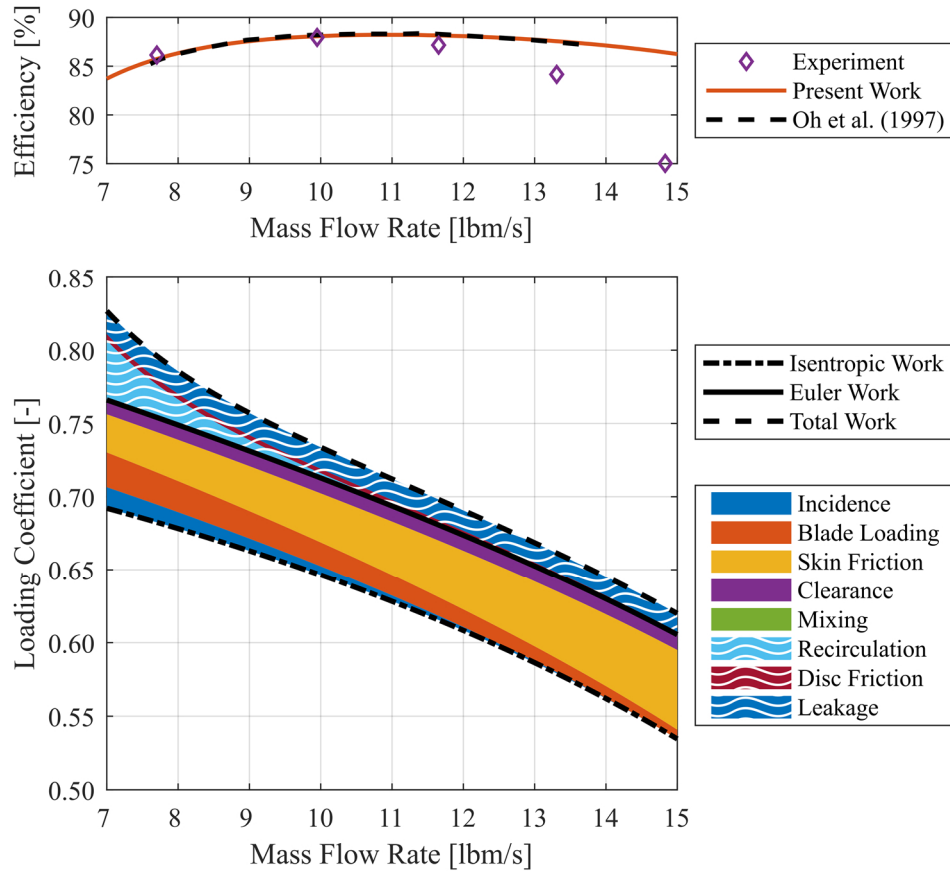
Figure 2.6: Comparison of efficiency between the experiment, Oh et al.'s model, and the present work, as well as the loss breakdown of the present work, for Eckardt's impeller A at 87.5% corrected speed.

from the underprediction in work input shown in Figure 2.3 combined with the generally similar levels efficiency at the same operating condition. In terms of the comparison between Oh et al.'s model and the present work, the predicted total pressure ratio is almost identical and, with the replication of efficiency, validates the model in the present work as well as the capability of OTAC to conduct off-design calculations for centrifugal compressors.
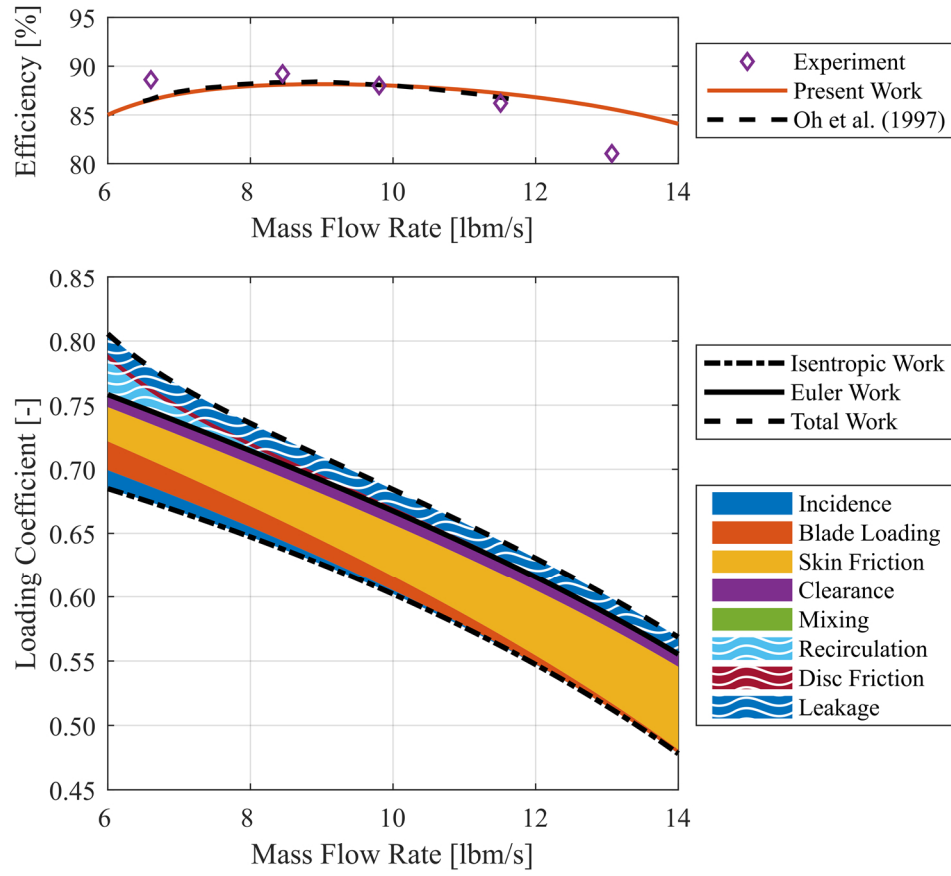
Figure 2.7: Comparison of efficiency between the experiment, Oh et al.'s model, and the present work, as well as the loss breakdown of the present work, for Eckardt's impeller A at 75% corrected speed.
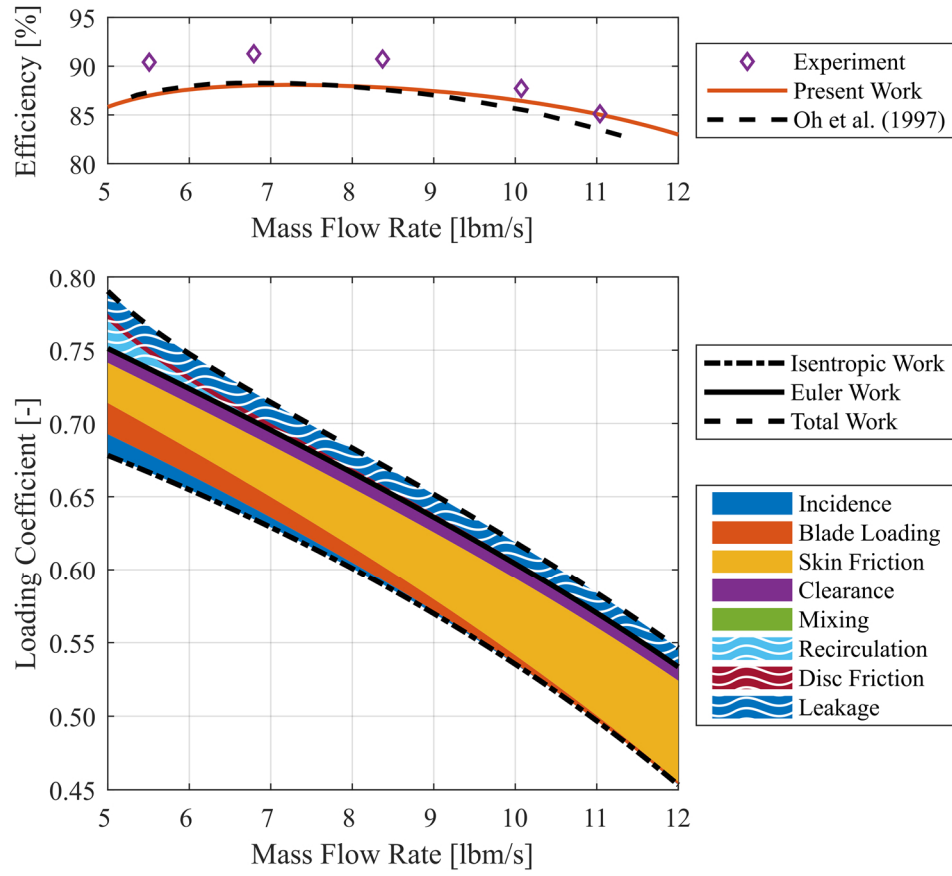
Figure 2.8: Comparison of efficiency between the experiment, Oh et al.'s model, and the present work, as well as the loss breakdown of the present work, for Eckardt's impeller A at 62.5% corrected speed.
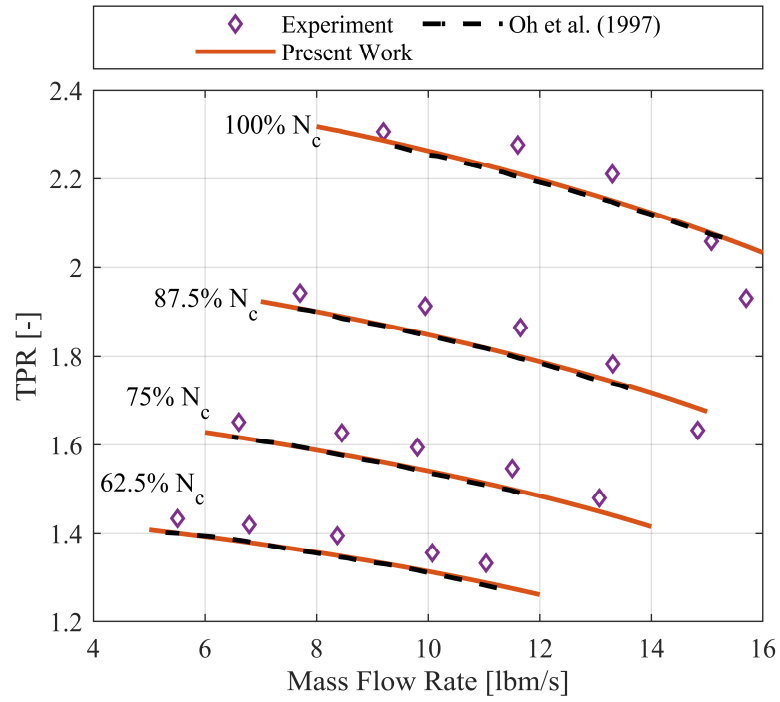
Figure 2.9: Comparison of experimentally measured and predicted compressor map for Eckardt's impeller A.

3. EFFICACY OF RELATIVE EDDY SLIP MODELS

The work input provided by an impeller must be accurately predicted with one-dimensional analysis tools to facilitate a successful preliminary design phase. The accuracy of the predicted work input is contingent on the accuracy of the slip model used in the one-dimensional model, and in high tip speed compressors, the work input is especially sensitive to errors in predicted slip factor. Models in the open literature have largely emphasized pumps and low-speed compressors that are not representative of the high tip speeds in modern aerospace compressors. This chapter addresses the efficacy of existing open literature slip models for predicting slip in preliminary design and extends the discussion of slip models themselves to their effects on work input. Furthermore, the utilization of slip models to predict the work input of high-speed compressors at design and off-design is considered.

The simplicity, ease of use in the preliminary design phase, and long history of satisfactory results have set Wiesner's approach as the standard to which all other models are compared (Del Greco et al., 2009; Paeng & Chung, 2001; Qiu et al., 2011; Stuart et al., 2019; von Backström, 2005). To evaluate the capacity for existing slip models to predict the work input for high-speed centrifugal impellers, the efficacy of Wiesner's model will be primarily investigated. The SRE approach developed by von Backström will be considered for its markedly good approximation of the Busemann solution. Qiu's model will also be included in the discussion since it is notable for the expressed intent to achieve accurate prediction of slip factor at both design and off-design conditions. All three of the models are similar, however, in that they are based on the relative eddy theory originally proposed by Stodola and Busemann (Busemann, 1928; Stodola, 1927). The equations and full definition of terms for Wiesner's, von Backström's and Qiu's models are provided in Chapter 1.

The general meanline model developed in OTAC was used to apply each of the three slip models to the five centrifugal compressors documented in detail in Chapter 2: Krain's transonic impeller stage (SRV2-O), the NASA low specific speed impeller (CC3), Came's transonic backswept impeller (Came stage B), Eckardt's backswept impeller (Eckardt impeller A), and the Honeywell

high-speed impeller (SSCC). Adiabatic operation was assumed throughout the analyses, and the vaneless diffuser configuration was used for each of the open literature cases. The Honeywell SSCC is equipped with a vaned diffuser, and rather than modeling the vaned diffuser, the impeller efficiency and impeller total pressure ratio were used for the development of and comparison to the one-dimensional model. The array of speeds included in the analysis of each compressor is given in Table 3.1.

Table 3.1: Corrected speeds available for and included in the analysis for each compressor.

Compressor	40.0%	50.0%	60.0%	62.5%	70.0%	75.0%	80.0%	85.0%	87.5%	88.0%	90.0%	92.5%	95.0%	97.5%	100.0%
Krain SRV2-O			X		X		X			X			X		X
NASA CC3			X		X	X					X				X
Came B		X		X		X					X		X		X
Eckardt A				X	X		X		X						X
Honeywell SSCC	X	X	X		X		X	X			X	X	X	X	X

Loss models require tuning to provide representative total pressure ratios of the experiments and, despite tuning, may accurately predict impeller performance at some operating conditions but give poor estimates of performance at others. Since the primary objective of the present work is to investigate the efficacy of slip models for the prediction of work input, the impeller loss models were removed. Instead, the flexibility of OTAC was utilized to prescribe the experimentally measured stage efficiency to each operating point, and the measured stage loss was divided between the vaneless diffuser (calculated through Stanitz's model) and the impeller for each open literature stage.

The documentation of each stage in the open literature does not allow for rigorous partitioning of the impeller loss into internal and external sources. Based on a sensitivity study of each stage to the internal/external loss distribution presented in Section 3.2, 80% of the impeller loss was

allocated to internal loss mechanisms and the remaining 20% to external loss sources at each operating point. Experimentally calculated values of total pressure ratio and efficiency were available for the SSCC impeller, so the model was constructed using the same experimental matching procedure and loss distributions excluding the vaneless diffuser loss. The performance of each stage was evaluated with each of the slip factor correlations developed by Wiesner (Wiesner, 1967), von Backström (von Backström, 2005), and Qiu (Qiu et al., 2011).

An experimentally measured slip factor was not available in the open literature for the SRV2-O, CC3, or Came stage B impellers, but a value for slip factor can be calculated from published total pressure ratio and efficiency data per the procedure in Figure 3.1. The geometry of each stage, as well as the total pressure ratio, mass flow rate, and corrected speed at each operating point, are given in the original publications. These parameters serve as inputs to the meanline equations in conjunction with an initial estimate of the loss incurred during the compression process. The meanline equations are solved with the provided inputs, and the resulting total temperature rise ratio calculated in the model is compared to that of the experiment (the experimental total temperature rise ratio is calculated from published total pressure ratio and efficiency data). The value for loss is then iterated on until the modeled and experimental total temperature rise ratios converge. Once convergence is achieved, the value for slip factor necessary to provide the work input for the given geometry and operating conditions is extracted from the one-dimensional model. During the procedure, the internal and external losses for each operating point were distributed in the same manner as prescribed for implementation of the slip models.

For validation of the method shown in Figure 3.1, the calculated values of slip factor were compared to the experimentally measured values of slip factor available for Eckardt's impeller. The calculated slip factor replicated the trend in measured values of slip factor reported by Eckardt (1980) with a general offset of 0.01 to 0.02 in slip factor between the experiment and the meanline matching procedure, Figure 3.2. For reference, an absolute error of ±0.05 in slip factor has historically been considered acceptable for the evaluation of slip models (a relative error of ±5% has also been used). The values of slip factor resulting from the procedure are given as a function of the impeller exit flow coefficient for all five impellers in Figure 3.3.
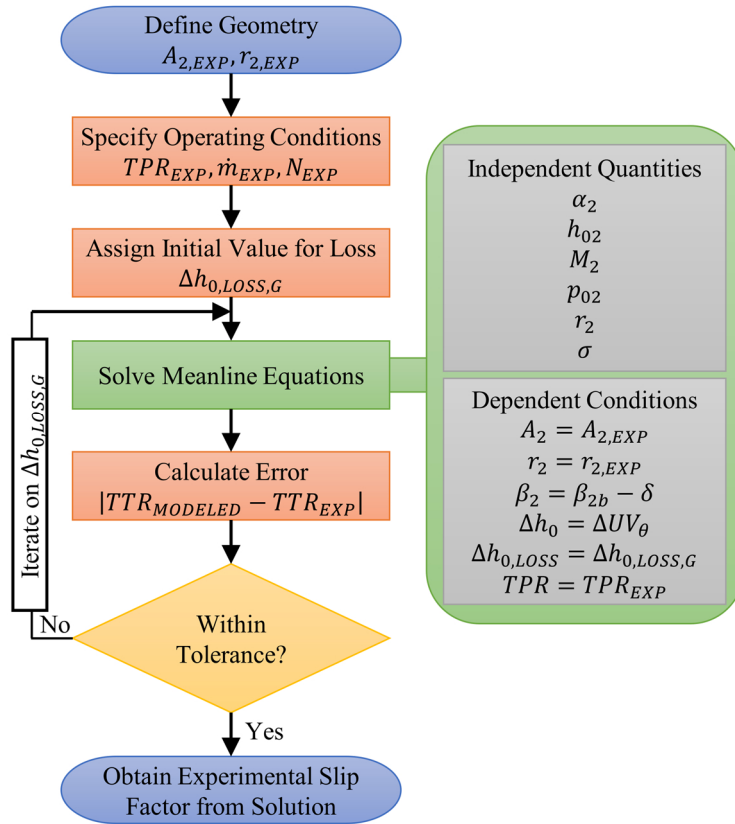
Figure 3.1: Procedure to calculate experimental slip factor from overall performance data.
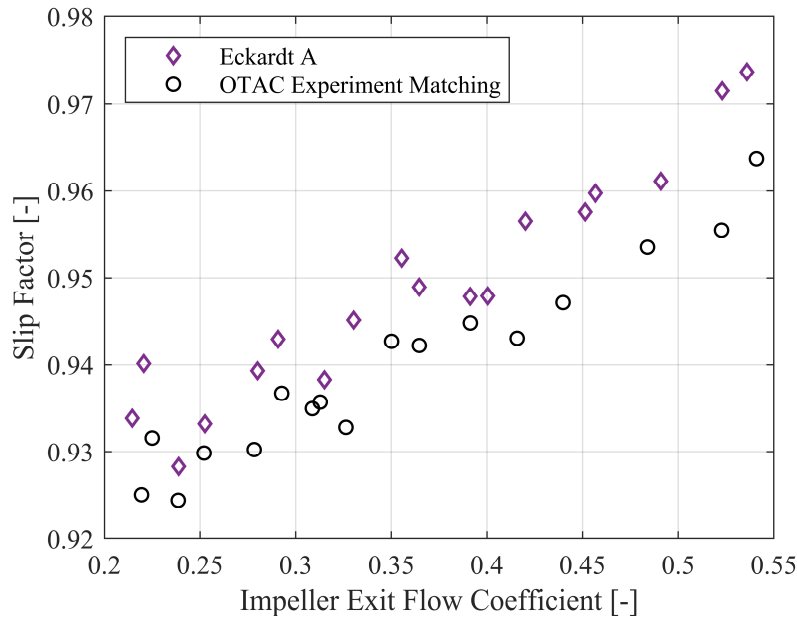
Figure 3.2: Comparison between experimentally measured slip factor and slip factor calculated through experimental matching of the one-dimensional model for Eckardt's impeller A.
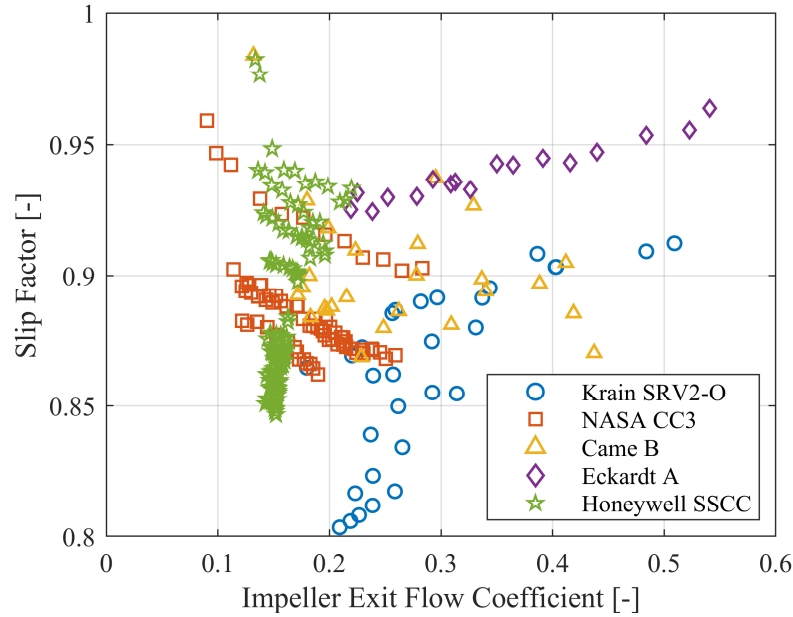
Figure 3.3: Experimental values of slip factor resulting from the procedure outlined in Figure 3.1.

Since the vaneless diffuser configurations of the open literature stages are under investigation, choke occurred in the inducer of the impeller. To avoid any confounding effects from inducer choke, all points showing performance decrements due to choke in the open literature compressors were neglected in the proceeding analysis.

Minimal documentation is available on the validation of blockage models in the open literature (Aungier, 1995; Pampreen, 1981), and some researchers have postulated that modeling blockage is fundamentally inconsistent with the meanline approach (Japikse, 1996). Therefore, blockage was not considered unless explicitly stated otherwise.

3.1   Sensitivity to Heat Transfer

Differences between the predicted and measured total temperature rise ratio occur due to differences between the actual and predicted impeller exit velocity triangle for the case of axial inlet flow (no prewhirl) and adiabatic operation. Since the inlet conditions are provided in the open literature and matched in each of the models, the inlet flow is not a factor in the misprediction of total temperature rise ratio. Heat transfer, however, may contribute to the differences between the

75

model and experiment since the meanline analysis was conducted with the assumption of adiabatic operation.

To explore the validity of the adiabatic assumption in the meanline model, the sensitivity of the modeled work input to heat transfer was assessed. Utilizing the Wiesner slip model, the total temperature rise ratio at the peak efficiency point at design speed of each stage was calculated for varying levels of heat transfer to determine the amount of heat transfer necessary to reach agreement with the experimentally measured total temperature rise ratio. The diabatic, modeled total temperature rise ratio normalized by the measured peak efficiency total temperature rise ratio for each high-speed stage is given as a function of the percentage of work input lost due to heat transfer, Figure 3.4. The adiabatic condition is indicated by a magenta line overlaid on the ordinate. The difference between the total temperature rise ratio in the experiment and the adiabatic model at design speed is quite large for the Krain and SSCC impellers, and there are also significant differences between the experiment and modeled adiabatic conditions at peak efficiency for CC3 and Came stage B. As the heat transfer out of the flow increases in magnitude, the modeled total temperature rise ratio approaches that of the experiment such that approximately 11%, 7%, 4%, and 9% of the work input delivered by the impeller must be lost to heat transfer to match the experimental total temperature rise ratio for the SRV2-O, CC3, Came B, and SSCC stages, respectively. Since heat transfer out of the flow for a compressor operating at steady state is known to be small relative to the work input provided by the stage (Denton, 1993), the contribution of heat transfer to the large difference between the experiment and the adiabatic model is likely negligible for all four high-speed cases. Therefore, the majority of the difference between the model and experiment must be due to the difference between the predicted and actual slip factor, and the Euler turbomachinery equation with axial inflow can be written without heat transfer:

$$-w = \Delta h_0 = c_p \Delta T_0 = U_2 V_{\theta 2} = U_2\left(V_{\theta 2,PFG} - V_{slip}\right). \qquad (3.1)$$

In equation (3.1), w is work input, h_0 is stagnation enthalpy, c_p is the specific heat at constant pressure, T_0 is stagnation temperature, U_2 is the impeller exit tip speed, $V_{\theta 2}$ is the impeller exit tangential velocity, $V_{\theta 2,PFG}$ is the impeller exit tangential velocity at the perfect flow guidance condition, and V_{slip} is the slip velocity.
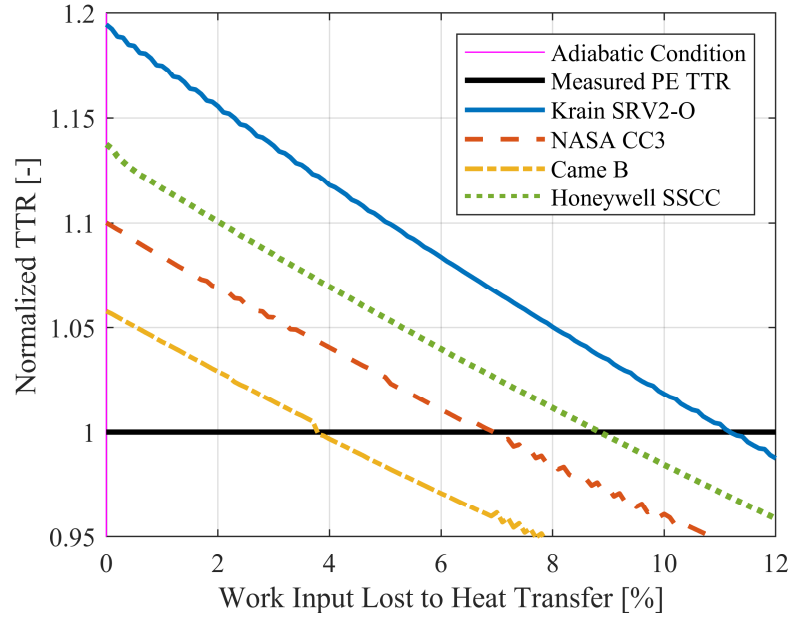
Figure 3.4: Sensitivity of the peak efficiency TTR for each stage to heat transfer as predicted by the Wiesner slip model.

3.2 Considerations for Internal/External Loss Distribution

An ambiguity in the prediction of slip factor arises from the distribution of internal and external losses. As was discussed in detail in the previous chapters, external losses consume shaft work but do not contribute to the total pressure rise. More specifically, external losses arise from flow mechanisms not associated with turning of the flow by the impeller but still increase the exit stagnation enthalpy of the stage. The shaft work absorbed by the blades and external losses usually cannot be rigorously separated in experiments, though external losses models may be used in conjunction with experimental measurements to estimate the contribution of external losses to the overall loss between measurement stations (Daily & Nece, 1960; Harley et al., 2014; Qiu et al., 2008; Wiesner, 1967). In the case of the present meanline model, the external losses are prescribed, so precise allocation of the work absorbed by the flow from the blades vs. external losses is possible. To obtain the work done on the flow by the blades, the penalty of the external losses, given by the subscript EXT, must be deducted from the overall stagnation or temperature rise, given by the subscript $STAGE$:

$$-w_b = \Delta h_{0,STAGE} - \Delta h_{0,EXT} = c_p \Delta T_{0,STAGE} - c_p \Delta T_{0,EXT} = U_2 V_{\theta 2}, \qquad (3.2)$$

which is defined specifically for the work input to the flow from the blades, w_b. From equation (3.2), as the external losses increase, the impeller is responsible for less of the temperature rise experienced by the stage. Since the PFG condition for the impeller is independent of losses, the slip factor must decrease to balance the shaft work consumed by the external losses. The relationship between slip factor and internal/external loss allocation is given in Figure 3.5. The experimental slip factor for the peak efficiency point of each stage is given as a function of the percentage of overall loss allocated to external loss, and the vertical, magenta line indicates the external loss allocation used throughout the present work. As was inferred from equation (3.2), the slip factor decreases as the external losses consume greater amounts of the shaft work at a given efficiency.
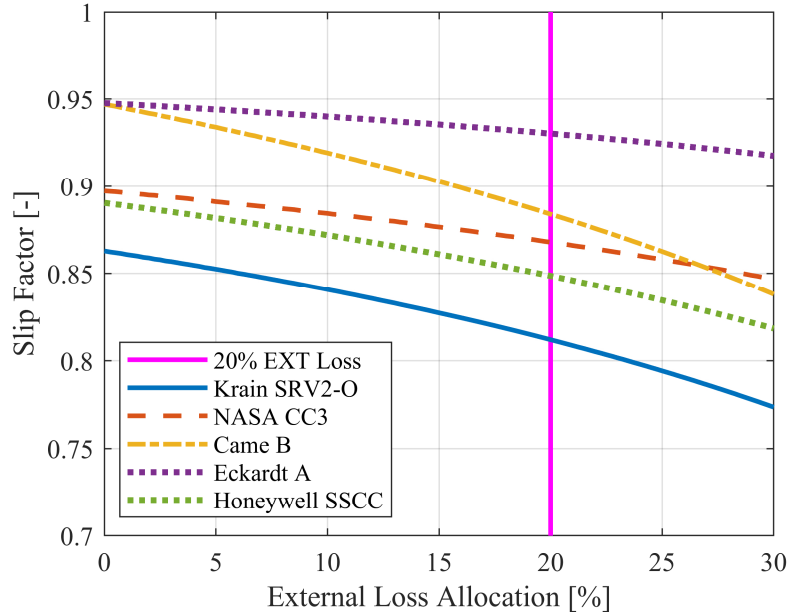
Figure 3.5: Sensitivity of the slip factor for each impeller at the peak efficiency point to the percentage of total loss generated by external sources.

External losses are known to vary with operating condition and speed, but they are non-negligible throughout the operating range and can be quite large near stall (Aungier & Cassin, 2003; Harley et al., 2014; Oh et al., 1997). Since the exact distribution of internal and external losses for the

stages under investigation is not available from the open literature, 20% of the loss at all operating points was delegated to external sources. Based on Figure 3.5, an error of up to 10% in the estimation of external losses gives an estimate of slip factor within the ±0.05 error band for slip factor for Came's impeller, the most sensitive to external losses. Thus, allocation of 20% of the total losses to external sources at all operating points was deemed an acceptable estimate since detailed enumerations of the loss sources were not available.

Since the primary focus of this work is on slip factor and work input by the impeller, all quantities will be in reference to work input to the flow by the blades for the remainder of the present work: external losses will not be included unless explicitly stated otherwise. As examples, ψ and Δh_0 will refer specifically to the loading coefficient and change in total enthalpy, respectively, generated by the blades without the temperature rise due to external losses.

3.3   Discussion of Experimental and Modeled Slip Factor

The differences between the experimental slip factor and those predicted by Wiesner's slip model, von Backström's model, and Qiu's model are shown in Figure 3.6a, Figure 3.6b, and Figure 3.6c, respectively. The bar graphs in Figure 3.6 show the distribution of the error data color coded by stage, and a black, vertical, dotted line highlights the zero-error location. Overpredictions manifest as negative values to the left of the zero-error line, while underpredictions are positive and to the right. The stars above the bar graphs are the error in slip factor at the peak efficiency operating point of the 100% speedline of each impeller. The ordinate is normalized such that the stages are equally represented within the bar graphs to prevent a single stage with many data points from distorting interpretation of the data. The range of actual values of slip factor computed for the experiments and each of the models are given in Table 3.2.

From the bar graphs, approximately 50% of the data fall within the traditionally accepted ±0.05 error band for all three slip models. However, more than 25% of the data are to the left of the ±0.05 band for Wiesner's and von Backström's models, and approximately 50% of the data are to the left of the error band for Qiu's model. All data to the left of the error band are associated with high-speed stages indicating the slip models generally overpredict the slip factor for high-speed
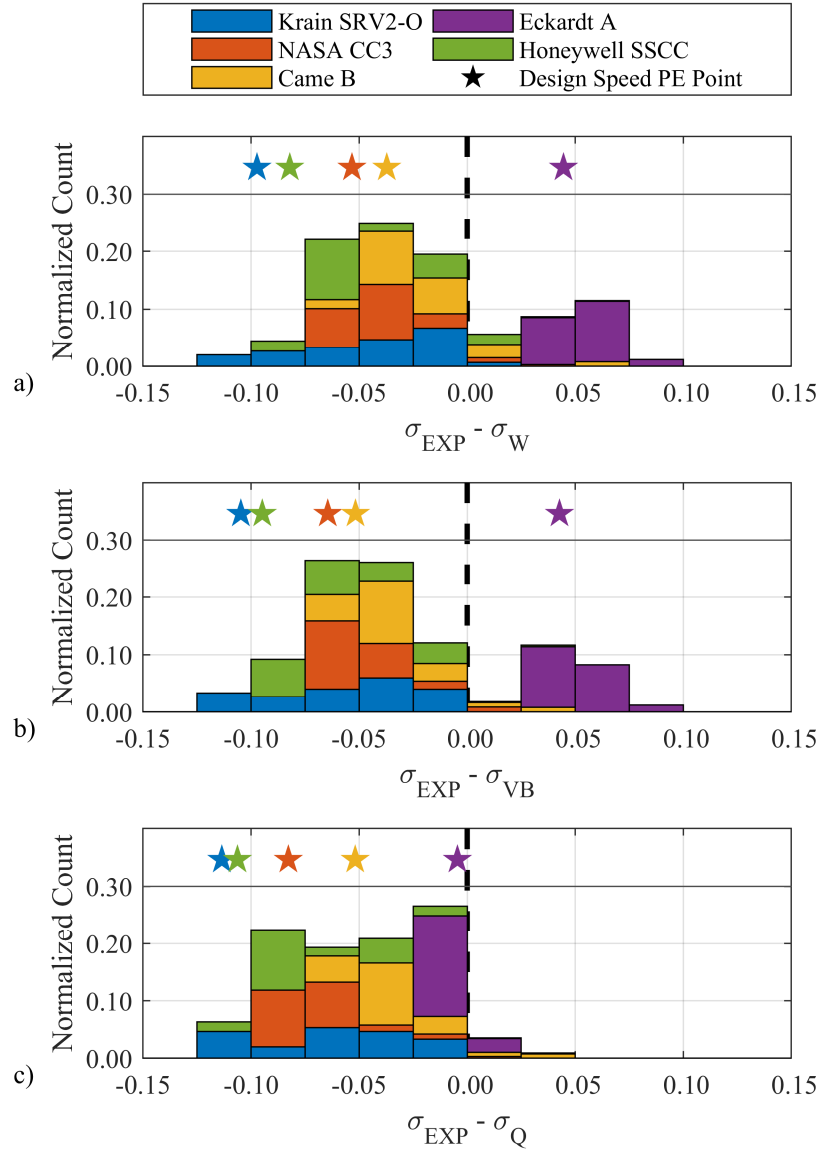
Figure 3.6: Difference between calculated experimental values of slip factor and the predicted values of slip factor for the a) Wiesner slip model, b) von Backström slip model, and c) Qiu slip model for the published operating points of each compressor.

impellers. Additionally, all three models exhibit a similar trend and distribution in the error between the models and experiments for the high-speed stages. The SRV2-O and SSCC impellers experience the broadest range and largest overpredictions in the implementations of each model with significant overpredictions occurring at the design point. The values of slip factor for CC3 and Came's impeller are also generally overpredicted both at the design point and throughout the operating range, although to a lesser degree. It is likely that similar trends and distributions are

Table 3.2: Range of slip factors observed for each compressor in the experimental matching and as predicted by the three slip models.

Compressor	σ_{EXP}	σ_W	σ_{VB}	σ_Q
Krain SRV2-O	0.80 – 0.91	0.91	0.92	0.93
NASA CC3	0.86 – 0.96	0.93	0.94	0.95 – 0.96
Came Stage B	0.87 – 0.98	0.92	0.94	0.94
Eckardt Impeller A	0.92 – 0.96	0.89	0.89	0.93 – 0.97
Honeywell SSCC	0.85-0.98	0.93	0.94	0.95

observed in Figure 3.6 for all three slip models because each model is based on the theory of the relative eddy in the impeller. In the validation of their models, Wiesner and von Backström explicitly compare their models to Busemann's analytical solution for the relative eddy in logarithmic spiral blades, and Qiu's model is based on Stodola's original modeling of the relative eddy. Since all three models are founded on the same concept, they all exhibit similar trends in error when applied to high-speed impellers. Therefore, the relative eddy concept may not capture some aspects of high-speed impellers, such as the large range of possible impeller tip speeds, which may have a significant effect on slip.

Moreover, the models are not able to capture the large variation in slip experienced across the operating range for the high-speed stages. From Table 3.2, the range of slip factor for each high-speed stage is more than 0.1, the width of the traditionally accepted error band, and only Qiu's model varies with operating condition. Qiu's model accurately reflects both the range and absolute value of slip factor for Eckardt's impeller, but it does not represent the broad range of slip factors encountered in the high-speed stages. Interrogation of the model shows that Eckardt's impeller is more sensitive to the blade turning rate term, equation (1.22), than the other stages. The blade turning rate is near zero for Krain's and Came's impellers, which makes the slip due to blade turning very small. In the case of CC3 and SSCC impellers where the blade turning is large enough to support some variation of slip factor with operating condition, the backsweep is larger than for Eckardt's impeller so the scale of the variation is diminished (section 2.1 compares the impeller geometries). Additionally, the impeller exit flow coefficient, which drives the variation of slip

factor with operating conditions, usually shows limited variation across an impeller's operating range. Because of the geometrical differences between Eckardt's impeller and the high-speed stages, the variation of slip factor predicted by Qiu's model for the high-speed stages is small relative to the range of actual slip factors.

To evaluate the variation of slip factor with operating condition, the Euler equation is rearranged to provide a non-dimensional measure of work input in terms of slip factor and key design parameters. Dividing both the stagnation enthalpy rise and total temperature rise portions of the Euler equation by the square of the impeller tip speed and inlet total temperature and casting the specific heat in terms of the gas constant and ratio of specific heats gives equation (3.3),

$$TTR = \frac{\Delta T_0}{T_{01}} = (\gamma - 1)\psi M_{U2}^2, \tag{3.3}$$

which defines the normalized total temperature rise ratio in terms of loading coefficient, ψ, machine Mach number, M_{U2}, and the ratio of specific heats, γ. The machine Mach number is

$$M_{U2} = \frac{U_2}{\sqrt{\gamma R T_{01}}} \tag{3.4}$$

and the loading coefficient can be defined as

$$\psi = \frac{V_{\theta 2}}{U_2} \tag{3.5}$$

for the case with no pre-whirl. From the impeller exit velocity triangle in Figure 1.6, the exit tangential velocity is

$$V_{\theta 2} = U_2 - V_{slip} - V_{m2} \tan \beta_{2b} \tag{3.6}$$

where V_{m2} and β_{2b} are the impeller exit meridional velocity and impeller exit blade angle, respectively. Combining equation (3.6) with the definition of machine Mach number in equation (2.4) and the definition of slip factor in equation (1.13) gives the loading coefficient in terms of slip factor, backsweep, and impeller exit flow coefficient, ϕ_2:

$$\psi = \sigma - \phi_2 \tan \beta_{2b}. \tag{3.7}$$

The impeller exit flow coefficient is the ratio of the impeller exit meridional velocity to the impeller exit tip speed:

$$\phi_2 = \frac{V_{m2}}{U_2}. \tag{3.8}$$

The form of loading coefficient in equation (3.7) is substituted into equation (3.3) to recast the normalized total temperature rise ratio as a function of the nondimensional impeller tip speed and exit velocity triangle:

$$TTR = (\gamma - 1)(\sigma - \phi_2 \tan \beta_{2b})M_{U2}^2. \tag{3.9}$$

While there have been many proposals that the slip factor might vary with mass flow rate and impeller exit flow coefficient, a reliable relationship between the slip factor and flow conditions has not yet been established in the open literature. For example, as shown in Figure 3.3, there is not a clear relationship between slip factor and impeller exit flow coefficient for the four impellers under examination. However, the relationships between the design parameters and slip in equations (3.7) and (3.9) support analyzing the slip factor in terms of loading coefficient and machine Mach number, Figure 3.7. The points on the scatter plot are the experimental data for each of the centrifugal compressor stages colored by the value of slip factor. Consistent trends in the value of slip factor can be discerned across different impeller designs as well as trends unique to each impeller. The dominant feature is the decrease in slip factor with increasing machine Mach number such that the smallest values of slip factor occur at the highest wheel speeds, both overall and for each design. Figure 3.6 showed that the slip models generally overpredict the slip factor

for the high-speed compressors, and thus, Figure 3.7 shows that the largest overpredictions in slip factor occur at the largest reported wheel speeds (i.e., at or near the design speed) for the high-speed stages.

To understand the dependence of slip factor on machine Mach number, equation (3.9) is rearranged to give the slip factor in terms for the total temperature rise ratio, machine Mach number, and exit flow coefficient:

$$\sigma = \frac{TTR}{(\gamma - 1)M_{U2}^2} + \phi_2 \tan \beta_{2b}. \tag{3.10}$$

Together, equation (3.10) and Figure 3.7 provide insight into the large ranges of slip factor documented in Table 3.2 for the high-speed compressors. While the datasets of all the stages extend from the design speed to minimums near 60% corrected speed (Table 3.1), the change in machine Mach number is much larger for the high-speed stages than for Eckardt's impeller across the same change in percent corrected speed: the range of machine Mach numbers observed in Figure 3.7 for Eckardt's impeller is less than 0.4. The small change in impeller tip speed results in a variation of slip factor 0.04. In contrast, the smallest range of machine Mach number for the high-speed compressors is almost 0.6 for CC3, and largest span of machine Mach number is more than 1.0 for the SSCC impeller. In addition to the large variations of machine Mach number across their operating ranges, the high-speed stages also run at large machine Mach numbers. Because the machine Mach number is raised to a power of two in equation (3.10), the slip factor is also more sensitive to changes in the machine Mach number at higher impeller wheel speeds. Thus, the high-speed stages experience large changes in slip factor across their operating range as a result of correspondingly large ranges of machine Mach number at high impeller tip speeds.

The relationship between slip factor and loading coefficient is more complex. As a broad observation of Figure 3.7, the slip factor generally increases with increasing loading coefficient across the design space. Considering constant machine Mach numbers of approximately 0.85 or 1.7, the slip factor increases (the color of the points lightens) with increasing loading coefficient in a pervasive trend across at least three impeller designs at each speed. However, this trend does
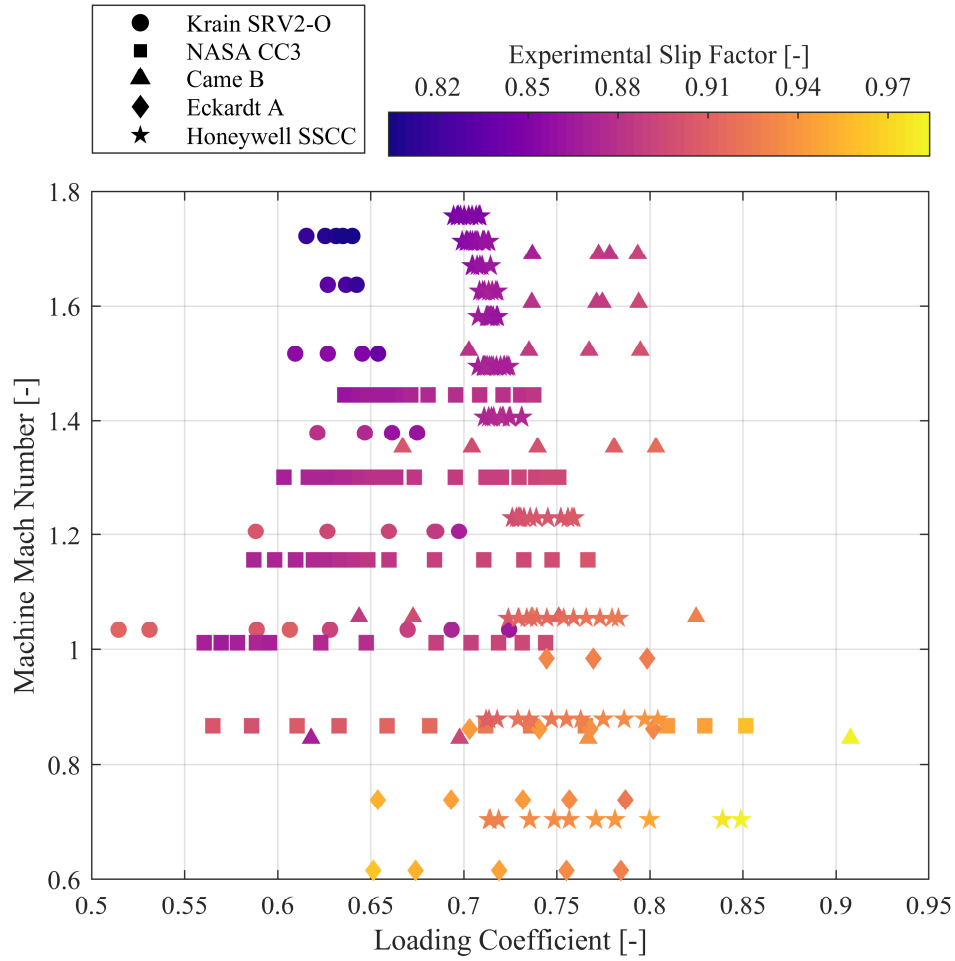
Figure 3.7: Trend of slip factor with operating conditions as a function of the dimensionless design parameters of loading coefficient and machine Mach number.

not hold within each impeller. Relative to points in each impeller's individual operating range, the slip factor increases with loading coefficient for the CC3 and Came stage B but decreases with loading coefficient for the SRV2-O. The trend of slip factor with loading coefficient is ambiguous at high speeds for the Honeywell SSCC due to the small range of available loading coefficients, but at low speeds where the range of loading coefficient is larger, the slip factor increases with increasing loading coefficient. The slip factor decreases with loading coefficient at very low speeds for Eckardt impeller A. At machine Mach numbers above 0.8, the slip factor reverses the trend and increases with loading, but the few non-choke data points at the higher speeds for Eckardt's impeller make drawing conclusions difficult. Examining the relationship between slip factor, loading coefficient, and backsweep in equation (3.7) provides some insight into the contradictory

trends between designs. The loading coefficient sets the minimum value for slip factor through equation (3.7). Thus, for a loading coefficient of one, the minimum possible value for slip factor is exactly one. As the loading coefficient decreases from one, there is more margin for slip to develop because the minimum possible value for slip factor also decreases. Figure 3.8 illustrates the relationship in equation (3.7) through lines of constant slip factor relative to the loading coefficient and backsweep parameter. The range of values of loading coefficient and backsweep parameter for each impeller are overlaid in colored regions, and the compressors with lower loading generally experience lower slip factors. Therefore, the broad trend of decreasing slip factor with decreasing loading coefficient is observed in Figure 3.7 across large differences in loading, such as the wide operating range for CC3 or the combined range of the Krain, SSCC, and Came impellers. It is postulated that the reverse trend may be true within specific designs because the loading coefficient only sets a minimum value for slip factor, and across smaller changes in loading coefficient, such as the operating range at design speed for Krain's impeller, changes in the backsweep parameter have a larger influence than the reduction in loading coefficient.
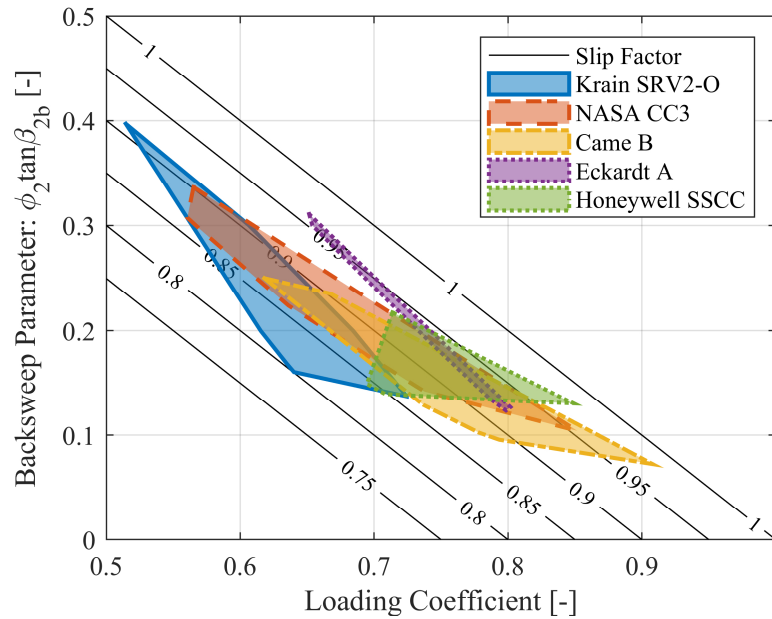
Figure 3.8: The relationship between loading coefficient, backsweep parameter, and slip factor.

3.3.1 Design Implications

The trend of slip factor with machine Mach number and loading coefficient illustrated in Figure 3.7 and Figure 3.8 has significant implications for design. Slip factor decreases more rapidly with increasing machine Mach number, and the minimum value available for slip factor is set by the loading coefficient. This trend is illustrated in Figure 3.9: data in Figure 3.7 has been reorganized to quantify slip factor on the ordinate rather than the machine Mach number. From Figure 3.9, since the slip factor decreases with increasing machine Mach number, large loading coefficients are necessary to maintain high values of slip factor at high impeller tip speeds. The loading coefficient can be increased by decreasing the impeller backsweep at the cost of reduced efficiency and stall margin. Therefore, an optimum loading coefficient exists at which the slip factor is maximized such that the work input lost due to slip is reduced but the impeller efficiency and stall margin are not sacrificed.

Together, Figures 3.7-3.9 represent the first time a robust trend of slip factor has been established in the open literature. The relationship of slip factor with machine Mach number and loading coefficient extends across significantly different impeller designs and is valid at both design and off-design operating conditions. Furthermore, the trend of slip factor provides insight to designers of high-speed machines. As the machine Mach number increases, the slip factor decreases and, additionally, is more sensitive to changes in rotational speed at high machine Mach numbers due to the exponent on the tip speed term. Therefore, high-speed impeller designs are inherently susceptible to low values of slip factor as a result of their high machine Mach number, and high-speed designs with low loading coefficients are especially likely to incur low values of slip factor.

3.4 Impact on Work Input

The efficacy of the slip models in evaluating the work input of each stage was assessed by comparing the measured total temperature rise ratio of each compressor relative to the predictions for each model at each operating point. The general overprediction of slip factor observed in Figure 3.6 is accompanied by an overprediction of work input, Figure 3.10. As in Figure 3.6, the stars in Figure 3.10 show the peak efficiency point at the design speed of each stage, the bar graphs show the normalized distribution of the error data color coded by stage, and a black, vertical, dotted
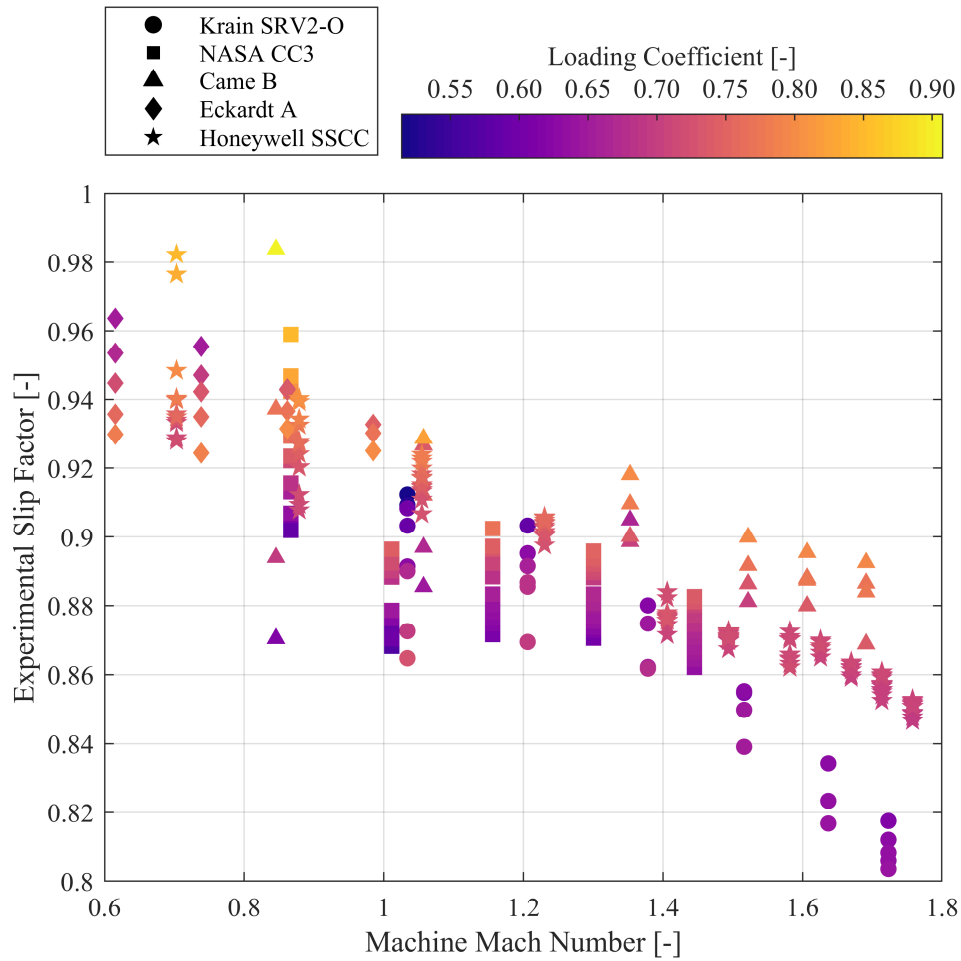
Figure 3.9: Variation of slip factor as a function of machine Mach number and loading coefficient.

line highlights the zero-error location. However, instead of showing the absolute error in slip factor, the abscissa is percent error in the prediction of total temperature rise ratio relative to the measured total temperature rise ratio.

Wiesner's model offers the best overall prediction, but the overprediction of total temperature rise ratio is still significant: at almost half of the operating points, the total temperature rise ratio is overpredicted by more than 5%. Since the largest difference in slip factor between the models and experiments occurred at the greatest speeds for the high-speed impellers, the largest magnitude of error in total temperature rise ratio also occurred at the maximum wheel speed. At design speed, Wiesner's model resulted in an error in total temperature rise ratio of approximately 20% for
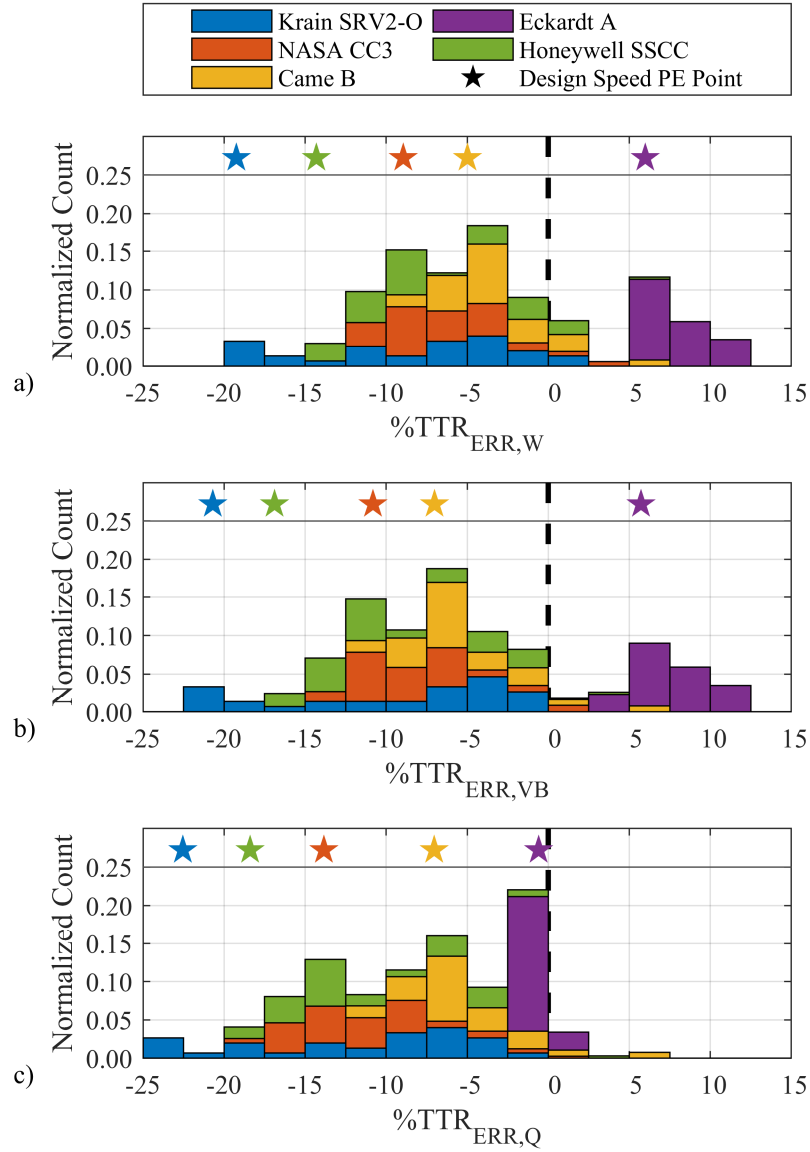
Figure 3.10: Relative error between calculated experimental values of stage TTR and the predicted values of stage TTR for the a) Wiesner slip model, b) von Backström slip model, and c) Qiu slip model for the published operating points of each compressor.

SRV2-O, 10% for CC3, 8% for Came stage B, and 15% for SSCC. The largest error for Wiesner's model applied to Eckardt's impeller occurred at lower speed but resulted in errors on the order of 8%. Von Backström's and Qiu's models result in larger overpredictions of total temperature rise relative to Wiesner's model, but the distribution of the errors is similar across all three models, analogous to the similarities between the models in the overprediction of slip factor in Figure 3.6. For Eckardt's impeller, the absolute error in total temperature rise will generally be smaller than

the absolute error of the high-speed stages because the actual total temperature rise is also relatively small.

The error in total temperature rise ratio can be directly observed in the work plots presented in Figure 3.11. The nearest available speedlines to 80%, 90%, and 100% corrected speed, according to Table 3.1, are given for each compressor. The total temperature rise ratio of the near 80% speedline for each of the high-speed compressors is the most accurately predicted for each model, and the accuracy generally improves at lower speeds not included in the figures (see the full work plot of Krain's impeller in Figure 1.1 for reference). However, as speed increases, the predicted total temperature rise ratio diverges from the experimentally measured work input. Consistent with previous observations that the slip factor suffers from the largest overpredictions at and near design speed, the largest relative errors in Figure 3.10 occur at the design speed of each high-speed impeller. The slip models predict similar magnitudes of work input and extremely similar trends of work input as a function of mass flow rate and loading. The similarities in total temperature rise originate from the similar magnitudes of slip factor predicted by each model for the same impeller as reported in Table 3.2. The only difference between the centrifugal compressor model of each stage is the slip model itself. Therefore, the trend of total temperature rise for each model is almost identical since there is little to no variation of slip factor within each model across the operating range of each stage.

An error propagation analysis was conducted on equation (3.7) to understand how the error in slip factor shown in Figure 3.6 resulted in the large errors in total temperature rise reported in Figure 3.10. The error in total temperature rise ratio is compared between points at the same mass flow rate and impeller tip speed which are the primary drivers of exit flow coefficient. Thus, the exit flow coefficients are assumed to be constant during error propagation. Since the exit flow coefficient is implicitly related with slip factor and total temperature rise ratio, the assumption of constant exit flow coefficient greatly simplifies the analysis and equation (3.11) results:

$$TTR_{ERR} = (\gamma - 1)\sigma_{ERR}M_{U2}^2. \qquad (3.11)$$
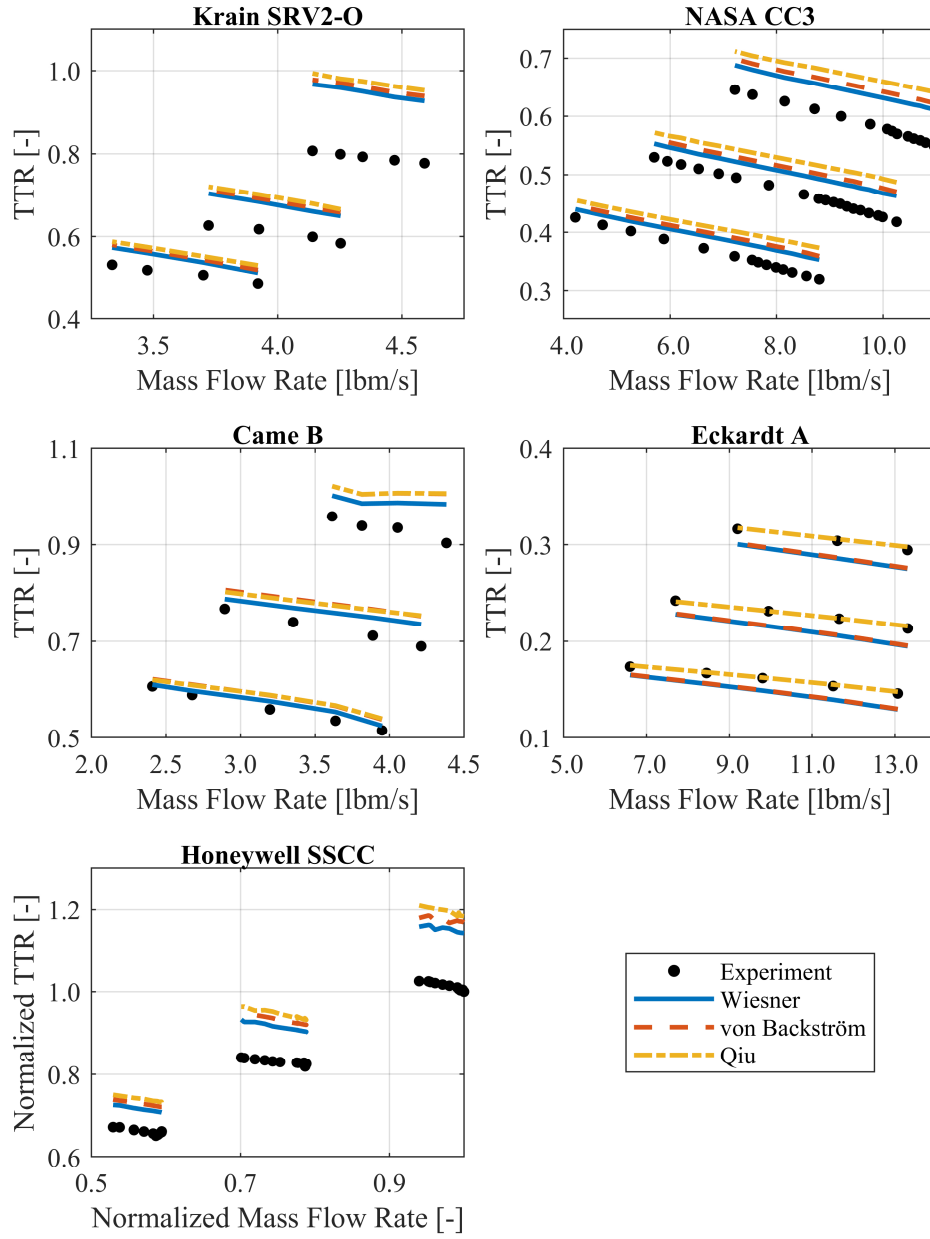
Figure 3.11: Total temperature rise ratio measured in each experiment compared with that predicted by Wiesner's, von Backström's, and Qiu's models for 80%, 90%, and 100% speedlines of each compressor (or nearest available according to Table 3.1).

Equation (3.11) shows that the error in the prediction of total temperature rise ratio, TTR_{ERR}, is only dependent on the error in slip factor, σ_{ERR}, and the square of the machine Mach number. Figure 3.12 illustrates equation (3.11): the same absolute value of error in slip factor is increasingly deleterious for prediction of total temperature rise as the machine Mach number increases. An

error of 0.05 in the predicted slip factor results in a total temperature rise ratio error of about 0.02 at the design intent machine Mach number of Eckardt's impeller. However, at the same value of error in slip factor for a machine Mach number of 1.8 (near the design speed for the Krain, Came, and SSCC impellers), a fairly large error of about 0.06 total temperature rise ratio is expected. Thus, reasonable levels of error in slip factor shown in Figure 3.6 propagate to the large errors in total temperature rise ratio exhibited in Figure 3.10 due to the large machine Mach numbers of the high-speed compressors.
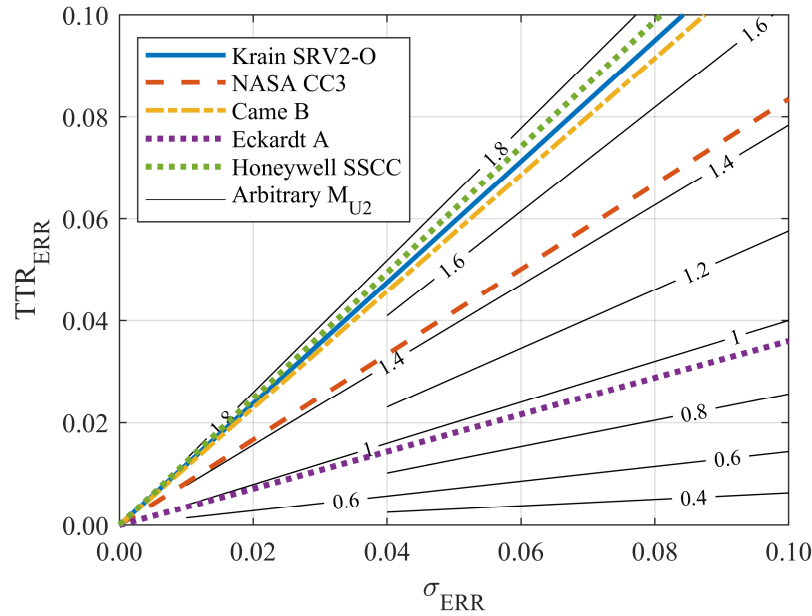
Figure 3.12: Error in predicted TTR as a function of error in predicted slip factor and machine Mach number. The colored lines are the machine Mach number at design speed for each of the stages under investigation.

Equation (3.11), and the corresponding graph in Figure 3.12, challenge whether the traditionally accepted ±0.05 error band for slip factor is satisfactory for both high- and intermediate-speed compressors. To evaluate the error in total temperature rise due to misprediction of slip in the context of the experiments, the ±0.05 slip factor region is compared to the operating range for each of the open literature compressors in terms of total temperature rise ratio and machine Mach number in Figure 3.13. The black line represents a generic impeller with 38 degrees of backsweep operating at an exit flow coefficient 0.20 and a slip factor of 0.90. The error bars are the range of total temperature rise possible at a given machine Mach number when an uncertainty of ±0.05 is

introduced to the slip factor. The error in total temperature rise ratio is similar to, if not larger than, the range of total temperature rise ratio available along an entire speedline for all the compressor stages, especially at the maximum wheel speeds. Recalling from Figure 3.12 that error in total temperature rise ratio scales with the square of the machine Mach number, a ±0.05 error in slip factor results in an error band in total temperature rise ratio comparable to the range of total temperature rise ratio achieved by Eckardt's impeller at design speed despite the relatively low machine Mach number. For Krain's and Came's impellers, the error bar is more than twice as large as the operating range from near choke to stall at 100% speed. Therefore, an error of ±0.05 in slip factor may not be adequate for estimation of the work input for intermediate- and high-speed impellers.
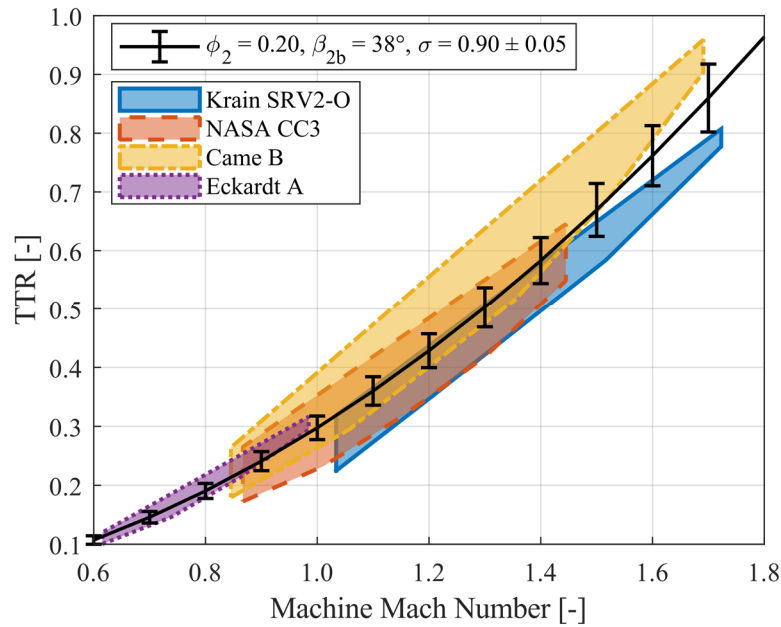
Figure 3.13: Error in TTR for ±0.05 in slip factor compared to the operating range of each of the stages under investigation.

4. DEVELOPMENT OF A NEW APPROACH TO MODELING SLIP AND WORK INPUT

At the time of writing, all slip models in the open literature are derived from the theory of the relative eddy published by Stodola (1927), and most of those models rely exclusively on the impeller geometry. Recent models, such as those published by Qiu et al. (2011) and Stuart et al. (2019) extend the relative eddy approach beyond exclusive dependence on the impeller geometry to capture the variation of slip factor with operating conditions. However, as discussed in the previous chapter, Qiu's model does not reproduce the large variation in slip factor throughout the operating range of high-speed impellers, and Stuart's model, while applicable to meanline models, extends the meanline approach to a pseudo-multi-zone approach. Despite substantial investment from the research community, there is a need for more reliable prediction of slip in preliminary design. Therefore, a new approach to modeling slip and work input for high-speed compressors is introduced that is based on thermodynamics principles instead of the relationship of geometry with complex flow characteristics.

4.1 Derivation of the Method

Some of the proceeding equations and terms have been defined in previous chapters, but they are repeated in the present chapter for clarity in the derivation procedure. The new model approaches the problem of predicting slip factor from a thermodynamic perspective rather than a fluid dynamics perspective due to the difficulty of accurately modeling flow physics in the impeller. Rather than the traditional practice of predicting the slip factor from geometry to calculate impeller work input, the new method directly predicts the work input delivered by the impeller. The predicted work input is then used to calculate slip factor. Since work input is of primary concern in the new method, the Euler turbomachinery equation excluding heat transfer is the starting point of the derivation:

$$-w = \Delta h_0 = c_p \Delta T_0 = \Delta U V_\theta, \qquad (4.1)$$

where w is the work input, h_0 is the stagnation enthalpy, c_p is the specific heat at constant pressure, T_0 is the total temperature, U is the impeller wheel speed, and V_θ is the impeller tangential flow velocity. Equation (4.1) is cast in terms of dimensionless design parameters by dividing both the stagnation enthalpy rise and total temperature rise terms by the square of the impeller exit tip speed and inlet total temperature. Additionally, the specific heat at constant pressure is rearranged in terms of the gas constant, R, and ratio of specific heats, γ, to express the total temperature rise ratio, TTR (a nondimensional measure of the impeller work input), as a function of the loading coefficient, ψ, and machine Mach number, M_{U2}, in equation (4.2),

$$TTR = \frac{\Delta T_0}{T_{01}} = (\gamma - 1)\psi M_{U2}^2. \tag{4.2}$$

The machine Mach number is defined according to equation (4.3),

$$M_{U2} = \frac{U_2}{\sqrt{\gamma R T_{01}}}. \tag{4.3}$$

The governing relationship between total temperature rise ratio, loading coefficient, and machine Mach number in equation (4.2) is leveraged to develop the new model. Both the stagnation enthalpy and total temperature terms used to derive equation (4.2) are dependent on the impeller exit tangential velocity. As shown in Figure 1.6, the impeller exit tangential velocity is dependent on slip, which is unknown in the current approach. Consequently, there are two unknowns, the total temperature rise ratio and the loading coefficient, and equation (4.2) cannot be solved as given. Therefore, the perfect flow guidance loading coefficient, ψ_{PFG}, is introduced which is the loading coefficient for the case that the impeller exit flow exactly follows the blades. The perfect flow guidance loading coefficient corresponds to the perfect flow guidance impeller exit tangential velocity, $V_{\theta 2,PFG}$ in Figure 1.6. Equation (4.2) is both multiplied and divided by the perfect flow guidance loading coefficient, resulting in equation (4.4),

$$TTR = (\gamma - 1)\chi\psi_{PFG}M_{U2}^2, \tag{4.4}$$

where χ is the ratio of the actual loading coefficient to the perfect flow guidance loading coefficient:

$$\chi = \frac{\psi}{\psi_{PFG}}. \tag{4.5}$$

Equation (4.4) is mathematically identical to equation (4.2), but the terms have been manipulated to give the actual total temperature rise ratio delivered by the impeller as a function of the perfect flow guidance loading coefficient as well as the ratio of the actual loading coefficient to the perfect flow guidance loading coefficient. While the actual loading coefficient is unknown due to its dependence on the slip factor, at the perfect flow guidance condition, the slip factor is, by definition, equal to one. Therefore, the perfect flow guidance loading coefficient can be directly calculated from the meanline equations.

Since equation (4.4) is a mathematically valid relationship, the term that must be modeled, the ratio of loading coefficients, is not required to be the primary driver of the model. Instead, the machine Mach number and loading coefficient inherently approximate both the magnitude and trend of the total temperature rise ratio, and modeling of the ratio of loading coefficients serves as a correction for magnitude.

The trend of the ratio of loading coefficients with various dimensionless quantities (such as specific speed, mass flow coefficient, machine Mach number, and impeller exit flow coefficient) was investigated. Generally, the ratio of loading coefficients was found to be weakly correlated with individual dimensionless design parameters but more strongly correlated with products of the dimensionless quantities that included measures of the impeller shape factor, impeller tip speed, and compressibility. After extensive vetting of various combinations of parameters, the product of the inlet flow coefficient and square of the machine Mach number was chosen. A product of these parameters is given in dimensional form in equation (4.6) for reference:

$$M_{U2}^2 \phi_1 = \frac{\pi}{4} \left(\frac{r_1}{r_2}\right)^2 \left(\frac{\rho_1}{\rho_{01}}\right) \left(\frac{V_{m1} U_2}{a_{01}^2}\right), \tag{4.6}$$

where ρ_1 is the inlet static density, ρ_{01} is the inlet stagnation density, r_1 is the inlet root mean square radius, r_2 is the impeller exit radius, V_{m1} is the inlet meridional velocity, and a_{01} is the speed of sound based on inlet stagnation conditions. The flow coefficient, ϕ_1, is defined as

$$\phi_1 = \frac{\dot{m}}{\rho_{01} D_2^2 U_2}, \tag{4.7}$$

where $\dot{m}$ is the mass flow rate, and D_2 is the impeller exit diameter. From equation (4.6), the dimensionless parameters incorporate a measure of the impeller shape factor through the radius ratio which has often been observed to influence slip factor (Busemann, 1928; Wiesner, 1967). Additionally, the impeller exit tip speed and compressibility at the impeller inlet contribute to the correction from perfect flow guidance conditions to actual conditions. Other combinations of dimensionless parameters also provided satisfactory correlations, but together, the square of the machine Mach number and flow coefficient provided the best combination of minimal scatter throughout the dataset and low error at high machine Mach numbers (i.e., at or near design speed).

The general form of the model is obtained by substituting in the square of the machine Mach number and the inlet flow coefficient for the ratio of loading coefficients, equation (4.8):

$$TTR = A\psi_{PFG} M_{U2}^2 (M_{U2}^2 \phi_1)^B. \tag{4.8}$$

The ratio of specific heats is assumed to be constant and is absorbed into the coefficient A. The ratio of loading coefficients, χ, is not directly present since it is modeled by the product of the inlet flow coefficient and square of the machine Mach number raised to the power of coefficient B. The coefficients A and B are determined from a nonlinear regression analysis and, as is discussed in detail in the proceeding sections, may be prescribed per the recommended general values, customized to fit specific impeller families, or tailored to fit the implementation of the model.

Detailed procedures for the regression analysis, incorporation of the model into meanline analysis tools, and calculation of the slip factor itself are given in the appendices.

4.2 Evaluation of the Method

The new model supports various methods of implementation, and thus, can be customized to fit the needs of the user. The general and family implementations of the model are considered first, indicated in figures by the GEN and FAM subscripts, respectively. Each implementation uses the definition of the model given in equation (4.8), but the coefficients *A* and *B* are calculated differently depending on the implementation.

A weighted nonlinear regression analysis was conducted on equation (4.8) to determine the coefficients *A* and *B* for the general application of the model. All the operating points available for the four open literature impellers were included in the analysis, but each stage was given equal total weighting such that stages with smaller data sets had the same influence on the regression as those with many points, such as the CC3 impeller. The general values for *A* and *B* in the first row of Table 4.1 are recommended as the default coefficients in the model. The family coefficients are also determined through nonlinear regression analysis, but the analysis is performed on each stage individually such that coefficients *A* and *B* are unique to each impeller. The values of *A* and *B* resulting from individually conducted nonlinear regression analyses on each of the open literature impellers are also given in Table 4.1. The general implementation of the model is intended for use in design cases where slip factor data from a reference impeller are not available for nonlinear regression analysis. The general coefficients are weighted towards high-speed application, but the together the four impellers represent a broad range of specific speed and loading. Thus, the coefficients are developed with the intent of applicability throughout the centrifugal compressor design space. The family implementation is recommended when an existing design is being modified and performance data at numerous operating conditions are available for regression analysis.

Throughout the proceeding analysis, the Honeywell SSCC impeller is used as a validation case for general implementation of the new model. The slip factor of the Honeywell SSCC impeller was

Table 4.1: Model coefficients *A* and *B* for various implementations of the new model.

Implementation	Compressor	*A*	*B*
General	General	0.26	-0.10
Family	Krain SRV2-O	0.25	-0.12
Family	NASA CC3	0.28	-0.06
Family	Came B	0.30	-0.05
Family	Eckardt A	0.36	-0.01

predicted using the coefficients *A* and *B* for the general implementation of the new model as calculated from the open literature compressors and given in the first row of Table 4.1. Therefore, the open literature cases provide an evaluation of the accuracy of the new model, and data associated with the SSCC impeller provide validation data to evaluate the predictive capability of the model. The results for the Honeywell SSCC validation case are shown alongside that of the open literature cases in most of the discussion. Since the family implementation of the model is customized for each impeller design, a validation case is not appropriate and is not included. The SSCC impeller is included in discussion of the family implementation to provide an additional data set for assessment of the new model.

4.2.1 Results

The differences between the calculated experimental slip factor and the slip factor predicted by Wiesner's model, the general implementation of the new model, and the family implementation of the new model are given in Figure 4.1a, Figure 4.1b, and Figure 4.1c, respectively. As in the bar graphs presented in Chapter 3, the bar graphs in Figure 4.1 show the distribution of the error data color coded by stage, and the black, vertical, dashed line highlights the zero-error location. Overpredictions of slip factor, are indicated by negative values to the left of the zero-error line, while underpredictions of slip factor are positive and to the right. The stars above the bar graph indicate the error in predicted slip factor at the design speed peak efficiency point of each stage. Each stage is given equal visual representation in the bar plots by normalizing the ordinate such that that a single stage with a large data set does not skew interpretation of the data.
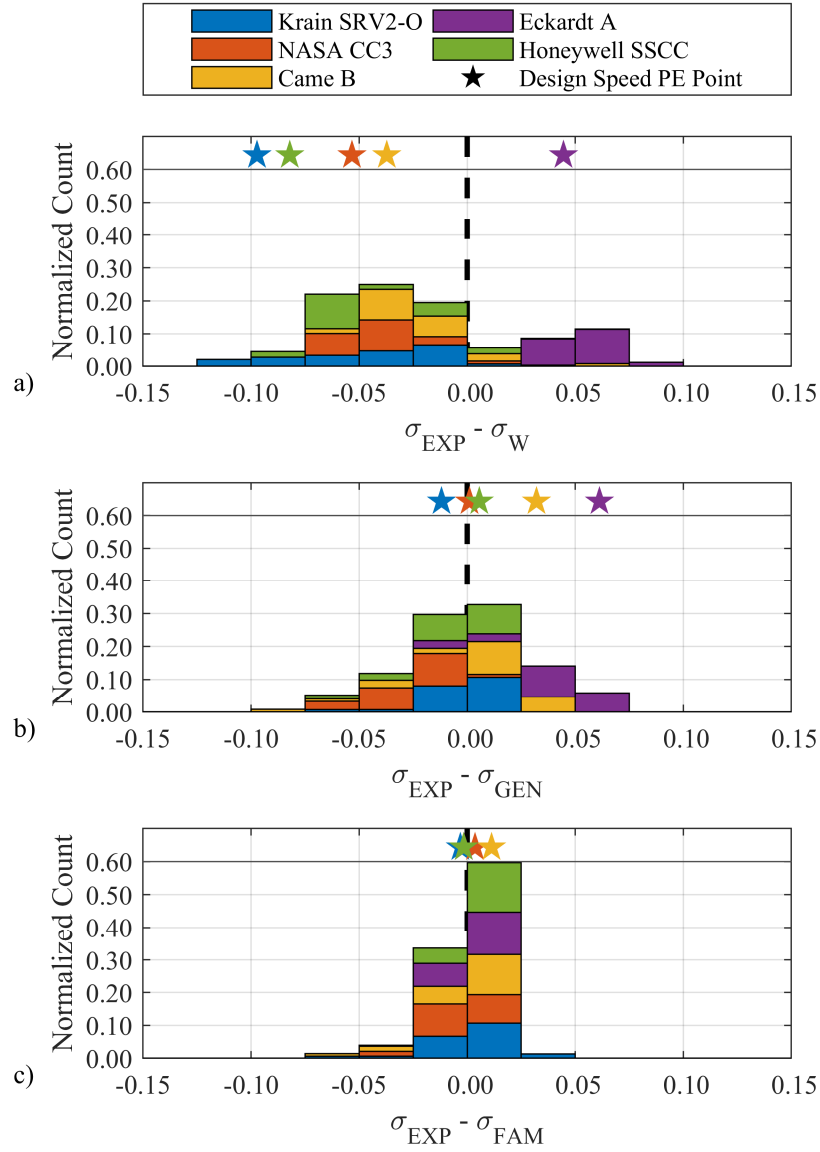
Figure 4.1: Difference between calculated and experimental values of slip factor and predicted values of slip factor for the a) Wiesner slip model, b) new slip model, general implementation, and c) new slip model, family implementation.

Both the general and family implementations of the new model result in a normal distribution of error in predicted slip factor centered around 0 error, while there is broad, irregular scatter in the error distribution resulting from Wiesner's model. Additionally, the range of error for both implementations of the new model is smaller than that of Wiesner's model. The scatter of the error distributions depicted in Figure 4.1 is quantified in Table 4.2. The general and family implementations of the new model predict more than 60% and 90% of the data, respectively, within

Table 4.2: Percent of data in Figure 4.1 within error bands of ±0.025 and ±0.050 in slip factor.

Slip Factor Error	Wiesner	New, General	New, Family
±0.025	25%	62%	93%
±0.050	52%	88%	99%

±0.025 of the experimental slip factor, while Wiesner's model captures just over 50% of the data within ±0.05. Specifically for the SSCC validation case, 83% of the data are predicted within the ±0.025 error band, which supports application of the general implementation to impellers not included in the regression analysis.

Traditional geometry-based approaches to modeling slip factor were shown to exhibit large levels of error at design speed for high-speed compressors in Chapter 3, and this can be seen for Wiesner's model in Figure 4.1a. Of the high-speed compressors, only the design point slip factor of Came's impeller is predicted within the traditionally accepted ±0.05 error band. The new model shows significant improvement in predicting slip factor at the design speed peak efficiency point for both the general and family implementations. Although the slip factor predicted for Eckardt's impeller is outside the ±0.05 band for the general method, the high-speed stages are all within the band. For the family implementation, the design point slip factor is predicted within ±0.025 for all cases.

Since errors in the prediction of slip factor propagate to errors in work input, the ability of the new model to predict work input is also considered, Figure 4.2. As in Figure 4.1, the zero-error location is highlighted by a black, vertical, dashed line, and stars across the top of the graph indicate the error at the design speed peak efficiency point. However, the abscissa now shows the relative error in total temperature rise ratio rather than absolute error in slip factor. The large error range in slip factor for Wiesner's model (Figure 4.1a) propagates to larger mispredictions of work input. Less than 35% of the data are predicted within ±5% of the actual work input, and at design speed, errors of at least 5%, and up to 20%, are observed. The errors observed for the new model are also larger but remain normally distributed about 0% error. More than 70% and 90% of the predictions are within ±5% of the actual work input for the general (Figure 4.2b) and family (Figure 4.2c)
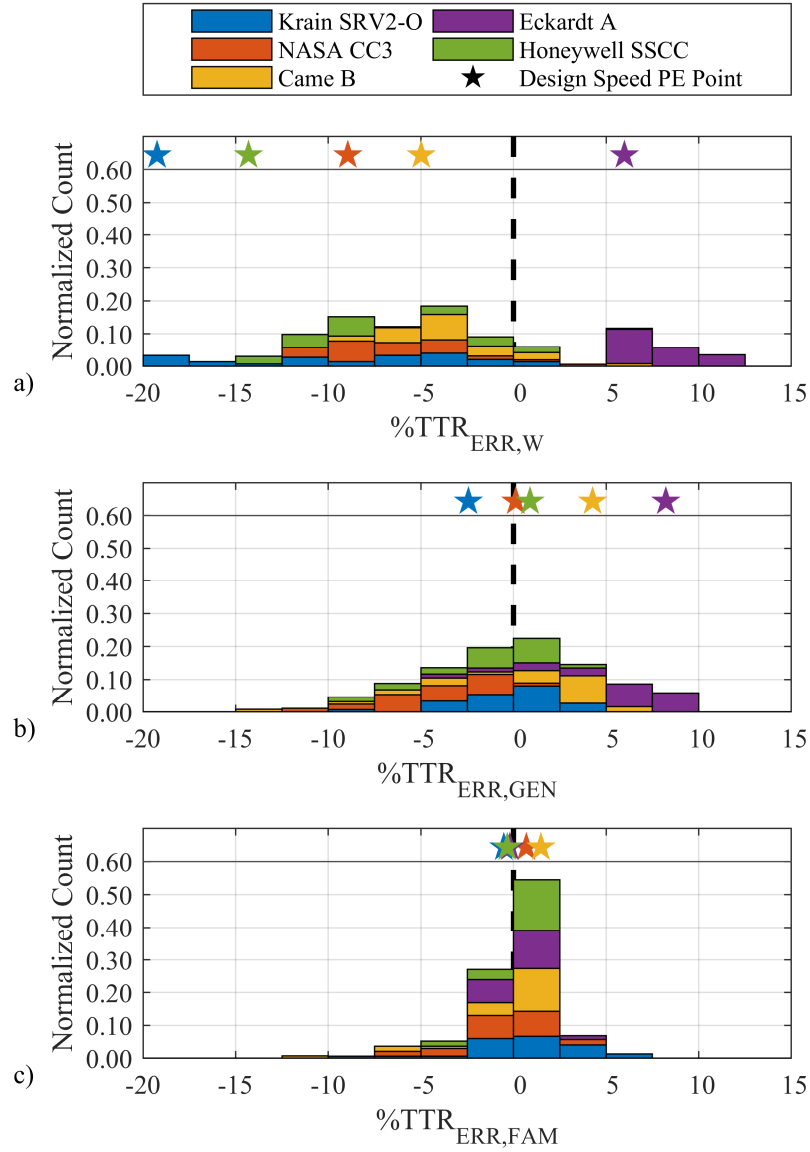
Figure 4.2 Relative error in predicted total temperature rise ratio for the a) Wiesner slip model, b) new slip model, general implementation, and c) new slip model, family implementation.

implementations of the new model, respectively. Additionally, the design point total temperature rise ratio predication is within ±2.5% error for the family implementation. The design point error is larger for the general implementation but still represents an improvement relative to Wiesner's model when applied to high-speed impellers.

Prediction of the work input for the SSCC case using the general implementation of the model again supports application of the new model to the broader centrifugal compressor design space.

102

The model predicts the total temperature rise ratio for 68% of the SSCC operating points within ±2.5% relative error, and the slip factor at design point is predicted with an error of less than 1%.

The improvement in prediction of total temperature rise ratio can be observed through comparison of the work plots for each of the compressors as measured in experiments and predicted by each of the slip models, Figure 4.3. All three models provide good estimates of the work input at low speed, but as speed (i.e., machine Mach number) increases, the prediction provided by Wiesner's model diverges from the experimental data, as documented in the previous chapter. In contrast, both implementations of the new model provide good estimates of the work input throughout the operating range of the high-speed impellers. The general implementation of the new model, which is the less accurate implementation, provides better estimates of the compressor work than Wiesner's model at all speedlines except the design speed of Eckardt's impeller, in which case it is comparable to Wiesner's model. The larger relative errors for the general implementation as applied to Eckardt's impeller are likely due to its weak dependence on the coefficient B as given in Table 4.1. The family implementation almost exactly replicates the work for all five compressors.

4.2.2   Discussion

To support discussion of the results, the relationship between slip factor, machine Mach number, loading coefficient, and total temperature rise is explored by considering the case of an impeller operating with axial inlet flow. For the case with no pre-whirl, the loading coefficient can be defined as

$$\psi = \frac{V_{\theta 2}}{U_2}.$$
(4.9)

Recalling the impeller exit velocity triangle from Figure 1.6, the exit tangential flow velocity is

$$V_{\theta 2} = U_2 - V_{slip} - V_{m2} \tan \beta_{2b}$$
(4.10)
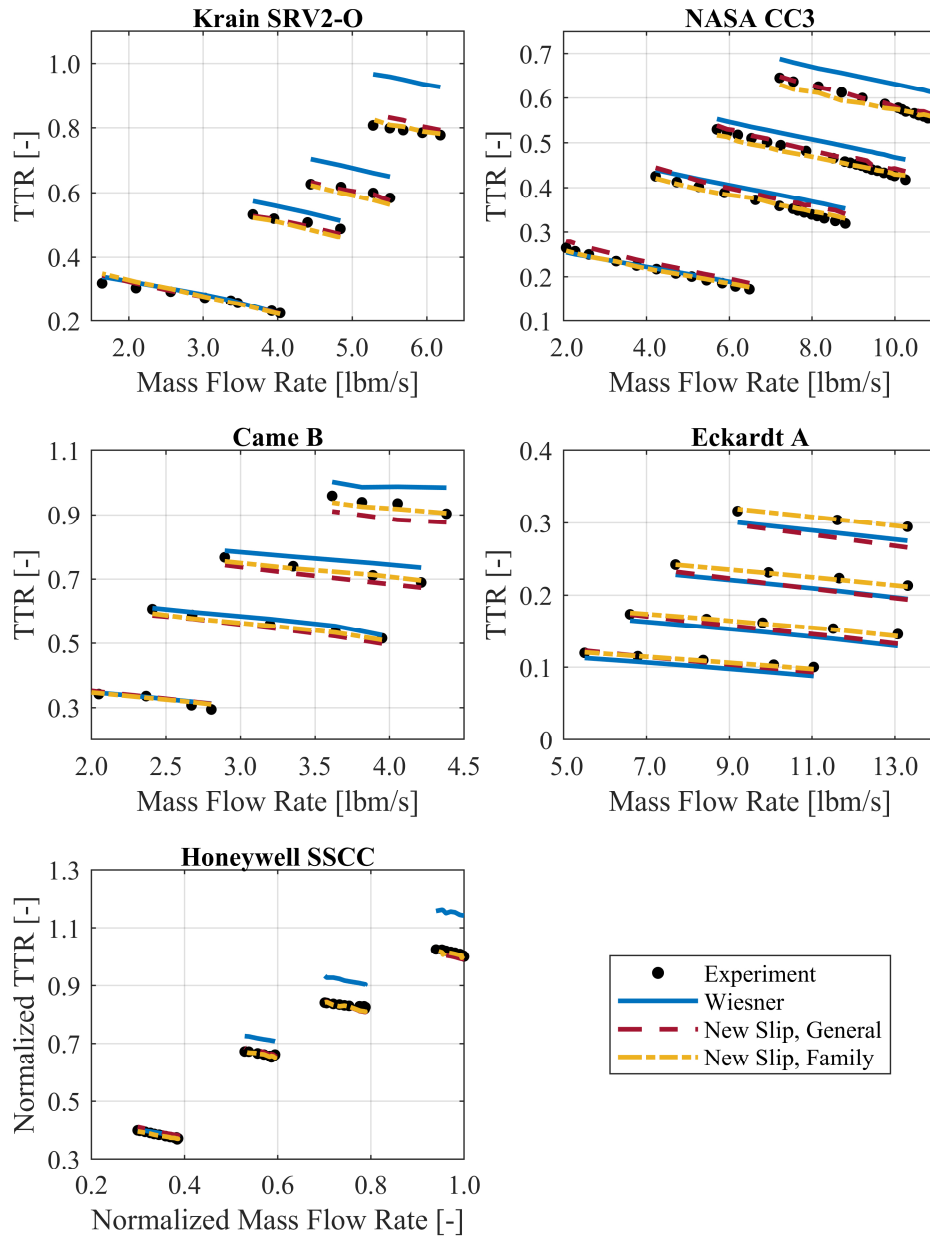
Figure 4.3: Total temperature rise ratio measured in each experiment compared with that predicted by Wiesner's, general implementation of the new slip model, and family implementation of the new slip, family for 60%, 80%, 90%, and 100% speedlines (or nearest available according to Table 3.1) of each compressor.

where V_{slip} is the slip velocity, V_{m2} is the impeller exit meridional velocity, and β_{2b} is the impeller exit blade angle. Combining equations (4.9) and (4.10) with the definition of slip factor,

$$\sigma = 1 - \frac{V_{slip}}{U_2}, \tag{4.11}$$

gives equation (4.12),

$$\sigma = \psi + \phi_2 \tan\beta_{2b}, \tag{4.12}$$

where the slip factor is cast in terms of the loading coefficient, the blade exit angle, and the impeller exit flow coefficient, ϕ_2, which is the ratio of impeller exit meridional flow velocity to the impeller exit tip speed:

$$\phi_2 = \frac{V_{m2}}{U_2}. \tag{4.13}$$

Finally, equation (4.12) is utilized to substitute the slip factor, exit flow coefficient, and blade exit angle into equation (4.2) in place of the loading coefficient, which is rearranged to give the slip factor in terms of dimensionless parameters:

$$\sigma = \frac{TTR}{(\gamma - 1)M_{U2}^2} + \phi_2 \tan\beta_{2b}. \tag{4.14}$$

Numerous investigations have confirmed the slip factor varies as a function of the compressor operating conditions (Cumpsty, 1989; Dean, 1971; Eckardt, 1978; Sakai et al., 1967; Stahler, 1965). However, traditional models derived from the relative eddy approach, such as Wiesner's model, are dependent only on the impeller geometry and cannot capture the variation of slip factor with operating conditions driven by equations (4.12) and (4.14). Some recent relative eddy approaches have incorporated the impeller exit flow coefficient to account for the variation of slip factor with operating conditions (Qiu et al., 2011; Stuart et al., 2017), but these methods dilute the influence of the machine Mach number in equation (4.14). The variation of the exit flow coefficient

throughout the compressor map is usually small relative to the range of machine Mach numbers available to high-speed compressors, and furthermore, the machine Mach number is raised to a larger power than the exit flow coefficient.

Thus, the relationship of slip factor with machine Mach number in Figure 4.4 is not captured by relative eddy models, regardless of exit flow coefficient inclusion. As the machine Mach number increases, the slip factor decreases both as a general trend and for each individual design. The dependence of slip factor on machine Mach number and increasing influence of machine Mach number at high tip speeds also drives the increasing overprediction of work input with wheel speed between Wiesner's model and the experimental results observed in Figure 4.3. In contrast to geometry-based models, the new model inherently incorporates the influence of the machine Mach number on slip factor through equation (4.14), emulates the trend of slip factor in Figure 4.4, and supports accurate characterization of the trend of slip factor with compressor operating conditions. Additionally, significant improvement in the prediction of the slip factor is attained at and near design speed for the high-speed impellers where influence of the machine Mach number is large.
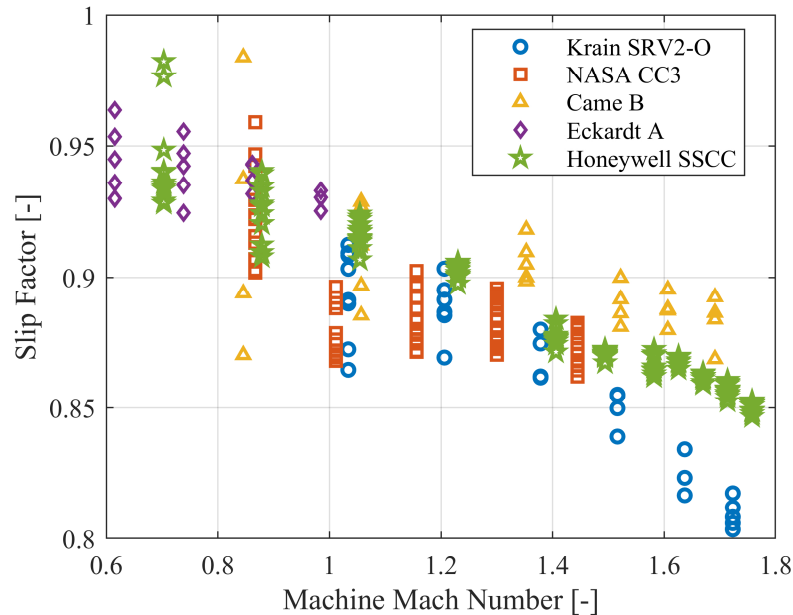
Figure 4.4: Relationship of slip factor with machine Mach number.

As previously shown in Figure 3.7, Figure 4.4 also shows that a range of values for slip factor are possible for a single machine Mach number (i.e., along a speedline). The new model captures this behavior through incorporation of the loading coefficient and flow coefficient, supporting the capability of the new model to capture the variation of slip factor throughout the compressor map.

Reversing the direction of the error propagation between slip factor and total temperature rise ratio also provides accuracy benefits to the new method. Traditional slip models calculate a slip factor, from which the work input delivered by the impeller is determined. To understand how the error in predicted slip factor cascades to the total temperature rise ratio, the error propagation analysis conducted in Chapter 2 is revisited. The impeller exit flow coefficient and machine Mach number in equation (4.14) are again considered constant, and error propagation analysis on equation (4.14) gives the error in total temperature rise ratio, TTR_{ERR}, as

$$TTR_{ERR} = (\gamma - 1)\sigma_{ERR}M_{U2}^2. \tag{4.15}$$

From equation (4.15), the error in slip factor, σ_{ERR}, is propagated to total temperature rise ratio scaled by the square of the machine Mach number for traditional slip models. Figure 3.12 illustrates equation (4.15): as the machine Mach number increases, the same level of error in slip factor is increasingly deleterious for the prediction of total temperature rise ratio. Thus, the errors in slip factor predicted by Wiesner's model in Figure 4.1 propagate to large errors in total temperature rise in Figure 4.2. The new method uses a predicted total temperature rise ratio to calculate the slip factor, so the direction of error propagation is reversed: the error in predicted total temperature rise ratio propagates to error in slip factor but is divided by the square of the machine Mach number. Consequently, the new method can tolerate larger mispredictions since the error propagation from total temperature rise ratio to slip factor reduces the magnitude of the absolute error in slip factor for machine Mach numbers greater than one.

In addition to providing high levels of accuracy, the new model is ideal for use in the preliminary design phase when basic parameters such as flow areas, velocity triangles, and thermodynamic states are set. At present, all other slip models require the specification of the number of impeller blades and/or backsweep angle, if not blade thickness and other geometric parameters, as well.

The new model relies only on dimensionless parameters that are fundamental to compressor design, and no additional parameters beyond those required to solve the meanline equations must be introduced to estimate the slip factor with the new model.

Though the model is not able to directly account for the radial component of inlet flow velocity that may arise from some irregular inlet ducts, the new model is expected to be compatible with axisymmetric swirl at the impeller inlet. The inlet swirl should be accounted for through the effect of the inlet flow angle on the loading coefficient. Unfortunately, direct consideration of the effect of non-axial inlet flow on slip factor and the model was not possible in the present work since axial inlet flow was provided to all the available datasets.

Because the new model is dependent only on design parameters and derived from governing relationships, it provides both improved estimation of the slip factor and ease of use in preliminary design. However, application of the model is unconventional. While traditional slip models use a predicted value for slip factor to calculate impeller work input, the new model directly predicts the work input, and the slip factor is solved for in the system of meanline equations. A one-dimensional analysis tool is, therefore, necessary to provide a solution to the meanline equations and a value for slip factor, whereas relative eddy models supply a value for slip factor based only on the impeller geometry. As such, the new model is intended specifically for use in meanline solvers for centrifugal compressors as outlined in Appendix B.

4.3   Considerations for External Losses

Internal losses only affect the entropy generation of the stage and have negligible bearing on the work input delivered by the impeller. In contrast, external losses (such as disc friction and recirculation) contribute to the overall stage total temperature rise ratio without providing additional total pressure rise. At a given operating point where the impeller wheel speed, mass flow rate, and total temperature rise ratio are constant, increasing levels of external loss correspond to reduced impeller work input. By extension, the slip factor must decrease to support the reduction in impeller work input. External losses must, therefore, be accounted for when relating slip factor,

total temperature rise ratio, and loading coefficient. Whitfield & Baines (1990) and Japikse & Baines (1994) provide additional details on internal and external losses.

Exact allocation of external losses is possible in 1D modeling. As such, all references to the total temperature rise ratio and loading coefficient up to this point have been to those parameters as specifically associated with the impeller: the external losses have not been included. Separating the total temperature rise due to the impeller and external losses is recommended since equation (4.4) is defined specifically for the work input generated by the impeller. However, the percentage of the temperature rise delivered by the impeller versus external losses often cannot be rigorously partitioned in experiments. Therefore, the model coefficients are recalculated per the procedures in Appendix A with the external losses included in both the perfect flow guidance loading coefficient and total temperature rise ratio terms, Table 4.3.

Table 4.3: Model coefficients A and B with external losses included for various implementations of the new model.

Implementation	Compressor	A	B
General+EXT	General	0.25	-0.11
Family+EXT	Krain SRV2-O	0.23	-0.15
Family+EXT	NASA CC3	0.27	-0.07
Family+EXT	Came B	0.27	-0.08
Family+EXT	Eckardt A	0.37	0.00

The new model is robust to the inclusion of external losses, Figure 4.5 and Figure 4.6. The absolute error in slip factor and relative error distribution for the total temperature rise ratio predicted by Wiesner's model are shown again in Figure 4.5a and Figure 4.6a, respectively, for comparison to the new model. From Figure 4.5, the new model provides improved prediction of slip factor relative to Wiesner's model when external losses are included. There is a slight increase in scatter for design points of the family implementation when external loss is included, and the general implementation is largely unchanged. Overall, the accuracy of the method for prediction of the
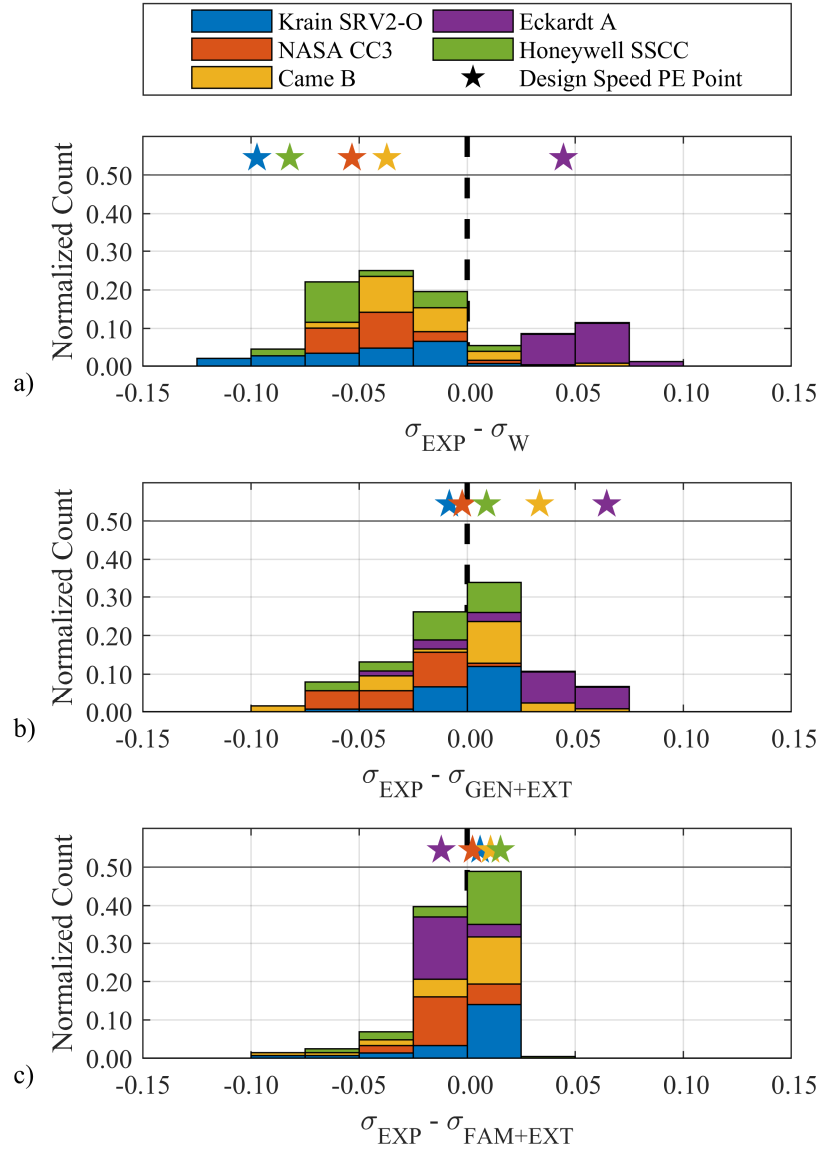
Figure 4.5: Difference between calculated and experimental values of slip factor and predicted values of slip factor for the a) Wiesner slip model, b) new slip model, general implementation including external losses, and c) new slip model, family implementation including external losses.

slip factor is maintained when the enthalpy rise due to external losses cannot be separated from the work input to flow by the impeller blades.

Figure 4.6b and Figure 4.6c show the error distribution for the predicted total temperature rise ratio of the general and family implementations of the new model including external losses. The SSCC impeller again gives validation for general implementation of the model. The inclusion of external

110
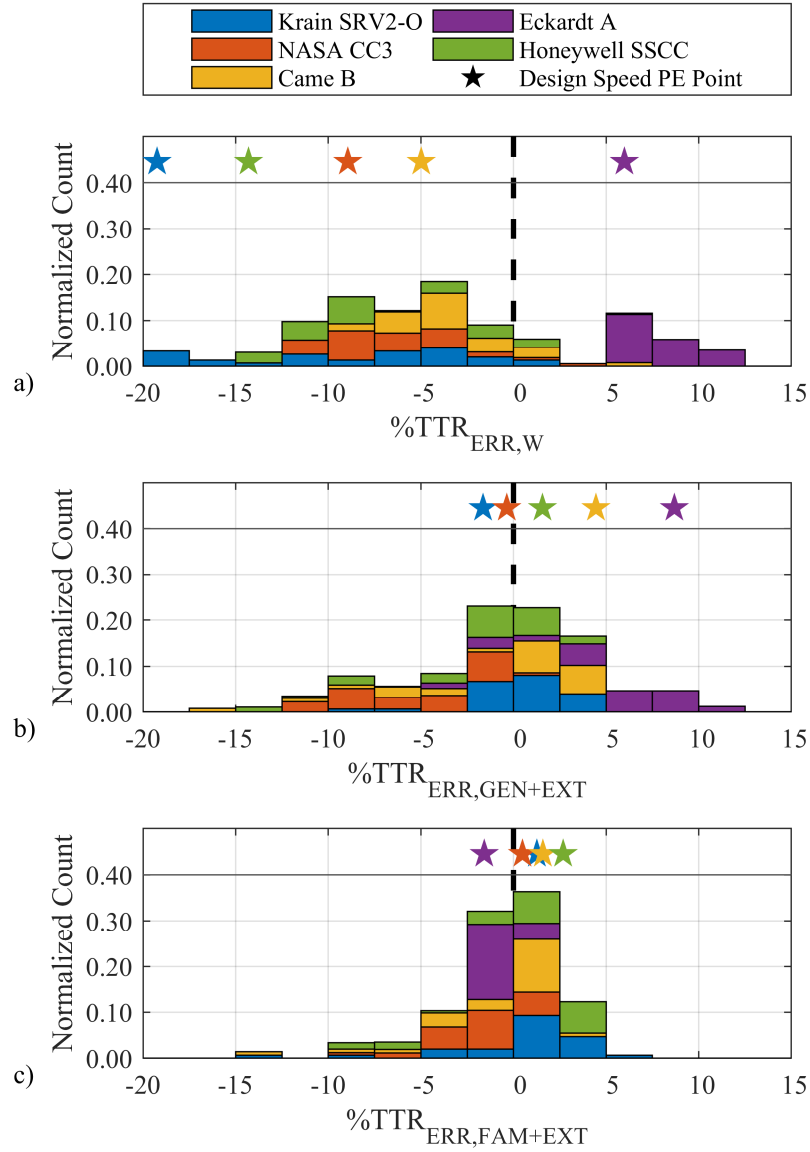
Figure 4.6: Relative error in predicted total temperature rise ratio for the a) Wiesner slip model, b) new slip model, general implementation including external losses, and c) new slip model, family implementation including external losses.

losses in the regression analysis results in more scattered error distributions for both implementations of the model. However, the accuracy remains improved relative to Wiesner's model, particularly at design point for the high-speed compressors and for the family implementation of the model.

In the present work, 20% of the overall loss is attributed to external losses at all operating points. In actual operation, the distribution of internal and external losses will vary as a function of the mass flow rate and loading coefficient (e.g., Figure 2.5, Figure 2.6, Figure 2.7, and Figure 2.8). The information required to replicate the actual variation of external losses between operating conditions within each stage is not given in the open literature, hence the ability of the new model to predict slip factor with varying external loss distributions cannot be directly examined.

However, the sensitivity of the model coefficients to the prescribed internal/external loss distribution can be considered, Figure 4.7. The coefficients for the general implementation of the model are shown as a function of the overall loss assigned to external losses for both the base model implementation as well as with external losses included. The coefficients of the family implementation of the new model for each open literature case at 20% external loss allocation (given in Table 4.1) are shown for reference. As external losses increase, less of the stage total temperature rise is provided by the impeller and a larger correction from the perfect flow guidance condition to the actual operating condition is required. Thus, both coefficients A and B decrease with increasing external losses. The same reasoning applies to the difference between the general implementation and general implementation with external losses. A larger correction is necessary when external losses are included since external losses are incorporated in correlating the perfect flow guidance condition to the actual operating condition. At 0% external loss there are no external losses, so the coefficients of the GEN and GEN+EXT implementations of the model converge.

The sensitivity of the coefficients to external losses is smaller than the range of values for the family coefficients of each stage. In fact, when external losses are excluded, the change in the coefficients across the large 30% variation in external loss distribution is similar to the variation of the coefficients within only the high-speed stages. Therefore, while the effect of varying external losses between operating points cannot be directly investigated, the accuracy of the model with the inclusion of external losses in Figure 4.5 and Figure 4.6, the insensitivity of the model coefficients to the external loss distribution in Figure 4.7, and the basis of the model in governing relationships give confidence that the model is compatible with variable external losses.
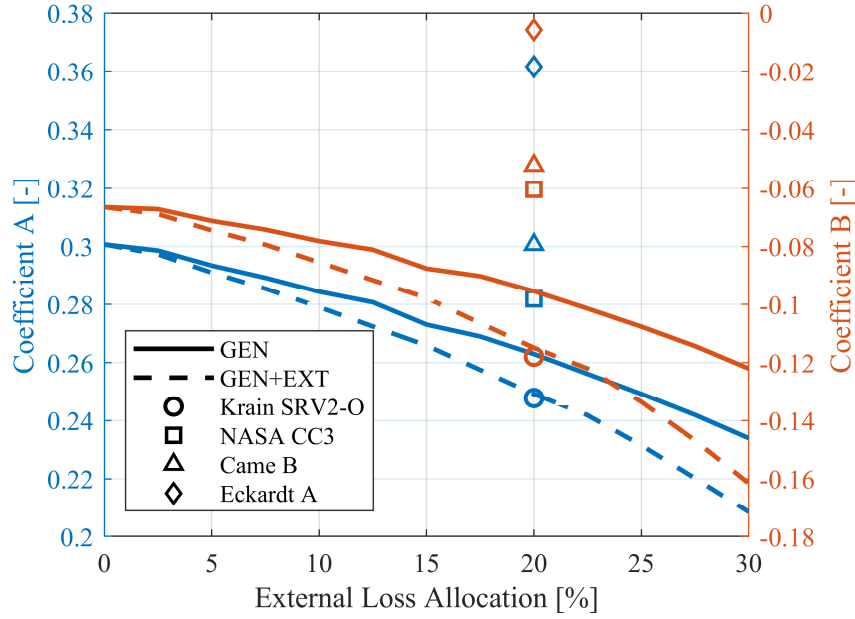
Figure 4.7: Relationship of the model coefficients *A* and *B* with the distribution of internal and external losses. The coefficients of the new model at the 20% external loss allocation for the family implementation are shown for reference.

4.4 Considerations for Blockage

To this point, blockage has not been considered for two primary reasons: (1) some researchers consider modeling blockage to be fundamentally inconsistent with the meanline modeling approach, and (2) little information and discussion of blockage models is available in the open literature. However, some organizations argue that since there is no mass flux through the blocked regions of the flow area, the meanline flow properties cannot accurately represent the properties of the zero-mass flux area. From this perspective, blockage must be modeled to accurately represent the flow field with meanline parameters. The capacity of the model to predict slip and work input in conjunction with the use of blockage is, therefore, investigated. The five compressors are modeled according the same procedures given in the current chapter, but a constant blockage equivalent to 10% of the impeller exit flow area is applied at each operating point. The 10% blockage is also carried over to Stanitz's vaneless diffuser loss model for consistency. The resulting error distributions of slip factor and total temperature rise ratio are given in Figure 4.8 and Figure 4.9, respectively. Wiesner's model, the general implementation of the new model, and the family implementation of the new model are show in subfigures (a), (b), and (c), respectively.

Incorporating 10% flow blockage at the impeller exit generally reduces the error in slip factor for Wiesner's model, Figure 4.8a. The slip factor predicted by Wiesner's model is unchanged since the model is independent of the flow conditions. Conversely, the value of slip factor calculated from the experimental matching procedure is a function of blockage, and the change in the experimental slip factor drives the overall reduction of error. As blockage increases, the impeller exit meridional velocity must increase to maintain the same mass flow rate for a reduced effective flow area (with the assumption of constant density), and changes to the meridional velocity affect the entire impeller exit velocity triangle. The impeller exit tangential flow velocity remains the same since it is constrained to match the velocity required to generate the total temperature rise ratio measured in the experiment. Therefore, the slip velocity and backsweep velocity components must change with the incorporation of blockage. Slightly larger values of experimental slip factor result with the incorporation of 10% flow blockage, and the slip factor predicted by Wiesner's model is more representative of the slip factors of the high-speed impellers with 10% blockage than 0% blockage. Eckardt's impeller is the exception to the improvement in accuracy, however. Wiesner's model underpredicted the slip factor without blockage, and adding blockage increases the magnitude of the underprediction.

Incorporating blockage into the new model has little effect on the accuracy in the prediction of slip factor for either implementation, Figure 4.8b and Figure 4.8c. The scatter of the distributions around zero-error is largely unchanged, and the design point prediction appears to be slightly improved.

The relative error in total temperature rise ratio for each model is shown in Figure 4.9. For Wiesner's model (Figure 4.9a), the error in predicted total temperature rise at the design point for the high-speed stages decreases with the incorporation of blockage, but the overall scatter of the error distribution remains approximately the same. The error distributions of the total temperature rise ratio for the general and family implementations of the new model also remain largely unchanged with the incorporation of blockage. The design point prediction of total temperature rise ratio improves slightly for both implementations of the new model relative to the case without blockage. Both the experimental data and perfect flow guidance data are calculated with 10% flow blockage, and the effect of blockage is accounted for in correlating the perfect flow guidance

114

Figure 4.8: Difference between calculated and experimental values of slip factor and predicted values of slip factor with 10% impeller exit blockage for the a) Wiesner slip model, b) new slip model, general implementation, and c) new slip model, family implementation.

operating conditions to the experimental operating conditions. Thus, like with external losses, the new model is insensitive to the incorporation of blockage because blockage is inherently incorporated into the model through equation (4.2).
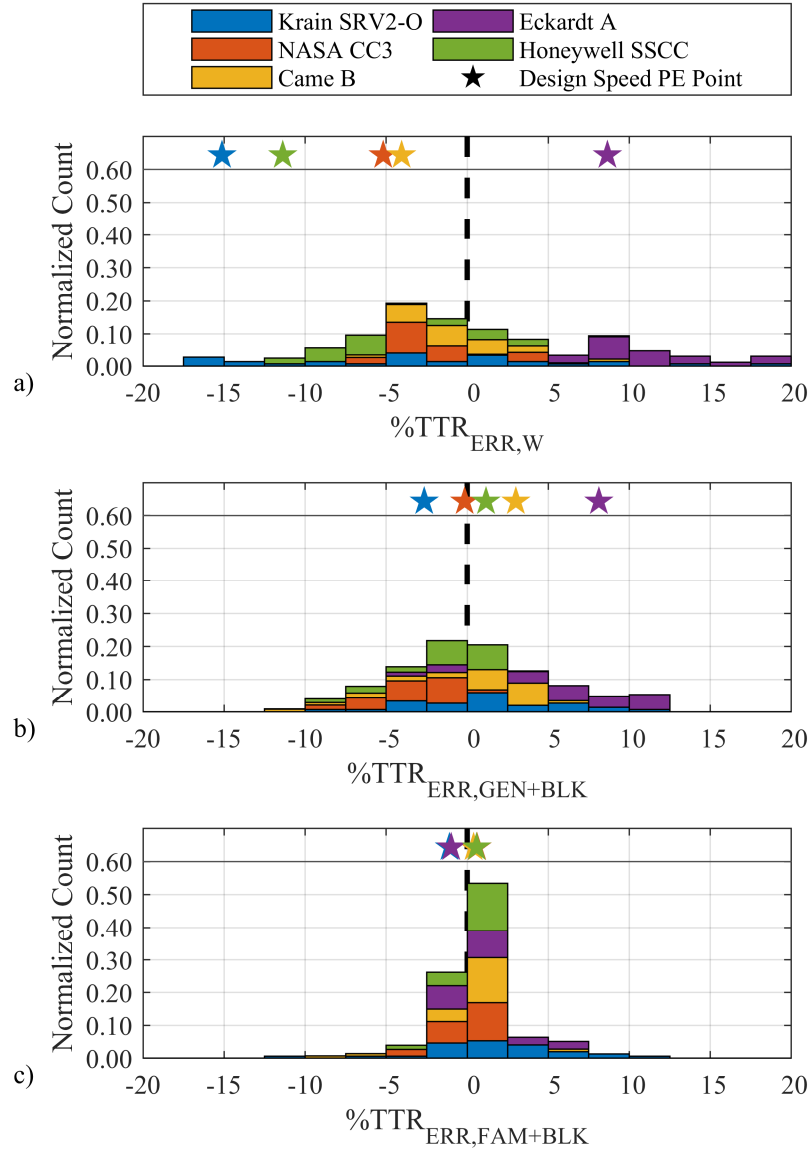
Figure 4.9: Relative error in predicted total temperature rise ratio with 10% impeller exit blockage for the a) Wiesner slip model, b) new slip model, general implementation, and c) new slip model, family implementation.

4.5 Alternate Correlations

Among the dimensionless parameters investigated, the product of the inlet flow coefficient and the square of the machine Mach number provided the best combination of ease of use, accuracy at high speeds, and minimal scatter at low speeds for the selected impellers. Consequently, most of the discussion in the present work is devoted to the correlation of total temperature rise ratio with this specific combination of parameters. However, multiple additional combinations of

116

dimensionless parameters correlate well with the ratio of the perfect flow guidance coefficient and the actual loading coefficient. Specifically, the product of the specific speed, N_S, and the square of the machine Mach number as well as the product of the ratio of the inlet flow coefficient to the exit flow coefficient and the square of the machine Mach number provided notably good results. The correlations for the general implementations of each of these parameters are given in equation (4.16),

$$TTR = 0.30\psi_{PFG}M_{U2}^2\left(M_{U2}^2 N_{S,PFG}\right)^{-0.12}, \tag{4.16}$$

and equation (4.17),

$$TTR = 0.31\psi_{PFG}M_{U2}^2\left(\frac{M_{U2}^2\phi_1}{\phi_{2,PFG}}\right)^{-0.09}. \tag{4.17}$$

The definition of specific speed used in equation (4.16) is

$$N_{S,PFG} = \frac{\phi_1^{0.5}}{\psi_{PFG}^{0.75}}. \tag{4.18}$$

The absolute error in slip factor, Figure 4.10, and the relative error distributions in total temperature rise ratio, Figure 4.11, are again presented to evaluate the accuracy of the method. The subfigures (b) and (c) correspond to equations (4.16) and (4.17), respectively. The error distribution for Wiesner's model is shown again for reference in subfigure (a) of both figures, and the SSCC impeller serves as a validation case. The general implementations for both the specific speed and ratio of flow coefficients are shown, but both can be utilized in the family implementation with recalculation of the coefficients for specific impeller designs.

The error distributions for the general implementations again show improvement in the prediction of slip factor and total temperature rise ratio relative to Wiesner's model and are comparable to the general correlation with inlet flow coefficient presented previously. When considering the design points in Figure 4.10b and Figure 4.10c, both alternate correlations show some
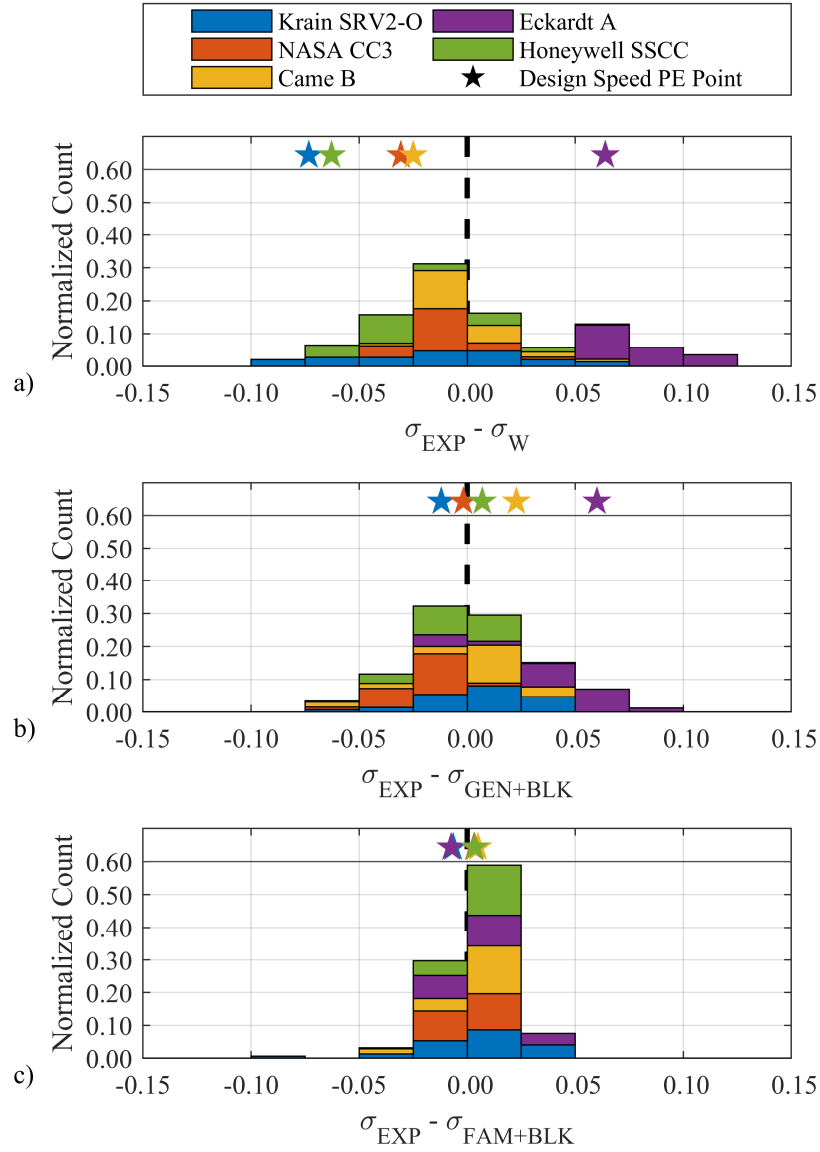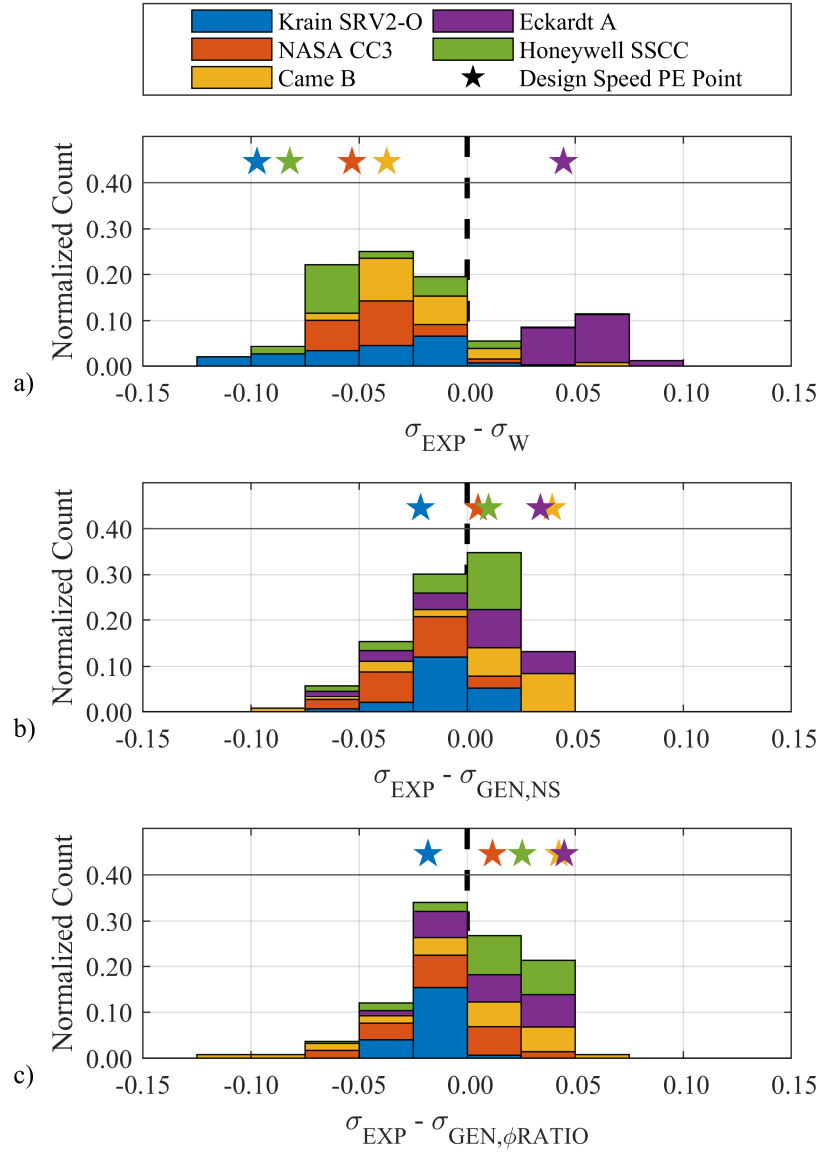
Figure 4.10: Difference between calculated and experimental values of slip factor and predicted values of slip factor for the a) Wiesner slip model, b) new slip model, general implementation for specific speed, and c) new slip model, general implementation for ratio of flow coefficients.

improvement in the prediction of slip factor relative to the correlation with inlet flow coefficient in Figure 4.1b. The overall error distribution of slip factor is also similar between the three different correlations. Parallel trends are observed in the prediction of total temperature rise ratio, Figure 4.11: the general implementation of the alternate correlations provides improved accuracy at the design point relative to the base correlation. However, there are more outliers with large negative relative errors for the alternate correlations.

118
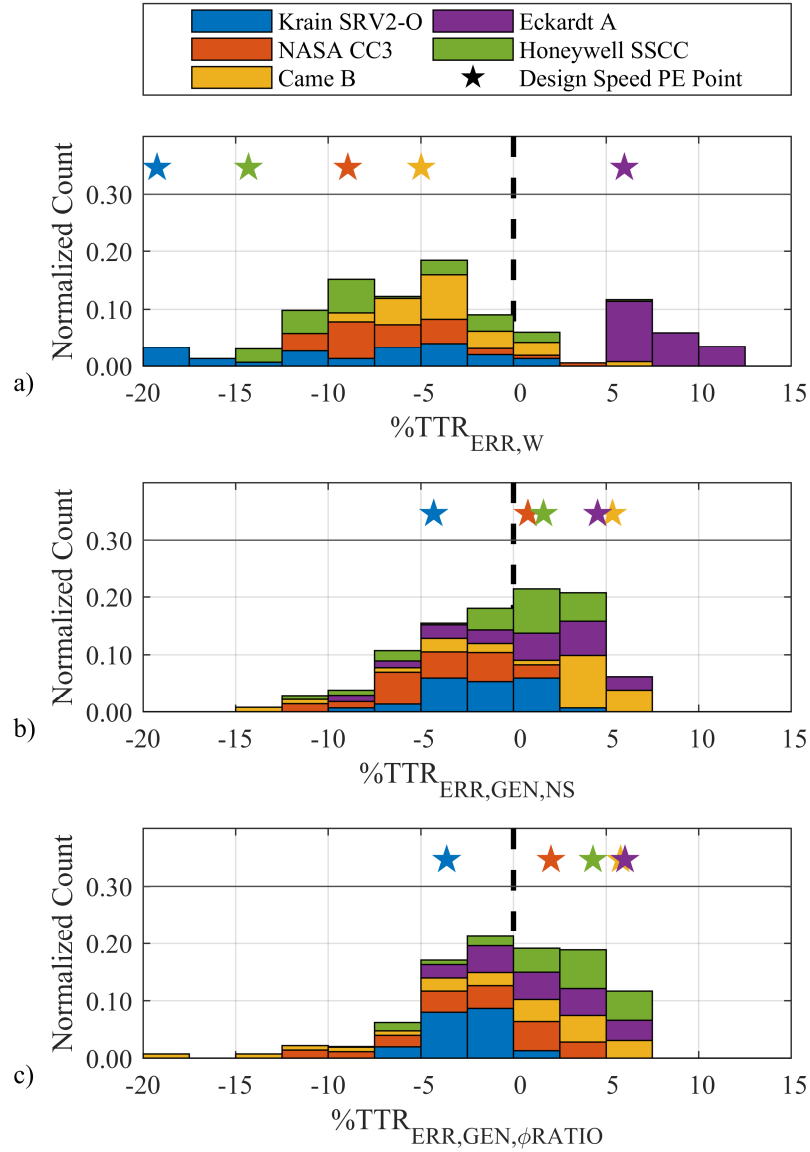
Figure 4.11: Relative error in predicted total temperature rise ratio for the a) Wiesner slip model, b) new slip model, general implementation for specific speed, and c) new slip model, general implementation for ratio of flow coefficients.

While the correlation with specific speed provides high accuracy at design point, the dependence on the specific speed introduces additional complexities into the model. For the model not to be recursive with the meanline equations, the perfect flow guidance specific speed must be used. Usage of an additional perfect flow guidance parameter introduces further reliance on modeling to the method. The same reasoning applies to the correlation with the ratio of flow coefficients: the impeller exit flow coefficient must be calculated from the perfect flow guidance condition. Thus,

the inlet flow coefficient correlation was chosen as the primary method for discussion in the present work. The alternate correlations are presented, however, as the additional resources may be of use during the design process.

5. CONCLUSIONS

A generalized meanline model for centrifugal compressors has been developed and validated. At the time of publication, the model has incorporated many loss models from the open literature, three commonly used slip models, and five compressors for use as case studies. The model has also been configured to enable one-dimensional analysis of experimental data for compressors based on overall performance measurements and validated with data from the open literature to verify the functionality of the model at design and off-design conditions. Validation of the model also serves as validation of the capability for OTAC itself to conduct off-design calculations for centrifugal compressors. The model was primarily developed for the investigation of slip models for centrifugal compressors, but it may serve as a design and analysis tool for a variety of applications.

Along with loss models which simulate entropy generation, slip models are a key component of the meanline design phase used to modify the ideal 1D equations such that they are representative of real compression processes. The current set of slip models in the open literature are all based, to some extent, on the relative eddy analysis originally presented by Stodola (Stodola, 1927) and mathematically derived for the case of logarithmic spiral blades by Busemann (Busemann, 1928). While Wiesner's, von Backström's, and Qiu's models may accurately reflect the theory presented by Busemann, it appears that the relative eddy theory may not completely represent the slip phenomenon in high-speed compressors. Because of this, there are errors between the slip factor predicted by each of the models and the actual slip factor experienced by the compressors, especially at large impeller tip Mach numbers. Furthermore, the slip models in the open literature are largely determined by the geometry of the impeller, and therefore, the predicted slip factor does not vary with operating conditions. The range of slip factors experienced by high-speed compressors may be quite large, so the slip factor predicted from geometry-governed models may provide a good estimate at some operating conditions and a less accurate estimate at others.

For the first time in the open literature, a robust trend of slip factor as a function of operating conditions is established, and the trend is consistent not only within the operating range of a single

121

impeller but also across dramatically different impeller designs. Slip factor generally decreases with increasing machine Mach number and decreasing loading coefficient, though the trend with loading coefficient may be reversed within a single impeller design. The trend of slip factor with design parameters has important implications for high-speed impeller designs: to minimize the work input not produced due to slip, high loading coefficients are necessary. Higher loading coefficients can be achieved by reducing the impeller backsweep angle, but the corresponding reduction in slip comes at the sacrifice of reduced stall margin and efficiency.

Slip factor is an important parameter for the accurate estimation of overall compressor performance. It is ultimately used to predict the work input of an impeller and the impeller exit velocity triangle, and this portion of the discussion is often neglected in the analysis of slip and slip models. Differences between the measured and predicted slip factor for each of the investigated open literature models leads to large errors in the predicted work input for the high-speed compressors. Error propagation analysis reveals that errors in slip factor are scaled by the square of the machine Mach number. Since the greatest differences between the measurements and experiments occurred at the highest impeller tip speeds, large errors in total temperature rise are observed at the design speed for all the high-speed stages. The error propagation analysis also reveals that an error of ±0.05 in slip factor, the traditionally accepted error band for prediction of the parameter, results in errors of predicted work input that may be as large or larger than the range of work input available along a speedline, especially for the high-speed stages. The reliability of slip models to predict slip for high-speed stages should be scrutinized.

Finally, a new method to model slip and work input for centrifugal compressor impellers has been introduced. Traditional slip models use the theory of the relative eddy to predict the flow physics at the impeller exit based on the impeller geometry. Rather than modeling flow physics, the new approach utilizes dimensionless parameters to predict the actual total temperature rise ratio from the perfect flow guidance condition. The new model is based on dimensionless parameters that are representative of both the operating conditions and impeller geometry. Thus, the model inherently supports prediction of slip factor at design and off-design conditions. The model is applicable to impellers throughout the centrifugal compressor design space by its dependence on the key design parameters of machine Mach number, loading coefficient, and flow coefficient. Additionally,

many slip models in the open literature require the specification of geometry beyond what is strictly necessary to establish the velocity triangles of the stage, such as blade number or blade thickness. The new model predicts slip factor and work input with parameters that are fundamental to establishing the duty of the compressor stage.

The new model provides greatly improved accuracy for predicting both slip factor and work input relative to other slip models available in the open literature, particularly near design speed for high-speed compressors. The dependence of the new model on the relationship between total temperature rise ratio, loading coefficient, and machine Mach number in equation (4.2) drives the high degree of accuracy observed throughout the present work. Since the model relies more heavily on governing equations than the actual modeling, numerous implementations of the model are possible. The general implementation of the model is recommended for broad application, equation (5.1):

$$TTR = A\psi_{PFG}M_{U2}^2(M_{U2}^2\phi_1)^B = 0.27\psi_{PFG}M_{U2}^2(M_{U2}^2\phi_1)^{-0.10}. \tag{5.1}$$

The two coefficients of the model, A and B, can be customized to fit specific impeller families, calculated with or without external losses, and for various design parameters. In the present work, the coefficients have been developed with respect to four well-documented centrifugal compressor cases from the open literature and validated with the Honeywell SSCC dataset. Ideally, additional datasets would be incorporated into the one-dimensional analysis procedures to develop the coefficients of the model. However, non-normalized design and off-design performance, as well as detailed specifications of stage geometry, are rarely published in the open literature. Hence, very few cases are available in the open literature with the extensive documentation necessary to construct a comprehensive one-dimensional model of the stage. It is, therefore, necessary for additional organizations to evaluate the model with respect to internal datasets to support further evaluation of the model's efficacy.

Whatever the application, the model has been shown to be robust to the inclusion or exclusion of external losses as well as blockage. Moreover, the reliance of the model on the governing relationships enables correlation of the actual work input delivered with a variety of dimensionless

design parameters. The reliance of the new model on governing relationships rather than modeling techniques, inherent incorporation of design conditions, and favorable uncertainty propagation together provide an improvement in predictive capability for slip factor and work input during centrifugal compressor preliminary design.

APPENDIX A: NONLINEAR REGRESSION ANALYSIS FOR DETERMINING SLIP MODEL COEFFICIENTS

The procedure to determine the coefficients *A* and *B* of the new model through nonlinear regression analysis has some flexibility due to the robustness of the method. In addition to the basic geometric parameters of the impeller, overall performance data of a centrifugal compressor stage is necessary to conduct the regression analysis. Ideally, the contribution of external losses to the overall stage total temperature rise ratio is known so that the total temperature rise ratio due to the impeller can be isolated through equation (5.2):

$$TTR_{IMPELLER} = TTR_{STAGE} - TTR_{EXTERNAL}. \qquad (5.2)$$

For cases where experimental data for the external losses are unavailable, as is common, the external losses can be modeled according to best practices. An alternative to the use of external loss models is to assign a portion of the overall loss to the external losses, as outlined in Chapter 3. As a final option, the new model is robust to the inclusion of external losses as discussed in Section 4.3, and the regression analysis can be conducted with overall total temperature data with a slight penalty to the accuracy of predictions. It must be noted that while the method is not overly sensitive to external losses, separation of the diffuser loss from impeller loss is necessary. Thus, the efficiency data provided to the method should either be the impeller efficiency, or the stage efficiency must be used in conjunction with a diffuser loss model to isolate the impeller loss from the diffuser loss.

Before proceeding with the regression analysis, the perfect flow guidance condition corresponding to each operating point in the dataset must be calculated to determine the perfect flow guidance loading coefficient. The perfect flow guidance specific speed and impeller exit flow coefficient can also be determined from the perfect flow guidance condition if one of the alternative implementations of the model given in Section 4.5 is used. The perfect flow guidance condition is calculated by using the mass flow rate and rotational speed associated with each operating point as inputs to a meanline analysis tool, with or without blockage per standard design practice. A slip factor of one is used to calculate the perfect flow guidance condition, and, in the present work, the

efficiency at the perfect flow guidance condition was assumed to be the identical to the actual operating conditions. Additionally, the proportion of external loss to overall loss was assumed to be identical between the actual operating condition and the perfect flow guidance condition. For example, 20% of the impeller loss was attributed to external loss at both the actual and perfect flow guidance conditions in the present work. If blockage is incorporated into the meanline model, it should be implemented in calculation of the perfect flow guidance condition in the same manner as calculating the actual operating condition. Matching the experimental efficiency was accomplished in the present work by iterating on the impeller loss until the total loss between the impeller and diffuser loss model resulted in an efficiency equal to the measured stage efficiency.

Nonlinear regression is then conducted on equation (4.8), equation (4.16), or equation (4.17) by providing a nonlinear regression analysis tool with the appropriate parameters from the chosen equation. The MATLAB function nlinfit was used in the present work (*MATLAB (version R2019a)*, 2019). The nonlinear regression analysis provides the user with the coefficients *A* and *B* to be implemented in the model of choice in a meanline analysis tool.

APPENDIX B. APPLICATION OF THE MODEL

The steps to introduce the new model into a meanline analysis tool are not rigid, and the procedures given herein are intended as guidelines rather than as imperatives. The two primary steps to incorporate the new model into an existing code are calculation of the slip factor from the predicted work input and integration of the model into the solver.

Equations (4.8), (4.16), and (4.17) all provide a predicted total temperature rise ratio rather than slip factor. However, most meanline analysis codes are set up to accept a predicted value for slip factor or deviation from a slip model, not total temperature rise ratio. To calculate the slip factor, the total temperature rise ratio of the impeller (excluding external losses as in Figure 4.1 and Figure 4.2) must be used. If the new model is implemented such that the external losses are included, as in Figure 4.5 and Figure 4.6, the total temperature rise ratio due to external losses must be deducted from the stage total temperature rise ratio. Once the total temperature rise ratio of the impeller is obtained, the loading coefficient associated with the impeller (excluding external losses) can be calculated via equation (5.3):

$$\psi_{IMPELLER} = \frac{TTR_{IMPELLER}}{(\gamma - 1)M_{U2}^2}. \tag{5.3}$$

The actual impeller exit tangential velocity is then calculated by relating the impeller loading coefficient to the flow velocities through equation (5.4),

$$V_{\theta 2} = \frac{\psi_{IMPELLER}U_2^2 - U_1 V_{\theta 1}}{U_2}. \tag{5.4}$$

From the impeller exit velocity triangle in Figure 1.6, the slip velocity can be calculated according to equation (5.5),

$$V_{slip} = U_2 - V_{\theta 2} - V_{m2} \tan \beta_{2b}. \tag{5.5}$$

Without the meanline equations, the impeller exit meridional velocity is unknown and the slip velocity cannot be determined. Thus, the model must be used in conjunction with meanline analysis tools to complete the system of equations. Once the slip velocity is determined from the model in conjunction with the meanline equations, and the slip factor can be calculated according to its definition:

$$\sigma = 1 - \frac{V_{slip}}{U_2} \tag{5.6}$$

An iterative procedure is recommended to incorporate the new slip model for predictive use in the development of a new impeller design (rather than matching experimental data). To initialize the iteration, a guess of the efficiency is made to calculate the perfect flow guidance condition at the operating point of interest. The appropriate perfect flow guidance parameters are then provided to equation (4.8), (4.16), or (4.17) from the perfect flow guidance operating point to calculate the slip factor. The slip factor and appropriate loss models are used to calculate the actual operating condition. The newly calculated efficiency is then used to recalculate the perfect flow guidance conditions and a new value of slip factor, and so on, until the efficiencies of the perfect flow guidance condition and actual operating condition converge.

REFERENCES

Aungier, R. H. (1995). Mean Streamline Aerodynamic Performance Analysis of Centrifugal Compressors. *Journal of Turbomachinery*, *117*(3), 360–366. https://doi.org/10.1115/1.2835669

Aungier, R. H., & Cassin, I. (2003). *Centrifugal Compressors: A Strategy for Aerodynamic Design and Analysis*. New York: ASME Press.

Bing, H., Tan, L., Cao, S., & Lu, L. (2012). Prediction method of impeller performance and analysis of loss mechanism for mixed-flow pump. *Science China Technological Sciences*, *55*(7), 1988–1998. https://doi.org/10.1007/s11431-012-4867-9

Busemann, A. (1928). Das Förderhöhenverhältnis radialer Kreiselpumpen mit logarithmisch-spiraligen Schaufeln. *ZAMM - Journal of Applied Mathematics and Mechanics / Zeitschrift Für Angewandte Mathematik Und Mechanik*, *8*(5), 372–384. https://doi.org/10.1002/zamm.19280080504

Came, P. M. (1978). The Development, Application and Experimental Evaluation of a Design Procedure for Centrifugal Compressors. *Proceedings of the Institution of Mechanical Engineers*, *192*(1), 49–67. https://doi.org/10.1243/PIME_PROC_1978_192_007_02

Came, P. M., & Herbert, M. V. (1980). Design and experimental performance of some high pressure ratio centrifugal compressors. *AGARD Centrifugal Compressors, Flow Phenomena and Performance*.

Casey, M., & Robinson, C. (2012). A Method to Estimate the Performance Map of a Centrifugal Compressor Stage. *Journal of Turbomachinery*, *135*(2), 021034-021034–10. https://doi.org/10.1115/1.4006590

Casey, M. V. (1985). The Effects of Reynolds Number on the Efficiency of Centrifugal Compressor Stages. *Journal of Engineering for Gas Turbines and Power*, *107*(2), 541–548. https://doi.org/10.1115/1.3239767

Casey, M. V., & Marty, F. (1986). Centrifugal compressors—performance at design and off-design. *Institute of Refrigeration at the Institute of Marine Engineers, London, UK*.

Conrad, O., Raif, K., & Wessels, M. (1979). The calculation of performance maps for centrifugal compressors with vane-island diffusers (pp. 135–147). Presented at the Performance Prediction of Centrifugal Pumps and Compressors.

Coppage, J. E., Dallenbach, F., Eichenberger, H. P., Hlvaka, G. E., Knoernschild, E. M., & Van Le, N. (1956). *Study of supersonic radial compressors for refrigeration and pressurization systems* (No. WADC report 55-257). Los Angeles, CA: Garrett Corporation Airesearch Manufacturing Division.

Cumpsty, N. A. (1989). *Compressor Aerodynamics*. Longman Scientific & Technical.

Daily, J. W., & Nece, R. E. (1960). Chamber Dimension Effects on Induced Flow and Frictional Resistance of Enclosed Rotating Disks. *Journal of Basic Engineering*, *82*(1), 217. https://doi.org/10.1115/1.3662532

Dean, R. C. (1971). On the unresolved fluid dynamics of the centrifugal compressor. *Advanced Centrifugal Compressors*, 1–55.

Dean, R. C., & Senoo, Y. (1960). Rotating wakes in vaneless diffusers. *Journal of Basic Engineering*, *82*(3), 563–570.

Del Greco, A. S., Biagi, F. R., Sassanelli, G., & Michelassi, V. (2009). A New Slip Factor Correlation for Centrifugal Impellers in a Wide Range of Flow Coefficients and Peripheral Mach Numbers (pp. 977–986). Presented at the ASME Turbo Expo 2007: Power for Land, Sea, and Air, Montreal, Canada: American Society of Mechanical Engineers. https://doi.org/10.1115/GT2007-27199

Denton, J. D. (1993). The 1993 IGTI Scholar Lecture: Loss Mechanisms in Turbomachines. *Journal of Turbomachinery*, *115*(4), 621–656. https://doi.org/10.1115/1.2929299

Dixon, S. L., & Hall, C. (2013). *Fluid Mechanics and Thermodynamics of Turbomachinery* (7th ed.). Butterworth-Heinemann.

Dubitsky, O., & Japikse, D. (2008). Vaneless Diffuser Advanced Model. *Journal of Turbomachinery*, *130*(1), 011020-011020–10. https://doi.org/10.1115/1.2372781

Eckardt, D. (1975). Instantaneous measurements in the jet-wake discharge flow of a centrifugal compressor impeller. *ASME J. Eng. Power*, *97*(3), 337–346.

Eckardt, D. (1976). Detailed flow investigations within a high-speed centrifugal compressor impeller. *Journal of Fluids Engineering*, *98*(3), 390–402.

Eckardt, D. (1978). *Investigation of the jet-wake flow of a highly loaded centrifugal compressor impeller* (No. NASA TM-75232). Retrieved from https://ntrs.nasa.gov/search.jsp?R=19780008108

Eckardt, D. (1980). Flow field analysis of radial and backswept centrifugal compressor impellers—part 1: Flow measurements using a laser velocimeter. In *Performance Prediction of Centrifugal Pumps and Compressors* (pp. 77–86). New Orleans, LA: American Society of Mechanical Engineers. Retrieved from http://adsabs.harvard.edu/abs/1979ppcp.proc...77E

Eisenlohr, G., Krain, H., Richter, F.-A., & Tiede, V. (2002). Investigations of the Flow Through a High Pressure Ratio Centrifugal Impeller. In *ASME Turbo Expo 2002: Power for Land, Sea, and Air* (Vol. 5, pp. 649–657). Amsterdam, The Netherlands: American Society of Mechanical Engineers. https://doi.org/10.1115/GT2002-30394

Forster, V. T. (1966). Performance loss of modern steam-turbine plant due to surface roughness. *Proceedings of the Institution of Mechanical Engineers*, *181*(1), 391–422.

Frigne, P., & Van den Braembussche, R. (1979). *One dimensional design of centrifugal compressors taking into account flow separation in the impeller* (No. VKI TN 129). Von Karman Institute for Fluid Dynamics.

Futral, S. M., & Wasserbauer, C. A. (1965). *Off-design performance prediction with experimental verification for a radial-inflow turbine* (No. NASA TN D-2621). National Aeronautics and Space Administration.

Galvas, M. R. (1973). *FORTRAN program for predicting off-design performance of centrifugal compressors*. Retrieved from https://ntrs.nasa.gov/search.jsp?R=19740001912

Gooding, W. J., Key, N. L., & Fabian, J. C. (2019). LDV Characterization of Unsteady Vaned Diffuser Flow in a Centrifugal Compressor. In *Proceedings of ASME Turbo Expo 2019* (p. 10). Phoenix, AZ, United States: American Society of Mechanical Engineers.

Grein, H. (1975). Some considerations on the surface roughness of wetted components of large hydraulic machines. *Escher Wyss News*, *1*, 34–40.

Greitzer, E. M., Tan, C. S., & Graf, M. B. (2007). *Internal Flow: Concepts and Applications* (Vol. 3). New York: Cambridge University Press.

Harley, P., Spence, S., Filsinger, D., Dietrich, M., & Early, J. (2013). Assessing 1D Loss Models for the Off-Design Performance Prediction of Automotive Turbocharger Compressors, V06CT40A005. https://doi.org/10.1115/GT2013-94262

Harley, P., Spence, S., Filsinger, D., Dietrich, M., & Early, J. (2014). Meanline Modeling of Inlet Recirculation in Automotive Turbocharger Centrifugal Compressors. *Journal of Turbomachinery*, *137*(1), 011007-011007–011009. https://doi.org/10.1115/1.4028247

Hassenpflug, W. C. (2010). The incompressible two-dimensional potential flow through blades of a rotating radial impeller. *Mathematical and Computer Modelling*, *52*(9), 1299–1389. https://doi.org/10.1016/j.mcm.2010.04.022

Herbert, M. V. (1980). *A method of performance prediction for centrifugal compressors* (No. ARC R & M 3843). HM Stationery Office.

Ibaraki, S., Furukawa, M., Iwakiri, K., & Takahashi, K. (2009). Vortical Flow Structure and Loss Generation Process in a Transonic Centrifugal Compressor Impeller (pp. 1089–1098). Presented at the ASME Turbo Expo 2007: Power for Land, Sea, and Air, American Society of Mechanical Engineers Digital Collection. https://doi.org/10.1115/GT2007-27791

Inoue, M., & Cumpsty, N. A. (1984). Experimental study of centrifugal impeller discharge flow in vaneless and vaned diffusers. *ASME, Transactions, Journal of Engineering for Gas Turbines and Power*, *106*, 455–467.

Jansen, W. (1967). A Method for Calculating the Flow in a Centrifugal Impeller when Entropy Gradients are Present. In *Internal Aerodynamics (Turbomachinery)* (pp. 133–146). Cambridge University: Institution of Mechanical Engineers.

Japikse, D. (1996). *Centrifugal Compressor Design and Performance* (2nd ed.). White River Junction, VT: Concepts ETI, Inc.

Japikse, D., & Baines, N. (1994). *Introduction to turbomachinery*.

Japikse, D., & Baines, N. C. (1998). *Diffuser Design Technology*. Norwich, VT: Concepts Eti.

Johnson, M. W., & Moore, J. (1980). The Development of Wake Flow in a Centrifugal Impeller. *Journal of Engineering for Power*, *102*(2), 382–389. https://doi.org/10.1115/1.3230265

Johnston, J. P., & Dean, R. C. (1966). Losses in Vaneless Diffusers of Centrifugal Compressors and Pumps: Analysis, Experiment, and Design. *Journal of Engineering for Power*, *88*(1), 49–60. https://doi.org/10.1115/1.3678477

Jones, S. M. (2014). *Development of an Object-Oriented Turbomachinery Analysis Code within the NPSS Framework* (No. NASA/TM-2014-216621). NASA. Retrieved from https://ntrs.nasa.gov/search.jsp?R=20140011370

Jones, S. M. (2015). Design of an Object-Oriented Turbomachinery Analysis Code: Initial Results. Presented at the 22nd International Symposium on Airbreathing Engines, Phoenix, AZ, United States. https://doi.org/ISABE-2015-20015

Kaneko, M., & Tsujita, H. (2015). Numerical investigation of influence of tip leakage flow on secondary flow in transonic centrifugal compressor at design condition. *Journal of Thermal Science*, *24*(2), 117–122. https://doi.org/10.1007/s11630-015-0763-5

Krain, H. (1981). A study on centrifugal impeller and diffuser flow. *Journal of Engineering for Power*, *103*(4), 688–697.

Krain, H. (1988). Swirling impeller flow. *ASME J. Turbomach*, *110*(1), 122–128.

Krain, H., Hoffmann, B., & Pak, H. (1995). Aerodynamics of a Centrifugal Compressor Impeller With Transonic Inlet Conditions (p. V001T01A011-V001T01A011). Presented at the ASME 1995 International Gas Turbine and Aeroengine Congress and Exposition, American Society of Mechanical Engineers. https://doi.org/10.1115/95-GT-079

Kulkarni, S., Beach, T. A., & Skoch, G. J. (2013). Computational study of the CC3 impeller and vaneless diffuser experiment. In *49th AIAA/ASME/SAE/ASEE Joint Propulsion Conference*. San Jose, CA: American Institute of Aeronautics and Astronautics. https://doi.org/10.2514/6.2013-3631

Lakshminarayana, B. (1995). *Fluid dynamics and heat transfer of turbomachinery*. John Wiley & Sons.

Lieblein, S., Schwenk, F. C., & Broderick, R. L. (1953). *Diffusion factor for estimating losses and limiting blade loadings in axial-flow-compressor blade elements.* NATIONAL ADVISORY COMMITTEE FOR AERONAUTICS CLEVELAND OH LEWIS FLIGHT ….

Lou, F. (2016). *A study on flow development in an APU-style inlet and its effect on centrifugal compressor performance* (PhD Dissertation). Purdue University, West Lafayette, IN.

Lou, F., Harrison, H. M., Fabian, J. C., Key, N. L., James, D. K., & Srivastava, R. (2016). Development of a Centrifugal Compressor Facility for Performance and Aeromechanics Research. In *ASME Turbo Expo 2016: Turbomachinery Technical Conference and Exposition* (p. V02DT42A005–V02DT42A005). American Society of Mechanical Engineers.

Mangani, L., Casartelli, E., & Mauri, S. (2012). Assessment of Various Turbulence Models in a High Pressure Ratio Centrifugal Compressor With an Object Oriented CFD Code. *Journal of Turbomachinery*, *134*(6), 061033. https://doi.org/10.1115/1.4006310

MATLAB (version R2019a). (2019). Natick, Massachusetts: The MathWorks Inc. Retrieved from https://www.mathworks.com/products/matlab.html

McKain, T. F. H. (1997). *Coordinates for a High Performance 4:1 Pressure Ratio Centrifugal Compressor* (No. NASA-CR-204134). Retrieved from https://ntrs.nasa.gov/search.jsp?R=19970024917

Medic, G., Sharma, O. P., Jongwook, J., Hardin, L. W., McCormick, D. C., Cousins, W. T., … Van Slooten, P. R. (2014). *High Efficiency Centrifugal Compressor for Rotorcraft Applications* (No. NASA/CR-2014-218114).

Moody, L. F. (1944). Friction factors for pipe flow. *ASME Transactions*, *66*(8), 671–684.

Musgrave, D. S. (1979). The prediction of design and off-design efficiency for centrifugal compressor impellers (pp. 185–189). Presented at the Performance Prediction of Centrifugal Pumps and Compressors. Retrieved from http://adsabs.harvard.edu/abs/1979ppcp.proc..185M

Numerical Propulsion System Simulation (NPSS). (2016). (Version v2.8). San Antonio, TX: Southwestern Research Institute (SwRI). Retrieved from https://www.swri.org/consortia/numerical-propulsion-system-simulation-npss

Oh, H. W., Yoon, E. S., & Chung, M. K. (1997). An optimum set of loss models for performance prediction of centrifugal compressors. *Proceedings of the Institution of Mechanical Engineers, Part A: Journal of Power and Energy*, *211*(4), 331–338. https://doi.org/10.1243/0957650971537231

Paeng, K. S., & Chung, M. K. (2001). A new slip factor for centrifugal impellers. *Proceedings of the Institution of Mechanical Engineers, Part A: Journal of Power and Energy*, *215*(5), 645–649. https://doi.org/10.1243/0957650011538776

Pampreen, R. C. (1981). A Blockage Model for Centrifugal Compressor Impellers. *Journal of Engineering for Power*, *103*(4), 698–707. https://doi.org/10.1115/1.3230792

Petermann, H., & Pfleiderer, C. (2013). *Strömungsmaschinen*. Springer-Verlag.

Qiu, X., Japikse, D., & Anderson, M. (2008). A Meanline Model for Impeller Flow Recirculation (pp. 1687–1694). Presented at the ASME Turbo Expo 2008: Power for Land, Sea, and Air, American Society of Mechanical Engineers. https://doi.org/10.1115/GT2008-51349

Qiu, X., Japikse, D., Zhao, J., & Anderson, M. R. (2011). Analysis and Validation of a Unified Slip Factor Model for Impellers at Design and Off-Design Conditions. *Journal of Turbomachinery*, *133*(4), 041018-041028–041029. https://doi.org/10.1115/1.4003022

Reddy, K. R. (1954). Relative Eddy and its Effects on the Performance of a Radial Bladed Centrifugal Impeller. *The Aeronautical Journal*, *58*(524), 547–555. https://doi.org/10.1017/S0368393100099193

Rodgers, C. (1979). Specific speed and efficiency of centrifugal impellers (pp. 191–200). Presented at the Performance Prediction of Centrifugal Pumps and Compressors. Retrieved from http://adsabs.harvard.edu/abs/1979ppcp.proc..191R

Sakai, T., Watanabe, I., Fujie, E., & Takayanagai, I. (1967). On the slip factor of centrifugal and mixed flow impellers. American Society of Mechanical Engineers.

Schlichting, H., & Gersten, K. (2016). *Boundary-Layer Theory*. Springer.

Schorr, P. G., Welliver, A. D., & Winslow, L. J. (1971). Design and Development of Small, High-pressure Ratio, Single-stage Centrifugal Compressor. In *Advanced Centrifugal Compressors* (pp. 147–216). New York: American Society of Mechanical Engineers.

Simon, H., & Bülskämper, A. (1984). On the Evaluation of Reynolds Number and Relative Surface Roughness Effects on Centrifugal Compressor Performance Based on Systematic Experimental Investigations. *Journal of Engineering for Gas Turbines and Power*, *106*(2), 489–498. https://doi.org/10.1115/1.3239592

Skoch, G. J., Prahst, P. S., Wernet, M. P., Wood, J. R., & Strazisar, A. J. (1997). Laser Anemometer Measurements of the Flow Field in a 4:1 Pressure Ratio Centrifugal Impeller (p. V001T03A049). American Society of Mechanical Engineers. https://doi.org/10.1115/97-GT-342

Stahler, A. F. (1965). The Slip Factor of a Radial Bladed Centrifugal Compressor. *Journal of Engineering for Power*, *87*(2), 181–188. https://doi.org/10.1115/1.3678159

Stanitz, J. D. (1949). *Two-dimensional compressible flow in turbomachines with conic flow surfaces* (No. NACA-TR-935). Cleveland, OH, United States: National Advisory Committee for Aeronautics, Lewis Flight Propulsion Lab. Retrieved from http://ntrs.nasa.gov/search.jsp?R=19930092000

Stanitz, J. D. (1952). *One-Dimensional Compressible Flow in Vaneless Diffusers of Radial- and Mixed-Flow Centrifugal Compressors, Including Effects of Friction, Heat Transfer and Area Change* (No. NACA-TN-2610). Cleveland, OH, United States: National Advisory Committee for Aeronautics, Lewis Flight Propulsion Lab. Retrieved from http://ntrs.nasa.gov/search.jsp?R=19930083365

Stanitz, J. D., & Ellis, G. O. (1950). *Two-dimensional compressible flow in centrifugal compressors with straight blades* (No. NACA-TR-954). Cleveland, OH, United States: National Advisory Committee for Aeronautics Lewis Flight Propulsion Lab. Retrieved from http://ntrs.nasa.gov/search.jsp?R=19930092019

Stodola, A. (1927). *Steam and gas turbines: with a supplement on the prospects of the thermal prime mover* (Vol. 2). McGraw-Hill.

Stuart, C., Spence, S., Filsinger, D., Starke, A., & Kim, S. I. (2017). Characterizing the Influence of Impeller Exit Recirculation on Centrifugal Compressor Work Input. *Journal of Turbomachinery*, *140*(1), 011005-011005–011013. https://doi.org/10.1115/1.4038120

Stuart, C., Spence, S., Filsinger, D., Starke, A., & Kim, S. I. (2019). A Three-Zone Modeling Approach for Centrifugal Compressor Slip Factor Prediction. *Journal of Turbomachinery*, *141*(3), 031008. https://doi.org/10.1115/1.4042248

Stuart, C., Spence, S., Filsinger, D., Starke, A., Kim, S. I., & Harley, P. (2015). An Evaluation of Vaneless Diffuser Modelling Methods as a Means of Improving the Off-Design Performance Prediction of Centrifugal Compressors (p. V02CT42A021-V02CT42A021). Presented at the ASME Turbo Expo 2015: Turbine Technical Conference and Exposition, American Society of Mechanical Engineers. https://doi.org/10.1115/GT2015-42657

Suhrmann, J. F., Peitsch, D., Gugau, M., Heuer, T., & Tomm, U. (2010). Validation and Development of Loss Models for Small Size Radial Turbines (pp. 1937–1949). Presented at the ASME Turbo Expo 2010: Power for Land, Sea, and Air, American Society of Mechanical Engineers Digital Collection. https://doi.org/10.1115/GT2010-22666

Takagi, T., Kobayashi, J., Miyashiro, H., & Morimoto, H. (1980). Performance prediction of single-suction centrifugal pumps of different specific speeds. In *Proceedings of the Conference on Performance Prediction of Centrifugal Pump and Compressors* (pp. 227–234).

Thanapandi, P., & Prasad, R. (1990). Performance Prediction and Loss Analysis of Low Specific Speed Submersible Pumps. *Proceedings of the Institution of Mechanical Engineers, Part A: Journal of Power and Energy*, *204*(4), 243–252. https://doi.org/10.1243/PIME_PROC_1990_204_033_02

Thanapandi, P., & Prasad, R. (1994). A Quasi-Steady Performance Prediction Model for Dynamic Characteristics of a Volute Pump. *Proceedings of the Institution of Mechanical Engineers, Part A: Journal of Power and Energy*, *208*(1), 47–58. https://doi.org/10.1243/PIME_PROC_1994_208_008_02

Todd, C. A., & Futral, S. M. (1969). *A FORTRAN IV program to estimate the off-design performance of radial-inflow turbines* (No. NASA TN D-5059). National Aeronautics and Space Administration.

von Backström, T. W. (2005). A Unified Correlation for Slip Factor in Centrifugal Impellers. *Journal of Turbomachinery*, *128*(1), 1–10. https://doi.org/10.1115/1.2101853

Whitfield, A. (1974). Slip Factor of a Centrifugal Compressor and Its Variation with Flow Rate. *Proceedings of the Institution of Mechanical Engineers*, *188*(1), 415–421. https://doi.org/10.1243/PIME_PROC_1974_188_047_02

Whitfield, A. (1990). Preliminary Design and Performance Prediction Techniques for Centrifugal Compressors. *Proceedings of the Institution of Mechanical Engineers, Part A: Journal of Power and Energy*, *204*(2), 131–144. https://doi.org/10.1243/PIME_PROC_1990_204_018_02

Whitfield, A., & Baines, N. C. (1990). *Design of radial turbomachines*. Harlow, Essex, England : New York, NY: Longman Scientific & Technical ; Wiley.

Wiesner, F. J. (1967). A Review of Slip Factors for Centrifugal Impellers. *Journal of Engineering for Power*, *89*(4), 558–566. https://doi.org/10.1115/1.3616734

Wood, J. R., Adam, P. W., & Buggele, A. E. (1983). NASA Low-Speed Centrifugal Compressor for Fundamental Research (p. 1351). Presented at the 19th Joint Propulsion Conference, Seattle, Washington. Retrieved from https://ntrs.nasa.gov/search.jsp?R=19830017391

VITA

Herbert Monroe Harrison III, better known as Trey, was born in Chapin, South Carolina to parents Herb Harrison and Nancy Buntyn on April 8, 1991. He grew up in Chapin with one brother, Turner Harrison. Trey graduated from Chapin High School in 2009 and began pursuing a Bachelor's Degree in Mechanical Engineering at Clemson University the same year. During his undergraduate studies, he had multiple internship with AFL in Duncan, South Carolina. He graduated with Departmental Honors from Clemson in May 2014. He began his graduate studies at Purdue University in 2014 in the School of Mechanical Engineering with advisor Nicole L. Key. During his graduate work Trey studied the effects of complex inlet distortions on centrifugal compressor performance and operability and developed analysis tools to investigate centrifugal compressors from a one-dimensional perspective. He received a Master of Science from Purdue in 2016. Trey was awarded the Laura Winkelman Davidson Fellowship as well as the NASA Graduate Aeronautics Scholarship over the course of his graduate work at Purdue. As part of the Graduate Aeronautics Scholarship, he worked at the NASA Glenn Research Center to support development of a computational model of the High Efficiency Centrifugal Compressor. Trey will receive his Ph.D. from the School of Mechanical Engineering in May 2020 and has accepted a position as an Aerospace Engineer at the NASA Glenn Research Center.